Czech Technical University in Prague

Faculty of Nuclear Sciences and Physical Engineering

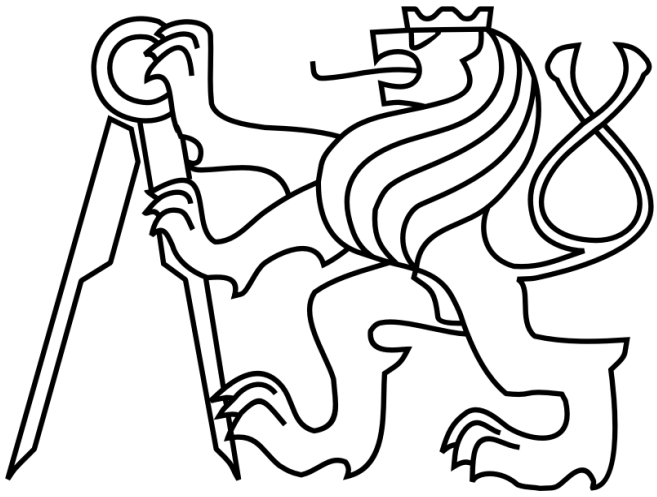

DOCTORAL THESIS

Study of the real structure of laser-cladded steel

Prague 2022 Ing. Karel Trojan

Acknowledgement

I would like to express my gratitude to my supervisor Prof. Nikolaj Ganev for his support and guidance. I am also grateful to my colleagues Dr. Kamil Kolařík and Dr. Jiří Čapek at the X-ray diffraction laboratory, FNSPE, CTU in Prague. Further, I would like to offer my special thanks to Dr. Václav Ocelík for valuable suggestions and an initiation into electron microscopy.

I would like to thank my family, especially my parents, for their support during my Ph.D. studies.

I appreciate the opportunity to use the equipment and facilities for the experiments. Measurements using electron microscopy were supported by The University of Groningen, The Netherlands. Neutron diffraction measurements were carried out at the CANAM facility of NPI ASCR Řež supported through Ministry of Education, Youth, and Sports Project No. LM2015056 as well as at Reactors LVR-15 and LR-0 supported by Project LM2018120 of the Ministry of Education, Youth, and Sports of the Czech Republic. Instrumented indentation measurements were performed by Dr. Jaroslav Čech at the Department of Materials, FNSPE, CTU in Prague. The microstructure was described with the help of Ing. Vladimír Mára from the Department of Material Engineering of the CTU Faculty of Mechanical Engineering in Prague.

This work was supported by European Regional Development Fund Project No. CZ.02.1.01/0.0/0.0/16_019/0000778, projects No. TH02010664 and TH04010475 of the Technology Agency of the Czech Republic, and Grant No. SGS22/183/OHK4/3T/14 from the Grant Agency of the Czech Technical University in Prague.

Bibliografický záznam

Autor:	Ing. Karel Trojan České vysoké učení technické v Praze Fakulta jaderná a fyzikálně inženýrská Katedra inženýrství pevných látek
Název práce:	Studium reálné struktury laserových návarů ocelí
Studijní program:	Aplikace přírodních věd
Studijní obor:	Fyzikální inženýrství
Školitel:	prof. Ing. Nikolaj Ganev, CSc. České vysoké učení technické v Praze Fakulta jaderná a fyzikálně inženýrská Katedra inženýrství pevných látek
Školitel specialista:	Ing. Kamil Kolařík, Ph.D. České vysoké učení technické v Praze Fakulta jaderná a fyzikálně inženýrská Katedra inženýrství pevných látek
Akademický rok:	2022
Počet stran:	143
Klíčová slova:	laserové navařování; nástrojová ocel AISI H13; mikrostruktura; reálná struktura; rentgenová difrakce; neutronová difrakce; elektronová difrakce; zbytková napětí; mechanické vlastnosti

Bibliographic Entry

Author:	Ing. Karel Trojan Czech Technical University in Prague Faculty of Nuclear Sciences and Physical Engineering Department of Solid State Engineering
Title of thesis:	Study of the real structure of laser-cladded steel
Degree program:	Applications of Natural Sciences
Field of study:	Physical Engineering
Supervisor:	prof. Ing. Nikolaj Ganev, CSc. Czech Technical University in Prague Faculty of Nuclear Sciences and Physical Engineering Department of Solid State Engineering
Supervisor specialist:	Ing. Kamil Kolařík, Ph.D. Czech Technical University in Prague Faculty of Nuclear Sciences and Physical Engineering Department of Solid State Engineering
Academic year:	2022
Number of pages:	143
Keywords:	laser cladding; AISI H13 tool steel; microstructure; real structure; X-ray diffraction; neutron diffraction; electron diffraction; residual stresses; mechanical properties

Abstract:

Hot-work tool steels are common die materials used in metal and casting industries. Dies, moulds, and more suffer damage due to wear and thermo-dynamic stresses during their lifetime. Therefore, various methods have been developed for their refurbishment or repair, which is cheaper than manufacturing new ones. A great benefit of laser cladding (one of the methods of additive manufacturing) is the high 3D production rate that is minimally influenced by thermal stresses due to a low heat input on surrounding material. Real structure is one of the most important factors that influences the behaviour of the product, especially fatigue life. Therefore, the aim of this thesis is to describe the effects of the laser cladding process on the real structure, microstructure, and mechanical properties of H13 tool steel using various diffraction methods. The results obtained were compared with the local hardness and wear measurements. Laser cladding of H13 tool steel showed great application potential. At the end of the work, further research is proposed that will necessarily focus on the design of the printing layout when cladding a larger volume.

Abstrakt:

Nástrojové oceli pro práci za tepla jsou běžné materiály používané ve strojírenském a slévárenském průmyslu. Formy, zápustky a jiné trpí silným opotřebováním a termodynamickým namáháním během své životnosti. Proto byly vyvinuty různé nové způsoby jejich úprav nebo oprav, které jsou levnější než výroba nových součástí. Laserové navařování (jedna z metod aditivní výroby) má velkou přednost v tom, že zajišťuje s minimálním tepelným namáháním v důsledku nízkého vneseného tepla do okolního materiálu vysokou trojrozměrnou produktivitu. Reálná struktura je jedním z nejdůležitějších faktorů, které ovlivňují chování výrobku, zejména jeho únavovou životnost. Cílem této práce je popsat pomocí různých difrakčních metod vliv laserového navařování na reálnou strukturu, mikrostrukturu a mechanické vlastnosti nástrojové oceli H13. Získané výsledky byly porovnány s tvrdostí návaru a jeho otěruvzdorností. Výzkum potvrdil, že laserové navařování nástrojové oceli H13 má značný aplikační potenciál. V závěru práce je navržen další výzkum s cílem najít návrh postupu pro depozici větších objemů.

Table of contents

List of abbreviations

AE	Auger Electrons
AF	Acicular Ferrite
AISI	American Iron and Steel Institute
BB	Bragg-Brentano
bcc	body-centred cubic
bct	body-centred tetragonal
BSE	Back-Scattered Electrons
DMLM	Direct Metal Laser Melting
EBSD	Electron Backscatter Diffraction
EDM	Electric Discharge Machining
EDS	Energy-Dispersive X-ray Spectroscopy
fcc	face-centred cubic
FWHM	Full Width at Half of the Maximum
GAM	Grain Average Misorientation
HAZ	Heat Affected Zone
IPF	Inverse Pole Figure
IQ	Image Quality
KAM	Kernel Average Misorientation
L	Longitudinal (direction)
LABE	Low-Angle Backscattered Electron
LMD	Laser Metal Deposition
N	Normal (direction)
ND	Neutron Diffraction
ODF	Orientation Distribution Function
OIM	Orientation Imaging Microscopy
PDF	Powder Diffraction File
PF	Pole Figure
RA	Retained Austenite
RS	Residual Stress / Residual Stresses
SE	Secondary Electrons
SEI	Secondary Electron Image

SEM	Scanning Electron Microscope
SLM	Selective Laser Melting
T	Transversal (direction)
TEM	Transmission Electron Microscope
TTA	Time-Temperature-Austenitization
TTT	Time-Temperature-Transformation
XRD	X-ray Diffraction

1 Introduction

This doctoral thesis aims to comprehensively evaluate the effect of laser cladding on the real structure of steels. Laser cladding is one of the methods of additive production, where the energy of a laser beam is used to melt the material. Additive production refers to the process by which a product is created by gradually applying thin layers on top of each other [1]. Real structure, which includes residual stresses, texture, size of crystallites, and others, significantly affects the properties of polycrystalline materials [2]. Therefore, the real structure significantly affects the service life of components that are made of these materials [3].

The purpose of this work was not to find the right processing parameters that could be used in production itself, but rather to describe the effect of laser cladding on the microstructure, real structure, residual stresses, and other mechanical properties that significantly affect the utility properties of the newly created volume, which by its nature forms the functional surface of the machine part.

Hot-work AISI H13 tool steel, which is widely used in industry, was chosen as a representative sample. This tool steel is one of the most common die materials used in metal and casting industries. Dies, mould parts, gears, plastic processing screws, ejectors, scissors, knives for hot cutting, etc. suffer damage due to wear and thermodynamic stresses during their lifetime [4]. Therefore, various methods have been developed for their repair, which is cheaper than manufacturing new ones. A great benefit of laser additive manufacturing (cladding) in this field is high productivity with minimal influence by thermal stresses due to a low heat input on surrounding material. As a result, it can significantly reduce repair costs, as there is no need for heat treatment, which is time consuming and, above all, costly for large components [5]. Another approach is to use dies with conformal cooling where the cooling channels can be closer to the surface and thus better control the cooling rate. Unlike additive manufacturing, complex cooling channels cannot be created by conventional methods such as drilling [6].

In order for a machine part to serve reliably during further operation, the mechanical properties of the new volume must at least attain the same values as the rest of the part. Since the dies, moulds, and more are cyclically loaded, it is necessary to describe the residual stresses that significantly affect the fatigue life. It is desirable to avoid tensile residual stresses, which reduce the yield strength and accelerate the rate of

crack growth [7]. An equally important factor is the hardness of the material and its wear resistance, where it is necessary to avoid lower value areas which would lead to faster wear and thus to component failure [8]. Since laser cladding does not achieve the same precision as other types of additive manufacturing, it is necessary to machine the surface into the desired shape [9]. Therefore, the effect of finishing processes on the newly created surface needs to be characterized.

The theoretical part of this thesis describes laser cladding and further explains the real structure of crystalline materials in detail. The experimental methods that have been used to describe the real structure and other properties of the laser-cladded samples are discussed in a separate chapter. All theoretical chapters are required to understand the need for a given research topic and the analytical methods used. Based on a study of the available literature and industry requirements, experimental samples were prepared and subjected to thorough examination by various methods. X-ray, neutron, and electron diffraction methods were used for the main part of the research. Based on the knowledge acquired, recommendations are proposed in the conclusion of this thesis regarding the direction of further research.

2 Theory

2.1 Laser cladding of steels

Today lasers are widely used in everyday life. Laser is an acronym that stands for “Light Amplification by Stimulated Emission of Radiation”, where stimulated emission of radiation means the stimulation by an incident photon of an excited atom which transitions to the ground state while simultaneously emitting another photon with the same wavelength, polarization, and direction as the stimulating photon [10] [11].

This type of radiation has been widely used for its exceptional properties and new applications continue to arise. No one is surprised to use a laser printer at home or watch a movie on DVD. Lasers are being progressively used in medicine, for example, for eye surgery, skin care or cosmetics. On the other hand, people are less aware of the wide use of lasers in industry. The laser processing of engineering materials includes several processes such as welding, cladding, marking, engraving, drilling, cutting, hardening, and more [11]. This doctoral thesis presents research on the laser processing of steels, especially laser cladding.

Optical systems can be used to concentrate laser radiation into a very small point, theoretically up to the magnitude of the radiation wavelength, but in practice, a beam diameter of 0.1 to 0.001 mm can be achieved. By focusing laser radiation, it is possible to provide for an energy flow of more than 10^6 Wmm^{-2}, and, consequently, such a high energy flow is capable of melting virtually any material [11].

Thanks to their wide range of energy flux and beam diameters, laser beams are widely used in various technological processes. Individual methods for the laser treatment of metals and alloys are shown in Figure 1, where the x-axis shows the time that the laser irradiates the surface of the material being treated, and the y-axis shows the power density of the laser. Both parameters are more or less independent of each other [11].

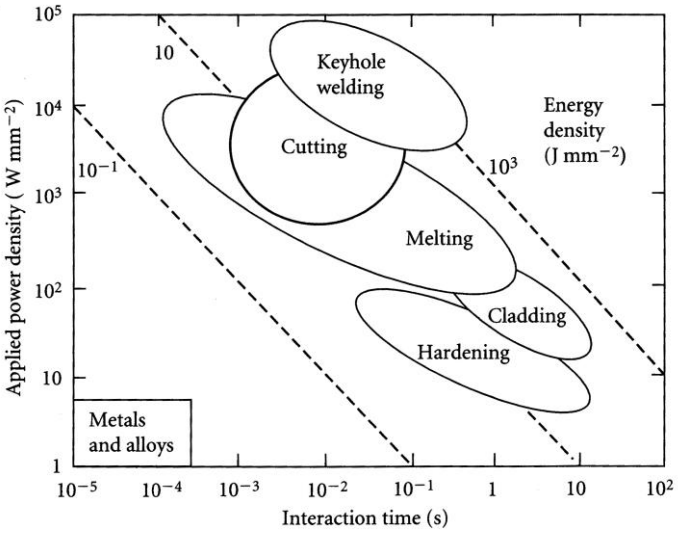

Figure 1: Laser treatment of metals and alloys [11].

2.1.1 Lasers

From a structural point of view, lasers are divided into three main groups – gas lasers, solid state lasers, and semiconductor (diode) lasers. Fibre lasers, which mostly use semiconductor lasers for pumping, stand outside this division [12].

The CO_2 laser is the best-known gas laser which uses a mixture of helium, nitrogen, and carbon dioxide as an active medium. It generates radiation with wavelengths of 9.4 and 10.6 μm. The active medium contains separate energy levels of electrons that allow stimulated emission. The resonator, which is mostly delimited by two mirrors, contains an active medium and its design suppresses radiation of inappropriate frequencies or radiation with inappropriate propagation direction [12]. Electric discharge is most often used for pumping, i.e. exciting the active medium to higher energy levels. First, the nitrogen molecule is excited, which then collides with the carbon dioxide molecule, imparting its energy. Helium helps carbon dioxide to transit to the ground state and during this, a photon is emitted. [13]. The CO_2 gas laser is used in welding, cutting, and engraving. Radiation of this laser is well absorbed by water, so it is also used in medicine. A disadvantage of this process is that the laser beam cannot be guided through optical fibres, and therefore reflection from mirrors is used [14]. Other gas lasers include, for example, helium-neon, argon and nitrogen.

Ruby lasers, Nd:YAG lasers, and neodymium glass lasers are the most important solid state lasers. Ruby crystal with chromium atoms is used as an active medium in

a ruby laser. The ruby laser usually operates in a pulse mode. However, the Nd:YAG laser is the most widely used solid-state laser. Its active medium consists of yttrium aluminium garnet doped with neodymium ions, which serve as excitation atoms. This type of laser is most often excited by a xenon lamp or a laser diode. Depending on the excitation, the laser can generate radiation in both pulse and continuous mode [14]. It is used for welding, cutting, drilling or marking. It is also widely employed in ophthalmology.

With the development of semiconductor technology, semiconductor lasers have become the most common type of lasers. Heterostructures or junctions with potential wells are typically used as the active medium of semiconductor lasers. These lasers use an inverse state p–n junction where electrons and holes are injected [15]. Diodes with power ranging from a few to dozens of watts are referred as high-power diodes [14].

In fibre lasers, laser radiation is generated inside the optical fibre, which is doped with rare earth ions. Ytterbium is the most commonly used, erbium or thulium can also be employed. The fibres may be single-sheathed or double-sheathed. Multimode laser diodes with a high divergence beam and a large emitting surface are most often used for pumping double-shell fibres. Single-shell fibres are used for single-mode diodes [16]. Double-sheathed fibres have the advantage that the low-quality multimode diode radiation can be coupled from the outer sheath to the inner single-mode fibre, which is doped with rare earth ions. The principle of pumping is similar to the previous types of lasers, as it occurs through excited states of rare earth ions, when after excitation the atom gets to the ground state by the desired stimulated emission or a competing process of spontaneous emission with simultaneous photon radiation. Stimulated emission increases the intensity of laser radiation, while spontaneous emission is a source of noise. Compared to conventional solid-state lasers, fibre lasers are highly stable, operationally reliable, compact and small. Thanks to the single-mode inner fibre, they also ensure excellent output beam quality. The overall efficiency of commercial fibre lasers is up to 25–35% [17].

2.1.2 Laser cladding

Cladding is a process in which a new material is applied to the surface of a base material. Cladding is performed in order to increase the functional capabilities of a substrate surface, where a more noble material is typically used to increase resistance to mechanical wear and corrosion, or the same material is cladded to the surface to renovate already

worn surfaces. Cladding also has an economic justification when it is not necessary to produce the entire product from a noble material and only the functional surface is sufficient. Other economic benefits stem from repairs, when it is sometimes much cheaper to repair a worn part than to produce an entirely new part [11]. Another approach is to use dies with conformal cooling where the cooling channels can be closer to the surface and thus better control the cooling rate. Complex cooling channels cannot be created by conventional methods such as drilling [6].

Cladding methods are similar to welding technology, where it is necessary to supply energy to melt both the substrate and the welded material. It is possible to use an electric arc or a laser beam. The cladded material, most often in the form of wire, tape or powder, is melted and then joins the melt pool formed on the base material. The deposit then crystallizes and forms a clad layer on the part, which is metallurgically bonded to the substrate. The metallurgical bonding of the cladded material with the substrate is the main advantage, due to its strength. Another advantage is the ability to clad almost any thickness with minimal mixing [11].

Laser cladding is a method of additive production, where the energy of a laser beam is used to melt the material. Additive production refers to the process by which a product is created by gradually applying thin layers on top of each other. The term Rapid Prototyping is used for the production of prototypes and printing from plastics is generally referred to as 3D printing.

Additive metal production mainly uses powders, which are most often melted through laser radiation to form a new volume in layers. Two approaches are used. The first uses a powder bed, where the material is applied to the work surface and only the given shape for a given layer is subsequently remelted by laser radiation. This method known as Selective Laser Melting (SLM) or Direct Metal Laser Melting (DMLM) achieves high accuracy, but the process is very slow [1].

The second approach uses a powder feeder, which is directed into the laser beam. The molten metal then solidifies and forms a new volume, see Figure 2. This method referred to as laser cladding or Laser Metal Deposition (LMD) [1] is less accurate, but the cladding speed is several times faster. Figure 2 shows a laser head with a nozzle and a powder feeder. Two different ways of powder feeding are common: from a side of the laser beam or coaxially (see Figure 2). When the powder is injected from the side, two directions can be distinguished: over hill and against hill, depending on the movement of the laser head or substrate. Against hill designates when the powder is injected from the

side towards which the laser track is moving. This direction shows higher powder efficiency. On the contrary, against hill is used for surface modification, e.g. injecting ceramic particles into the surface layer. The coaxial nozzle is advantageous in that the cladding efficiency does not depend on the movement of the laser head or substrate [18].

During cladding, see Figure 2, the powder and part of the base material is melted by the energy of the laser and a melt pool is formed, which then solidifies and forms a new clad layer on the base material. A bonding zone is created, where the mixing of the cladded metal with the base material is observable. Further, the heat-affected zone is important, especially in terms of the mechanical properties of the cladded metal. The powder is fed with an inert gas, while at the same time the molten material is protected by the inert shielding gas.

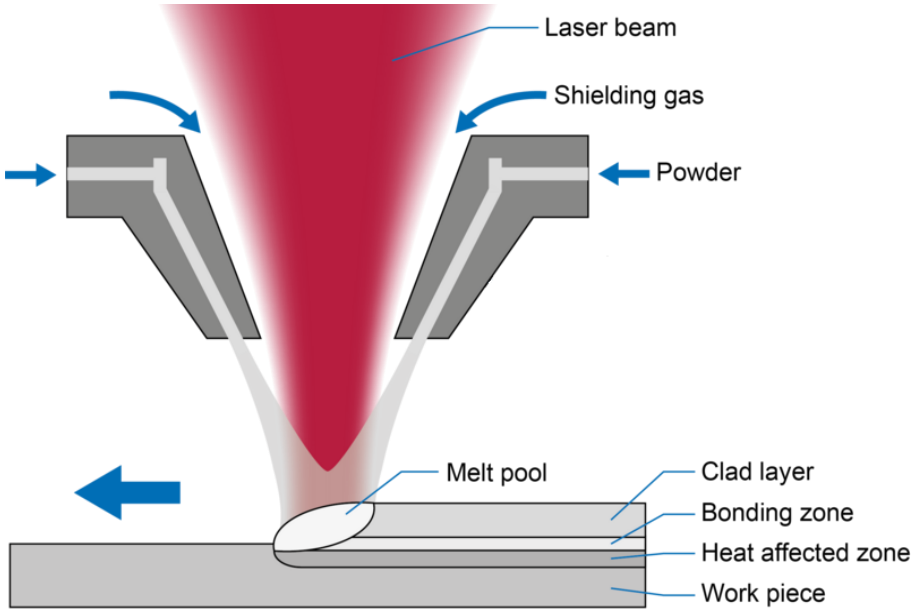

Figure 2: Laser cladding [19].

2.2 Steels

A phenomenon called polymorphism can be observed in most metals, including iron. Polymorphism is the ability of an element to crystallize into different crystal systems. Individual types are called modifications or phases and are usually labelled in Greek letters (i.e. α, β, γ…). When cooled down below a given freezing point, the original primary structure, which is formed from the melt and is replaced by a secondary structure, changes through recrystallization. This creates a different modification. For metals, the whole process described is reversible [20]. The Greek letter α usually indicates the stable phase with the lowest temperature, the letter β indicates the stable phase with the second lowest temperature, etc.

For iron, different modifications can be distinguished. The α-Fe phase represents iron with a body-centred cubic (bcc) lattice up to a Curie temperature of 768°C. Above this temperature, iron no longer exhibits ferromagnetic properties, but retains a body-centred cubic lattice. This modification is referred to as β-Fe. At approximately 910°C, the body-centred cubic lattice changes into a face-centred cubic (fcc) lattice called γ-Fe. At about 1400°C, iron is again transformed back into the original body-centred cubic lattice, this iron modification being called δ-Fe [21].

For steels, a solid solution is distinguished as a separate phase. A solid solution is a phase consisting of at least two components. Its crystal structure coincides with the lattice of one of the components (solvent or solute) and the lattice parameters are a continuous function of the chemical composition. A compound, which also has at least a two-component phase, differs from a solid solution in that it either has a lattice other than the components, or its parameters are not a continuous function of the chemical composition [22].

In a substitute solid solution some atoms in the lattice are replaced by atoms of approximately the same dimensions and similar chemical properties. Another possibility is an interstitial solid solution where the atoms of the dissolved component reach the inter-nodal positions of the crystal lattice of the solvent. The last type is a subtractive solid solution where the lattice has a certain number of unoccupied nodal points and the ratio is not proportional to the stoichiometric ratio of the ideal crystal lattice. As a result, one of the components is in an apparent excess [22].

The two-component binary equilibrium diagrams in two-component systems determine the dependence between temperature and chemical composition under the

given isobaric conditions. These diagrams provide information only about the composition and the quantity of the given phases, but not the structural distribution of the phases. In addition, they show only ideal equilibrium states in which perfect diffusion is assumed, i.e. cooling or heating of the system at a very slow pace, approximately by 3°C/h. However, this is not in accordance with the general practice, since heating and cooling are carried out at higher speeds and thereby the system becomes unbalanced [23].

The iron-iron carbide phase binary diagram in Figure 3 describes the alloy microstructure equilibrium versus composition and temperature. By using this diagram, it is possible to determine the temperature range and the composition under which a given phase is stable [11].

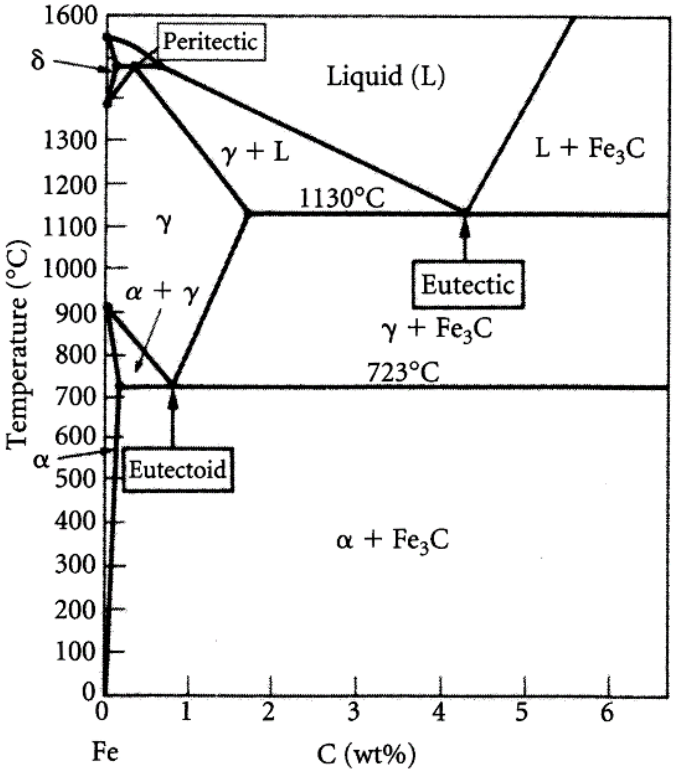

Figure 3: Iron-iron carbide phase binary diagram [11].

Ferrite is an interstitial solid solution of carbon in α-Fe with a body-centred cubic crystal lattice. Austenite is an interstitial solid solution of carbon in γ-Fe with a face-centred cubic lattice. Iron carbide, or cementite with the chemical formula Fe_3C, is a compound of iron and carbon [24].

The eutectoid point in the equilibrium phase diagram determines the temperature and the given concentration at which, when cooled from a higher temperature, two different solid phases precipitate from the original solid phase. The eutectoid point for the

solid iron-carbon solution is defined by the parameters of 723°C and 0.76 wt. % of carbon, see Figure 3. Steels are divided into three types according to carbon content. Hypoeutectoid steel has a carbon content below 0.76 wt. %, followed by eutectoid steel with an approximate carbon content of 0.76 wt. % and hypereutectoid steel with a carbon content between 0.76 and 2.06 wt. % [11].

In addition to iron and carbon, a wide range of metallic and non-metallic elements are present in each steel. Elements intentionally added to the steel are referred to as alloys. On the other hand, impurities that contaminated the steel during production and processing are called accompanying elements. If accompanying elements degrade the properties of steel, they are referred to as impurities [25].

2.2.1 Steels grades

Steels can be divided into unalloyed and alloyed based on the content of alloying elements. While there is no exact weight percentage threshold for steel to be considered alloyed, this content is usually expressed in terms of tenths of weight percentage. Steels can be also divided based on their usage and mechanical properties [25]. Types of steels are defined by the standards of individual countries; this thesis will refer to the European EN ISO and the US ASTM standards. It is also important to mention that there are ČSN standards, well-established in the Czech Republic, which also clearly distinguish steels based on their usage. The standards distinguish between steels based on their classification, which then defines their minimum mechanical properties and chemical composition. These classifications are, for example, structural steels, steels for pressure vessels, tool steels or stainless steels.

Elements that have greater solubility in austenite stabilize γ-Fe and are called austenite-forming. These elements primarily include Ni, Mn, and Co, and to a lesser degree C, N, Zn, and Cu. These elements can stabilize γ-Fe at room temperature, or even significantly below it. Conversely, elements that are more soluble in ferrite stabilize α-Fe and are referred to as ferrite-forming. These elements mainly include Cr, Al, W, Mo, P, and V [24].

Furthermore, carbide-forming elements, which include in particular Cr, Mn, V, Mo, W, and Ti, significantly modify mechanical properties. They increase the strength, hardness, wear resistance, and heat resistance. In contrast, S, P, N, and O impair the formability and toughness of steels. The content of these elements is as low as possible

in modern steels. Cu increases corrosion resistance, but significantly reduces hot formability [24].

2.2.2 Phase transformations in steels

A phase transformation is a process in which an equilibrium heterogeneous system under the influence of external forces changes into another state with a different thermodynamic equilibrium. This change is accomplished by a moving part of the mass from one phase to another to equalize the chemical potentials [20].

Phase transformations of the first-order are accompanied by a change in volume and absorption or a release of phase or latent heat, as the change in entropy can be expressed as a fraction of heat and temperature. Examples of first-order phase transformation are, for example, melting, evaporation and crystal structure change. The first-order phase transformations that are most important for the present research involve entropy and volume change. As the volume increases, the entropy of the system also increases [20].

In second-order phase transformations, the second derivative of free enthalpy is a discontinuous function. In these phase transformations the crystal structure does not change. Examples of such transformations are, for example, the transformation from a normal to a superconducting state, or the transformation from a paramagnetic to a ferromagnetic state [20].

Even the simplest carbon unalloyed steel represents a thermodynamic multi-component system, which cannot be described in a similar way to the phase transformations of iron itself. Equilibrium binary diagrams can be used for thermodynamically stable systems. On the contrary, non-equilibrium diagrams are constructed for processes that run fast [23]. During laser processing, transformations occur first during material heating. For example, the ferrite structure in the heat-affected zone changes to an austenitic structure, which subsequently changes during cooling. Figure 4 shows a part of the equilibrium binary diagram around the eutectoid point, indicated by the letter S. In the figure, the thermal hysteresis of the iron-carbon system is indicated. Temperature A_1 determines the eutectoid conversion temperature, temperature A_3 determines the boundary between austenite and the ferrite-austenite mixture, and temperature A_{cm} determines the boundary between austenite and the cementite-austenite structure. However, the individual temperatures during heating and cooling are different

from the theoretical values, mainly due to the rapid temperature change and the unbalanced behaviour of the system. Therefore, the temperatures starting the transformation during heating are denoted by the index c and, conversely, the temperatures during cooling are denoted by the index f [24].

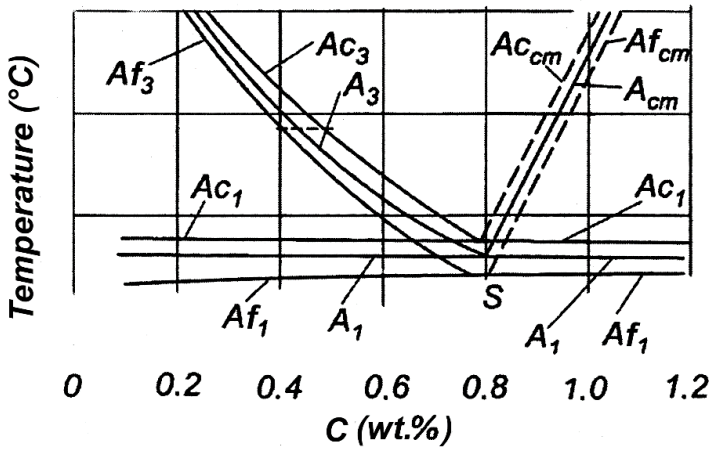

Figure 4: Temperature diagram for heating and cooling of steel [23].

The phase transformations during heating can be also described using a TTA (Time-Temperature-Austenitization) diagram, see Figure 5. If the required phase transformation is to be achieved, then a given temperature determined from the equilibrium binary diagram must be applied to our system for a long period of time. Conversely, when there is only a limited conversion time, a higher temperature must be reached. The thermal hysteresis described decreases with lower content of carbon and other impurities in the steel [11]. The effect of thermal hysteresis must especially be taken into account for products with small dimensions, during hardening processes, induction heating and laser processing.

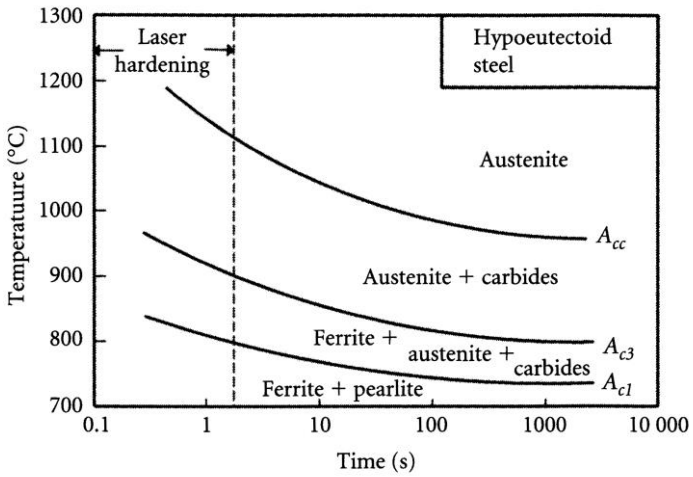

Figure 5: TTA diagram for hypoeutectoid steel [11].

Phase transformations in the material also occur during cooling. The transformations of austenite, especially when rapidly cooled, cannot be described by an equilibrium binary diagram. This transformation is described by a TTT (Time-Temperature-Transformation) diagram. A TTT diagram is shown in Figure 6. The cooling curves show the rate of cooling and consequently the formation of different phases from austenite. If cooling occurs slowly, phases corresponding to the phase diagram are formed, but when the cooling rate is accelerated, metastable phases such as martensite may form [11].

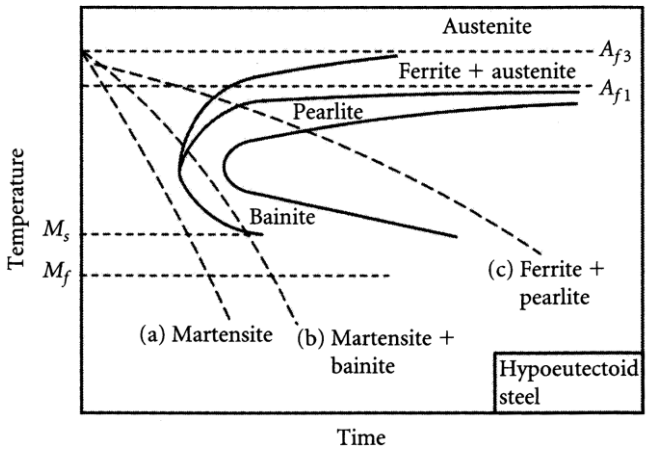

Figure 6: TTT diagram for hypoeutectoid steel [11].

2.2.3 Microstructure of steels

Using the metastable iron-iron carbide phase binary diagram in Figure 3, the microstructure of various steels can be predicted. Since the solubility of carbon in iron is

very low, the cooling of low carbon steels results in the formation of a ferritic structure and the precipitation of cementite at grain boundaries. When cooling the eutectoid steel, a perlitic structure is formed. This consists of a lamellar structure of two phases: ferrite and cementite. During the slow cooling of austenite, carbon diffusion and growth of new grains occur, where the layers of ferrite and perlite alternate. From a mechanical point of view, pearlite has the properties of both: it is soft and ductile due to ferrite and hard and brittle due to cementite. Furthermore, acicular ferrite can be described in steels, which is characterised by a needle-shaped microstructure. On the contrary, ledeburite consists of austenite and cementite grains [24].

As outlined in the previous section, if austenite is cooled at an increased rate, there is not enough time for the diffusion of carbon and other elements. This results in bainite, which is formed by acicular crystals of carbon supersaturated ferrite and fine cementite particles. At a lower cooling rate, upper bainite is formed, which is characterized by coarser grains of cementite, which are oriented in the direction of the ferritic grains. At a higher cooling rate, lower bainite is formed, which in turn shows fine cementite inside the ferritic grains. Due to the presence of fine carbide particles in the bainite structure, it shows a higher hardness than a pearlitic structure. The transformation from austenite is not complete, as the retained austenite remains in the structure [24].

If the cooling rate is high, diffusion almost does not take place, and a martensitic structure is formed by the phase transformation. This is characterized by a strongly supersaturated solid solution of carbon in α-Fe, which has a typical acicular structure. As a result, the unit cell shows body-centred tetragonal (bct) symmetry. The phase transformation described results in a unit cell with different lattice parameters a and c. The ratio of lattice parameters $a\ /\ c$ is strongly dependent on the mass representation of carbon in the steel. As a rule, the higher the carbon content, the higher the ratio of lattice parameters $a\ /\ c$. At low carbon contents in the material, usually below 0.3% by weight, the shape of the martensite lattice approaches that of a cube and its size corresponds to a ferrite lattice. If the austenite is rapidly cooled below the temperature indicated by M_s (martensite start), see Figure 6, the diffusion is suppressed and the conversion of austenite takes place without diffusion and a given proportion of martensite is formed in the steel. In order to form even more martensite, it is necessary to reduce the temperature further up to M_f (martensite finish). M_f is defined as the temperature below which martensitic

conversion no longer takes place. In the case of carbon steels, a cooling rate of up to 1000 K/s must be achieved in order to form a martensitic structure in the steel [23].

2.3 Real structure

Over the years, it has been proven repeatedly that properties of materials are determined not only by the phase composition and crystal structure, but very often the real structure plays an important role [2]. But what exactly do we mean by the real structure of crystalline materials? How does the real structure influence the properties of polycrystalline materials and the durability of products for which they were used?

There is no clear definition of real structure, but deviations from the perfect translational periodicity of crystalline structure are generally considered [2]. Firstly, the ideal polycrystalline material is composed of a large number of independently diffracting crystals, which have a random orientation [26]. Thus, if we consider a polycrystalline material, the real structure mostly includes lattice defects, coherently diffracted domain – crystallites, residual stresses and preferred grain orientation – texture [27].

2.3.1 Lattice defects

In real materials there are always certain deviations from the perfect translation periodicity; we call these deviations lattice defects. They are usually divided according to the spatial point of view into point, line, planar, and bulk defects [25].

The basic point defects in metals are vacancies and interstitials. If impurities are present in the metal, they form interstitials or substitutions. A vacancy occurs when an atom is missing in the lattice position. Conversely, an interstitial is formed by placing an atom in a position between lattice atoms. A substitution is the replacement of the metal by another type of atom. Elastic lattice deformations occur around point defects, resulting in a change in the lattice parameters of the material. For example, interstitial carbon atoms have a crucial role for the mechanical properties of steels [25].

The most important line defects are dislocations, which are either edge or screw. The movement of dislocations is important because it is associated with the plastic deformation of metals. The density of dislocations, which is given as the total length of dislocation lines in unit volume, strongly depends on the state of the material and increases with plastic deformation [23].

Planar defects include grain boundaries, interphase boundaries, and a crystal surface. Grain boundaries also significantly affect the properties of the material, since

they represent a place with an increased concentration of point and line defects. Therefore, there is faster diffusion and the material has less chemical resistance [23].

Bulk defects include pores, cracks or foreign particles called inclusions. The alloying elements also form phases, which are called precipitates, and remarkably affect mechanical properties [25].

2.3.2 Coherently diffracted domains – crystallites

It is necessary to distinguish between grains and coherently diffracted domains, which are referred to as crystallites. Grains exist due to the polycrystalline nature of the majority of metallic materials. As the metal solidifies, the nucleation of the crystalline phase occurs at multiple sites at once. Subsequently, these grains grow until they merge with each other. Because this process is random, grains with different crystal lattice orientations are formed. Furthermore, we can distinguish between small-angle and high-angle boundaries between grains, where small-angle corresponds to a disorientation of mostly up to 15° [25]. When observed in a light microscope or with an electron microscope, grain boundaries are observed which commonly amount up to several degrees. Using electron diffraction, a misorientation of two points greater than 5° is most often defined as the grain boundary.

In contrast, a crystallite is considered to be a domain that has an almost monocrystalline structure with a minimum of defects. It is therefore clear that a grain where the individual parts may differ from each other by several degrees is not the same as crystallite. The grain thus consists of an aggregate of randomly slightly rotated crystallites. Crystallites should be considered when using X-ray diffraction, as the method is very sensitive to changes in lattice parameters [21].

The size of the crystallites describes the state of the polycrystalline material, and in particular can indicate changes in its state after plastic deformation or the recovery process [27]. These changes strongly affect the mechanical properties of polycrystalline materials.

2.3.3 Residual stresses

The stress at the point of the elastic body is defined as the ratio of the magnitude of the elemental force and the elementary (very small) area on which the force acts. The stresses

act in the direction of the force, which may generally be oblique to the selected area. The applied stress can be divided into normal and tangential. If a rectangular system is selected, the stress can be divided into three normal stress components and six tangential stress components at the point of the stressed body. Positive normal stresses are called tensile and negative compressive stresses. The state of stress acting at any point of the elastic body can be unambiguously characterized by nine components σ_{ij} $(i, j = x, y, z)$ of the symmetrical stress tensor [22].

The application of external forces or moments to the system generates stresses, sometimes referred to as applied stresses. In contrast, residual stresses are contained in the body without external loads. Therefore, applied stress will only exist as long as external forces are applied. On the contrary, residual stresses remain even after their causes have been eliminated [22].

Residual stresses are classified according to different criteria. One possible division is according to the cause of origin. From this point of view, three most important types are distinguished - deformation, thermal, and transformation stresses. Deformation stresses originate from irreversible plastic and inhomogeneous deformations caused by external forces. Thermal stresses are generated by cooling due to different deformations in different regions of the body. Finally, transformation stresses arise from a spatially inhomogeneous transformation of a structure that is accompanied by volume changes [22].

The most common division of residual stresses in polycrystalline materials is the distribution according to the magnitude of the volume in which the stresses reach an equilibrium. Type I residual stresses (macroscopic) are approximately homogeneous in the macroscopic area of the material. They are therefore constant in both direction and size in large areas on the order of several millimetres, covering many crystallites. Macroscopic residual stresses reach equilibrium in the entire volume. If a body's force and torque fail to reach equilibrium, type I residual stresses always change. Type II residual stresses (microscopic) are approximately homogeneous in areas comparable to the size of individual crystallites. Microscopic stress represents a deviation between type I residual stress and the mean values of residual stresses in the individual crystallites. Microscopic residual stresses arise due to the incompatibility of deformations of individual crystallites. If the microscopic stress is divided by Young's modulus, a dimensionless number called microdeformation (often referred to in the literature as microstrain) is obtained. Type III residual stresses (submicroscopic) are inhomogeneous

in areas comparable to interatomic distances. Submicroscopic stresses correspond to the actual value of residual stresses at each point of crystallite and are caused by lattice defects in real crystals. Residual stresses always represent a superposition of all three types at a certain point. While type I and II residual stresses can be zero, type III residual stresses always occur in real crystals [27].

Residual stresses play a crucial role from a technological point of view as they have an impact on the corrosion resistance, the fatigue life, and other utility properties. Generally speaking, compressive macroscopic residual stresses decelerate crack nucleation, formation and propagation. For this reason, they prolong fatigue life [27].

It is worth mentioning that if crystallite size d and microdeformation ε are known, it is possible to obtain the dislocation density ρ from these values using the Williamson and Smallman method:

$$\rho = \frac{\sqrt{3K}\varepsilon}{db}, \tag{1}$$

where b is the Burgers vector and K is a constant [28]. For bcc crystal structure $K \sim 14.4$ and $b = a/\sqrt{2}$, where a is the lattice parameter.

2.3.4 Preferred grain orientation – texture

If the crystallites in polycrystalline materials are not randomly oriented, this phenomenon is called a preferential orientation or texture.

The formation of texture has many causes. In the case of polycrystalline substances, it is caused by uneven (preferential) growth of crystallites, mechanical processing and recrystallization. The most common textures include fibre and rolling textures. The fibre texture can be determined by a significant crystallographic direction $\langle uvw \rangle$ and the angle of rotation around it. Conversely, in a rolling texture, the sliding planes of the material $\{hkl\}$ are parallel to some significant plane of the sample and the directions $\langle uvw \rangle$ lie in this plane and are parallel to the significant direction of the sample [29].

The texture can be described by pole figures (PF), inverse pole figures (IPF) or orientation distribution function (ODF). The pole figures describe the orientation of a given crystallographic plane in space by using stereographic projection. In contrast, the inverse pole figures indicate the distribution of the significant sample direction with

respect to the crystal reference system (typically a standard stereographic triangle with crystallographic axes). The orientation distribution function describes the probability that a crystallite with a given orientation is present in a volume. In other words, it determines the volume density of the crystallites in a certain direction [29].

Not only mechanical and chemical properties, but also physical characteristics can differ depending on the direction in the textured material. Therefore, it is very important to describe the texture of the material and its impact on the material characteristics.

2.4 Experimental identification of the real structure using diffraction techniques

2.4.1 X-ray diffraction

X-ray diffraction in a crystal lattice is a physical phenomenon that can be used to determine its real structure, i.e. to characterize the phase composition of the material under investigation and determine residual stresses, preferred orientation or texture, and crystallite size [26].

X-ray scattering can also be interpreted as a reflection of photons on atomic lattice planes. An observable interference phenomenon (concentrations of diffuse energy in certain directions) occurs only when the waves scattered by atoms in lattice planes have the same phase. This is only achieved when the Bragg condition is met:

$$n\lambda = 2d_{hkl} \sin\theta, \tag{2}$$

where λ is the wavelength of the incident photons, θ the angle of the incident X-rays, n the order of reflection, and d_{hkl} the interplanar distance [30].

2.4.1.1 Debye-Scherrer method in the back reflection arrangement

The Debye-Scherrer method is shown schematically in Figure 7. A narrow monochromatic X-ray beam comes from direction P towards sample V at 90°, where X-ray diffraction occurs. This radiation is then collected on a flat detector [26]. Nowadays, classical film is no longer used, since imaging plates are much better processed by a scanner and then reused.

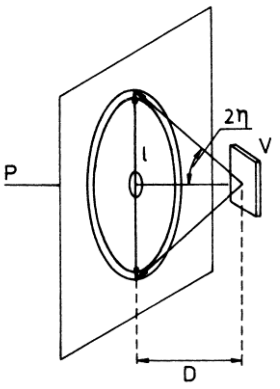

Figure 7: Debye-Scherrer method in the back reflection arrangement [26].

The ideal polycrystalline substance is composed of a large number of small, independently oriented crystallites. As a result, the crystallites distributed in such a manner are equivalent to the spherical rotation of a single crystal about the axis indicated by the incoming beam P. The conical diffracted radiation surfaces formed thereby correspond exactly to the interplanar distances. The diffraction lines, which are detected on the imaging plate, are the intersections of the aforementioned conical surfaces with the plane detector [26].

For the half of the vertex angle of cone surface 2η of Figure 7, the following applies:

$$\tan 2\eta = \tan(180° - 2\theta) = \frac{l}{2D}, \tag{3}$$

where l is the radius of the intersection, D is the distance of the sample from the detector, and θ is the angle at which a single crystal of the material would diffract the radiation [26].

The advantage of this method is primarily the ability to examine the surfaces of large and complex specimens. Another advantage is that the area under investigation is very small, on the order of mm^2. The described method is also relatively inexpensive.

The X-ray diffraction pattern obtained provides information on crystallite size. From this information it is possible to qualitatively estimate the crystallite size and texture, i.e. the preferred orientation of the crystallites of the investigated material [27]. This method is one way to obtain the Full Width at Half of the (diffraction) Maximum (FWHM) parameter. The FWHM parameter depends on microdeformation (fluctuation of inter-planar distances), crystallite size (size regions of coherent scattering), and density of dislocations. FWHM increases with increasing microdeformation and density of dislocations and decreasing crystallite size [27].

2.4.1.2 X-ray $\sin^2\psi$ method for determining macroscopic residual stresses

Stress applied to polycrystalline material results in an extension of each crystallite in the direction of the tensile stress and its compression in the perpendicular direction. This changes the interplanar distance of the lattice planes perpendicular to the tensile or compressive forces by $\pm\Delta d_{hkl}$. The change d results in a shift of the angular position θ of the interference maximum of diffracted radiation, which is defined by the Bragg condition (2) [22].

Using the relation

$$\varepsilon = -\frac{\Delta d_{hkl}}{d_0} = -\operatorname{cotg}\theta_0(\theta - \theta_0), \tag{4}$$

it is possible to determine the lattice deformation ε of the stressed crystal in the plane hkl, where d_0 is the interplanar distance of the unstressed material, and d of the stressed material, thus $\Delta d_{hkl} = d_0 - d$. The equation further defines the angular position θ_0 of the interference maxima of diffracted radiation on the unstressed material and θ of the stressed material [22].

Any deformation can act in a general direction. The direction of each such deformation can be defined by using a pair of angles φ and ψ to determine the lattice deformation $\varepsilon_{\varphi\psi}$. Thus, deformation is described by the equation:

$$\varepsilon_{\varphi\psi} = \frac{\nu + 1}{E}\sigma_\varphi \sin^2\psi - \frac{\nu}{E}(\sigma_{11} + \sigma_{22}), \tag{5}$$

where E is Young's modulus, ν is the Poisson number, σ_{ii} is stress in the given direction, σ_φ is stress in the direction given by angle φ in the plane of the material surface assuming $\sigma_{i3} = 0$ and ψ indicates tilt. The assumption that $\sigma_{i3} = 0$ is fulfilled due to the small penetration depth of X-rays into the material and thus the two-axis state of stress [22].

The basic $\sin^2\psi$ equation of stress measurement is introduced by identifying the lattice deformation ε with the deformation $\varepsilon_{\varphi\psi}$. X-ray elastic constants s_1 and $½s_2$ are defined by the equations:

$$½s_2 = \frac{\nu + 1}{E};\ s_1 = -\frac{\nu}{E}. \tag{6}$$

If the macroscopic constants E and ν are used, the correct value of the residual stresses is obtained only for materials which show no or little elastic anisotropy (for example W). For materials with more pronounced elastic anisotropy (e.g. for iron-based materials) it is necessary to use X-ray elastic constants, which are different for selected planes $\{hkl\}$. Their values can either be calculated theoretically or determined from an experiment where the sample is exposed to uniaxial tensile or bending stress [31].

By taking the derivative of (5) according to $\sin^2\psi$ the following equation is obtained:

$$\frac{\partial \varepsilon_{\varphi\psi}}{\partial \sin^2 \psi} = ½ s_2 \sigma_\varphi, \tag{7}$$

which shows that the slope of line $\varepsilon_{\varphi\psi} = \varepsilon_{\varphi\psi}(\sin^2 \psi)$ is proportional to the stress σ_φ. The principle of stress measurement by the $\sin^2 \psi$ method is shown in Figure 8. To determine the stress accurately, it is necessary to know the exact angular dependence $\varepsilon_{\varphi\psi}$ obtained by the diffraction on suitable planes $\{hkl\}$ for the direction given by the azimuthal angle φ [27].

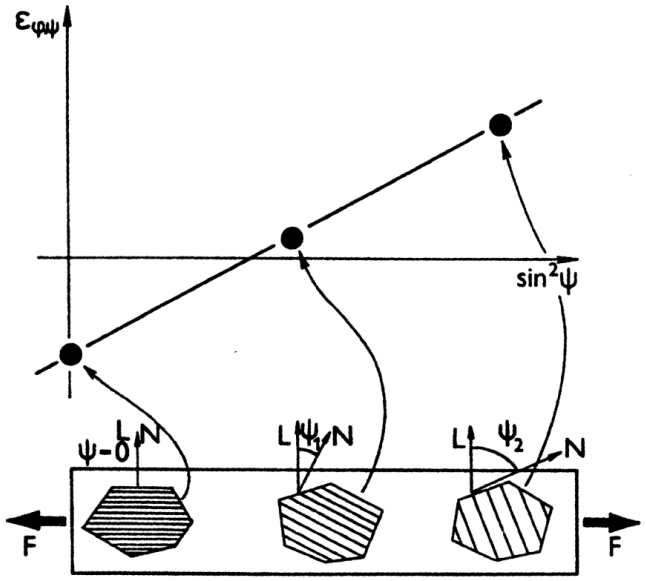

Figure 8: The principle of stress measurement by the $\sin^2 \psi$ method [27].

The advantage of this non-destructive method is the ability to detect a given stress in a given direction in a small area. The irradiated area may be less than 1 mm^2. Another advantage is the defined effective penetration depth of the radiation into the material. This can be changed by using X-ray tubes with different metal anodes. When evaluating the displacement of the diffraction maxima, only the elastic deformations in the material are determined. One disadvantage of this method is that it is limited to polycrystalline materials only. In addition, reliability decreases with increasing grain size. The texture of the examined material also negatively influences the results [27].

In equation (5) it is assumed that the two principal stress components σ_{11} and σ_{22} are identical to the principal axes of the coordinate system, i.e. the shear stress tensor components are zero $\sigma_{ij} = 0$, $i \neq j$. However, if the principal stress components are not identical to the coordinate system axes, equation (5) will be:

$$\varepsilon_{\varphi\psi} = \frac{\nu+1}{E}(\sigma_{11}\cos^2\varphi + \sigma_{12}\sin 2\psi + \sigma_{22}\sin^2\varphi)\sin^2\psi - \frac{\nu}{E}(\sigma_{11}+\sigma_{22}). \quad (8)$$

By taking the derivative of (8) according to $\sin^2\psi$ we obtain the following equation:

$$\frac{\partial\varepsilon_{\varphi\psi}}{\partial\sin^2\psi} = ½s_2(\sigma_{11}\cos^2\varphi + \sigma_{12}\sin 2\psi + \sigma_{22}\sin^2\varphi), \quad (9)$$

which shows that the dependence of $\varepsilon_{\varphi\psi}(\sin^2\psi)$ is uniquely determined by the main stress components σ_{11} and σ_{22}, the shear stress σ_{12}, the X-ray elastic constants s_1 and $½s_2$ and the direction φ. Relation (9) describes the so-called split, where different deformations are measured at the same large positive and negative values of the angle. The lattice deformation $\varepsilon_{\varphi\psi}$ depends not only on $\sin^2\psi$, but also on the relation $\sin 2\psi$ [22].

2.4.1.3 X-ray diffraction phase analysis

The interplanar distance of the atomic planes, i.e. the position of the maxima of the diffracted radiation on the measured diffraction diagram, is uniquely associated with the values of the parameters of the unit cell of the crystal lattice. The type and position of atoms in the unit cell influence the intensity of diffracted radiation, i.e. the relative intensity and position of maxima of diffracted radiation can be uniquely determined for each crystallographic phase. To determine the crystallographic phase or phases contained in the material to be examined, the interplanar distance and relative intensity are compared with the data already obtained, i.e. a pair of parameters (d_i, Y_i). Records in different crystallographic databases uniquely specify each known phase of any material. The most widely used database is the Powder Diffraction File, also known as PDF [32].

The diffraction phase analysis is traditionally divided into two areas, qualitative and quantitative. The first area deals with the qualitative analysis of the sample to determine which crystal phase the material contains. In the quantitative phase there is an effort to find out the percentage of individual phases. The ability to detect the presence of a given phase in a material during a qualitative analysis is determined by the volume of phases that are sufficient to produce a diffraction spectrum that the instrument is able to detect. This volume depends significantly on the element, its phase, and the composition of the mixture. When determining the individual phases, the real structure

affects the diffractogram and thus makes it difficult to determine the composition of the substance correctly [27].

The diffractogram of a given substance is obtained most often using the θ-θ goniometer. The recorded data are displayed in the form of a graph – diffraction diagram, where the value of 2θ is plotted on the x-axis and the value of the relative intensity of the measured diffracted radiation on the y-axis. From these values, the interplanar distance is determined using the Bragg condition (2). Subsequently, the values (d_i, Y_i) are used to determine which phases the substance contains. The measured diagram is a superposition of all diffractograms of individual phases. With a higher number of phases, it is more difficult to determine the sample composition as the individual diffraction maxima may overlap [33].

The Rietveld refinement method, which is based on the comparison of measured and calculated diffraction data, is most often used for qualitative phase analysis. The first step during Rietveld's refinement method is to determine the background. Different polynomials are commonly used, as it is possible to use a classical polynomial to a certain order or a special one like the Chebyshev polynomial [30].

The radiation coming from the X-ray tube contains a continuous braking spectrum and, for phase analysis, a more important characteristic spectrum. The characteristic spectrum contains several spectral lines, the most intense are $K_{\alpha 1}$, $K_{\alpha 2}$, and $K_{\beta 1}$. After passing the radiation through a suitably selected filter, known as the β filter, the intensity of the $K_{\beta 1}$ line is suppressed and the intensity of the continuous spectrum near wavelength $\lambda_{K_{\beta 1}}$ is reduced [26]. Rietveld's refinement method usually only considers lines $K_{\alpha 1}$ and $K_{\alpha 2}$ in its calculation and neglects the others [30].

The contribution to the calculated intensity can be divided into two parts. The first part is the instrument function, for which the instrument itself is responsible, while the second part of the intensity corresponds to the structure of the investigated substance itself. The main contributions to the calculated intensity are given in relation:

$$Y_i^{meas.} = K\, p_{hkl}\, L_\theta\, P_\theta\, A_\theta\, T_{hkl}\, E_{hkl}\, |F_{hkl}|^2 \ldots + Y_i^{background}. \tag{10}$$

The individual factors in relation (10) are as follows: K – scaling factor, p_{hkl} – multiplicative factor, L_θ – Lorenz factor, P_θ – polarization factor, A_θ– absorption factor, T_{hkl} – texture factor, E_{hkl} – extinction factor, and F_{hkl} – structural factor. With the help

of refinement parameters, a correction is made for various effects in order to obtain the best possible approximation of the measured diffraction data. The advanced parameters are: background, sample misalignment from the goniometer axis, profile function parameters, basic cell dimensions, texture, absorption, porosity, extinction, scaling factor, temperature factors, and the position and occupation of individual atoms in the unit cell. In this way, the real structure of the test substance is determined, and the mass representation of the individual phases in the irradiated volume is also determined [30].

Scaling factor K is used so that the normalized measured values correspond to the calculated absolute intensity, which is the total intensity diffracted by one unit cell at a given angle θ, which is defined by the corresponding length of the reciprocal lattice vector. Therefore, the scaling factor is constant for a given phase and is determined by the location of the diffraction centres and their state in the unit cell. The multiple factor p_{hkl} is responsible for the presence of more symmetrically equivalent points in the reciprocal lattice, i.e. it corresponds to the number of symmetrically equivalent reflections. The Lorenz factor L_θ is given by the geometry of the diffraction experiment used. The factor has two terms, where the first is related to the finite size of the points of the reciprocal lattice and the finite width of the Ewald sphere and is proportional to $1/\sin\theta$. The second term is related to the variable radius of the Debey rings and is proportional to $1/\sin 2\theta$. After adjusting and neglecting all the constants that go into the scaling factor, the Lorenz factor is expressed as:

$$L_\theta = \frac{1}{\cos\theta \sin^2\theta}. \tag{11}$$

The polarization factor P_θ corresponds to the polarization, which corresponds to the scattering on the electrons. The two previous factors are combined into a single Lorenz-polarization factor LP, which is given by the relation

$$LP = \frac{1 + \cos^2 2\theta}{\cos\theta \sin^2\theta} \tag{12}$$

provided that an incident X-ray monochromator is not used [30].

The absorption factor A_θ corresponds to the absorption of radiation in both the primary and diffractive beams. The factor also takes into account the properties and possible porosity of polycrystalline samples. The texture factor T_{hkl} describes the number of possible deviations from the assumed random orientation of the individual crystallites.

It is most often used to describe the texture factor of the March-Dollas function. The extinction factor E_{hkl} takes into account deviations from the classical kinematic theory of diffraction. For powder samples, the extinction factor is usually small and neglected, the situation is different for perfect or mosaic-like crystallites, where the phenomenon of primary and secondary extinction can be observed. The primary extinction is caused by further diffraction of an already diffracted beam in the same crystallite on the same plane system. The secondary extinction is caused by further reflection on another mosaic crystallite. The structural factor F_{hkl}, or the structural amplitude, is determined by several parameters that define the crystal structure of the material. It is mainly the distribution of individual types of atoms in the unit cell and their thermal motion. If the unit cell contains more atoms that have different scattering ability, then the amplitude of the scattered wave is given by a complex function in the form:

$$\vec{F}(\vec{h}) = \sum_{j=1}^{n} g^j t^j(s) f^j(s) \exp\left(2\pi i \vec{h} \cdot \vec{x}^j\right). \tag{13}$$

The individual terms of equation (13) are described below. The structural amplitude $\vec{F}(\vec{h})$ with indices hkl, which are represented as a vector $\vec{h}$, n is the total number of atoms in the unit cell and includes all symmetrically equivalent atoms. The length of diffraction vector s is given by the dependence $\sin\theta^{hkl}/\lambda$. The factor g^j represents the population factor of the j-th atom. For a fully filled position, $g = 1$. The temperature factor t^j, which is also dependent on the diffraction vector, describes the temperature motion of the j-th atom. The atomic scattering factor f^j, which is also dependent on the diffraction vector, indicates the interaction of a given atom with X-rays. Finally, the scalar product $\vec{h} \cdot \vec{x}^j$ is the product of two vectors, where the vector $\vec{x}^j$ represents the coordinates of the j-th atom in the unit cell [30].

To compare the quality of approximation, the most commonly used weighted profile residual factor is applied:

$$R_{wp} = \left[\frac{\sum_{i=1}^{n} w_i \left(Y_i^{meas.} - Y_i^{calc.}\right)^2}{\sum_{i=1}^{n} w_i (Y_i^{meas.})^2}\right]^{\frac{1}{2}}. \tag{14}$$

Where n is the total number of measured points, $Y_i^{meas.}$ is the observed intensity of the i-th measured point, $Y_i^{calc.}$ is the calculated intensity of the i-th measured point, and w_i is the weight of the i-th data point, which is usually taken as the inverse of the intensity

observed. This formula corresponds to the application of the Poisson statistical distribution to a statistical set of measured data [30].

2.4.2 Neutron diffraction

A thermal neutron beam (wavelength 0.1 to 0.2 nm, energy 80 to 20 meV) can be used for diffraction experiments, which can also be interpreted as reflection of the neutrons on atomic lattice planes using the Bragg condition (2) [34].

The use of neutrons in diffraction has several specific differences from X-ray diffraction. Compared to X-rays, the absorption of neutrons is significantly lower for most materials (except B and Cd). This can be used in the research of metallic materials, as it allows the study of larger samples and non-destructive analysis to greater depths (a few micrometres for X-ray diffraction vs. a few centimetres for neutron diffraction) [26].

Another difference is that X-rays are coherently scattered on the bound electrons of the atom, the nucleus practically does not participate in the scattering. Conversely, with the exception of magnetic substances, neutrons are scattered only on nuclei. Since the radius of the nucleus is several orders of magnitude smaller than the wavelength of the thermal neutrons, the amplitude of the scattered wave does not depend on the angle, so the scattering is isotropic (spherically symmetric) [26].

Further, we observe the potential scattering of neutrons on the nucleus and also resonance scattering. This is due to the temporary connection of the neutrons to the nucleus. This makes it possible to distinguish light atoms in crystals containing heavy atoms and to distinguish the positions of atoms with close proton numbers.

For elements with an unfilled 3d electron shell, such as Fe, Co, and Ni, an interaction between the resulting magnetic moment of the atom and the magnetic moment of the neutron can be observed. This magnetic scattering can be compared in size with nuclear scattering, thus creating additional diffraction maxima on the diffraction pattern [26].

Due to the above-mentioned specifics, neutron diffraction finds its application in structural analysis, in the study of the arrangement of magnetic moments, in the description of textures and much more. From a technical point of view, the use of neutron diffraction for the analysis of residual stresses is very interesting, due to the greater depth of penetration.

2.4.2.1 Neutron tensometry

The principle of neutron tensometry is the same as for X-ray diffraction. The shift of diffraction maxima can be used to deduce local changes of the lattice parameter, which can then be converted to deformation, see equation (4). However, due to the non-negligible penetration depth of the neutron beam, it cannot be assumed as in X-ray tensometry that the tensor component σ_{i3} is zero. In general, to obtain the entire stress tensor, it is necessary to perform 6 measurements in independent directions. Under these assumptions, equation (5) cannot be used and the deformations measured can then be recalculated using generalized Hooke's law to obtain macroscopic stresses:

$$\begin{aligned}\varepsilon_{\varphi\psi} = \frac{d_{\varphi\psi} - d_0}{d_0} \\ &= ½s_2^{hkl}\,(\sigma_{11}\cos^2\varphi + \sigma_{12}\sin 2\varphi + \sigma_{22}\sin^2\varphi)\sin^2\psi \\ &+ ½s_2^{hkl}\,(\sigma_{13}\cos\varphi\sin 2\psi + \sigma_{23}\sin\varphi\sin 2\varphi + \sigma_{33}\cos^2\psi) \\ &+ s_1^{hkl}(\sigma_{11} + \sigma_{22} + \sigma_{33}),\end{aligned} \tag{15}$$

where the elastic constants s_1^{hkl} and $½s_2^{hkl}$ are associated with given planes $\{hkl\}$. Consequently, the least squares method for fitting can be used to calculate stresses as fit parameters. Sometimes analysis in only three significant directions of the sample is used to determine residual stresses, thus we obtain only three main components of the tensor without shear stresses [34].

Another problem is the determination of d_0 from equation (15). 'Stress-free' samples are used for this, where it is most advantageous to use a powder of exactly the same material as being analysed. The problem is when the chemical and microstructural composition of the sample changes within the analysed area, such as welds or clads. Another possibility is to use the fact that the integral of the residual stresses over the whole body is equal to zero and thus the average interplanar distance of the whole body corresponds to d_0. Again, this approach cannot be used for complex shapes. In this case, it is possible to use parts of the analysed sample, where they are cut so that the macroscopic stresses are released (e.g. the shape of the comb). Alternatively, d_0 could be determined from a place that is probably only minimally affected by the process that introduced residual stresses into the material (e.g. the edge of the welded plate). Another option is to use equilibrium conditions. This approach requires that force and moment must balance across any selected cross-section [35].

Another consequence of the greater penetration depth is the need to define the irradiated volume. When solving technical problems, the smallest possible irradiated volume is required, from which the average value of macroscopic residual stresses is obtained. Slits of incident and diffracted radiation are used to define the shape and size of the irradiated volume. The volume is best defined at an angle of $2\theta = 90°$ [34].

2.4.3 Electron microscopy

The resolution of the microscope increases with decreasing wavelength of the applied radiation. Using an accelerating voltage in the order of tens and hundreds of kV, we can achieve a resolution of 0.1 nm in high-end transmission electron microscopes, which is comparable with the interatomic distance [25].

When a primary electron beam irradiates the sample, several effects occur, see Figure 9. If the sample is thin enough, some of the electrons will transmit, they are scattered due to interaction with the solid. Part of the electrons is absorbed and part is elastically reflected, these are the backscattered electrons (BSE). Primary electrons can eject a valence electron, creating secondary electrons (SE). The empty energy level is filled with an electron from a higher level while emitting a characteristic X-ray photon. If the energy is not radiated by a photon, it can be transferred to another electron and an Auger electron (AE) leaves the atom. Accompanying phenomena include cathodoluminescence and electromotive force [36].

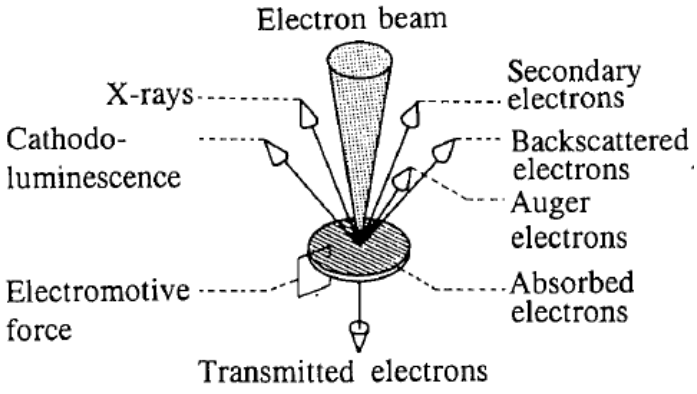

Figure 9: Effects accompanying the irradiation of a solid state by an electron beam [37].

We distinguish two types of electron microscopes, scanning electron microscopes (SEM) and transmission electron microscopes (TEM). A SEM scans the sample surface

and the backscattered or secondary electrons are analysed. By changing the intensity of the secondary electrons, which are more dependent on the inclination of the sample, a topological contrast is created. On the contrary, backscattered electrons are more dependent on the atomic number of the elements present, thus, material contrast occurs [25].

In a transmission electron microscope the beam passes through a thin sample, and transmission electrons can be observed. The image forms an absorption contrast due to the different thickness of the sample and then the scattering of electrons caused by the structure, different chemical composition, defects, etc. [36].

Due to the small penetration depth of electrons, which is given by their charge and small weight, they are suitable for the study of surfaces. The effects that arise when the electron beam irradiates a thick sample, their interpretation, the approximate volume, and depth from which the information comes are shown in Figure 10. From the smallest depth come AE, which can be used to study the composition of the surface. SE that describe the surface topology are detected from a greater depth of about 100 nm. The phase differences can be determined using BSE, which comes from a depth of about 500 nm. X-rays can be detected from a few micrometres, which can be used to determine the chemical composition [38].

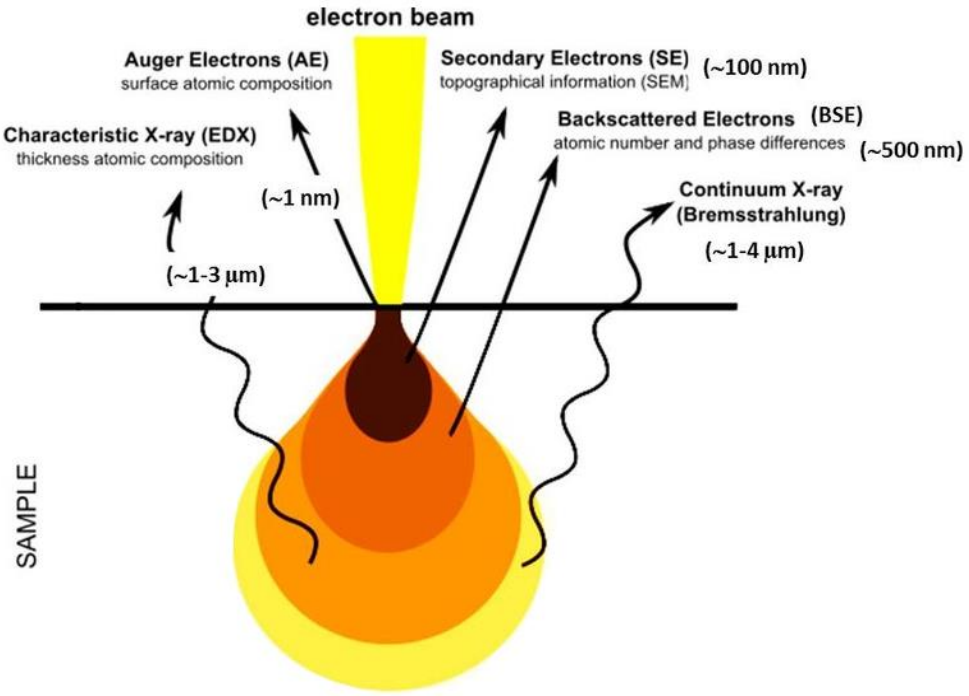

Figure 10: Effects and penetration depth of electron beam [38].

2.4.3.1 Electron backscattered diffraction (EBSD)

Electron backscattered diffraction (EBSD) can be used to investigate phase composition, texture, grain morphology, defects, and deformations. The principle is shown in Figure 11 (b). An electron beam irradiates a flat, well-polished sample at a low angle of approximately 20°. Some backscattered electrons satisfy Brag's condition (2) and diffraction occurs. This creates diffraction cones with a large apex angle which, when projected on the phosphor screen of the camera, form Kikuchi bands. Each band corresponds to a family of crystallographic planes. Each pattern, see Figure 11 (a), consists of many differently oriented bands, which form the tops of triangles at their intersections [39]. The volume where the information comes from is therefore determined by the depth from which BSE are detected and the geometry of the apparatus, see Figure 11 (b). In general, at an accelerating voltage of about 15 kV, the width of interaction volume is twice the spot size, the length is three times the spot size and the depth is up to 100 nm. In addition, the spot size is at the top of the interaction volume due to tilt. Most SEM can generate an electron beam with a spot size less than 10 nm in diameter. This fact is important when scanning a phase interface [40].

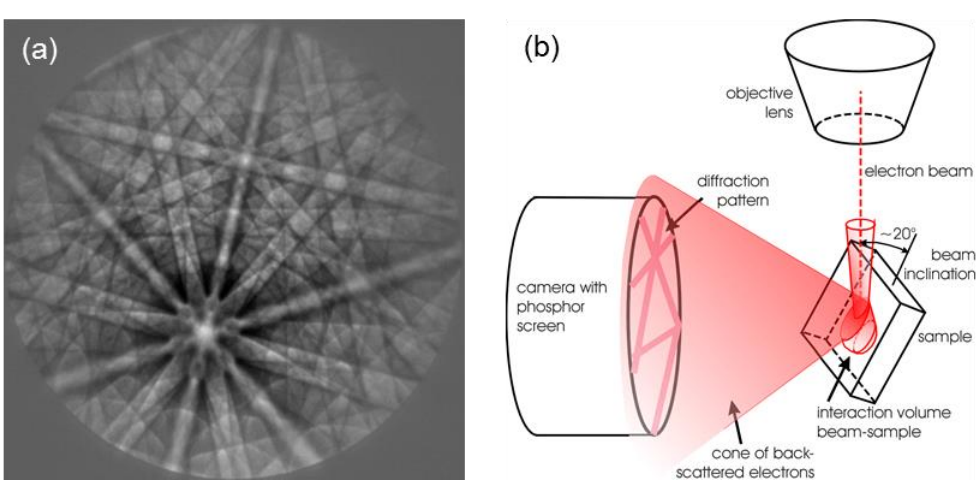

Figure 11: (a) An electron backscatter diffraction pattern, (b) Principle of electron backscattered diffraction [41].

Indexing takes place using a Hough transformation, which converts the straight bands from lines to points. With knowledge of the experimental geometry, the peak locations can be converted to a table of interplanar angles and compared with look up tables of expected angles for the phases present within the sample. It is important to mention that the indexing program searches only within the phases that have been pre-

selected for it, it cannot determine them itself [39]. With modern systems, pattern capture and indexing can be performed very rapidly and a detailed mapping of the sample crystallography (crystal type, crystal orientation, pattern quality, etc.) can be obtained. This creates maps of the scanned surface, which provide rich information of the sample microstructure; this process is referred to as orientation imaging microscopy (OIM) [42].

The grain boundary is defined as the boundary between two neighbouring scanning points having crystallographic misorientation larger than certain angle, often 5, 10 or 15 degrees are used. Only points with a certain confidence index are taken into account in the evaluation. The confidence index is based on a voting scheme during automated indexing of the diffraction pattern where it is counted as a ratio of votes for the best solution minus votes for the second-best solution divided by the total possible number of votes from the detected Kikuchi bands. A certain crystallographic orientation receives a vote when the observed angles between the three bands are the same as the table values of the given orientation. A confidence index of 0.05 for a face-centred cubic material corresponds to approx. 70% probability of correct indexing [42].

The main results are phase composition maps and inverse pole figures (IPF). To obtain a Grain Average Misorientation (GAM) map, misorientation between each neighbouring pair of points within the grain is calculated. The average misorientation value is then determined and assigned to every point within the grain. Unlike that, the Kernel Average Misorientation (KAM) value is the average misorientation with respect to the first, second, third, etc. nearest neighbour of the given point with a maximum corresponding to the grain boundary. Both GAM and KAM maps are good indicators of microstrain and density of geometrically necessary dislocations. Image Quality (IQ) describes the quality of an electron backscatter diffraction pattern. It is related to the perfection of the crystal lattice in the diffracting volume. In other words, the parameter depends on microstrain, presence of precipitates, grain boundaries, concentration of crystallographic defects (mainly dislocations), crystallographic orientation and roughness of the surface [42] [43] [44].

2.4.3.2 Energy-Dispersive X-ray Spectroscopy (EDS)

Energy-dispersive X-ray spectroscopy (EDS) is an analytical technique used for elemental analysis or chemical characterization. As already mentioned, an electron with sufficient energy can excite the nucleus, thus ejecting an electron. Subsequently, during the transition to the ground state, i.e. the transition of the electron from a higher level to

a lower one, a characteristic spectrum of X-rays is emitted. Due to the interaction of atoms in the solid, the higher energy levels split, each element has characteristic transitions between energy levels according to which it is possible to identify it unambiguously. The number and energy of photons can be measured using an energy-dispersive detector, thus the chemical composition in the interaction volume can be determined [36].

To excite the transition between energy levels, it is necessary for the primary electrons to be accelerated to a higher energy than the one which corresponds to the given transition. The overvoltage ratio is the ratio of the energy of the primary electrons in the beam to the ionization energy of the transition. Therefore, the overvoltage ratio must be higher than one. Furthermore, the number of electrons generated increases as this ratio increases, reaching a maximum for the value of 2.7 and then decreasing slightly. High-value accelerating voltages are also not suitable, because in that case low energies are less distinguishable. Therefore, it is necessary to correctly select the accelerating voltage based on the elements presumed to be present in the examined sample [45].

Figure 10 shows the approximate shape of the interaction volume where the information comes from. It should be emphasized that this volume is several times larger than that used in EBSD, and this fact needs to be considered during parallel EBSD and EDS analysis.

2.5 Other experimental techniques

Other non-diffractive methods can be used to analyse the real structure and its manifestations. A description of individual methods that were used to study laser-cladded steel is given in the following chapters.

2.5.1 Metallographic analysis

Metallography deals with the study of the structure of materials using metallographic microscopes, which can use light or electrons. The purpose of metallographic imaging methods is to determine which structural phases the material contains, along with the amount, distribution, and shape of these phases [23].

The observation of the structure is performed on a metallographic cut. In order to be able to use the maximum resolution of the microscope, it is necessary to carefully prepare the metallographic cut. The surface intended for material observation must be perfectly flat, so it is first ground and polished. Subsequently, the structure of the observed surface is prepared in a suitable manner. When cutting, grinding, and polishing test specimens, the structure must not change, either due to deformation or heating. Structural changes due to heating particularly occur in materials which are at nonequilibrium at normal temperatures. A test specimen of suitably large dimensions is machined by conventional machining methods or electroerosion machining. The most commonly used machining methods are sawing, turning, milling, and cutting. The sample must be strongly cooled with a suitable medium to avoid the previously mentioned change in structure [23].

Unsuitably small samples are poured into a resin, properly labelled, and then another grinding operation is performed. This is done first on a mechanical grinder and then the surface is sanded with sandpaper or an abrasive with decreasing grain size. Subsequent polishing is essentially a continuation of grinding, in which the samples are ground with a fine powder dissolved in an aqueous suspension, which covers the fabric of the rotating wheel. When grinding and polishing the sample, material is removed from the surface, which is deformed, but also thermally affected to a certain depth. Thus, an undesired layer is formed on the surface, which can be removed, for example, by electropolishing [25].

After polishing, various structural defects, cavities, colourless non-metallic inclusions or other inhomogeneities can be observed on the surface. The actual structure, i.e. the individual grains of the metal phases, is not visible. The most common way to make the structure visible is chemical etching. Chemical etchants can reveal either the macrostructure or microstructure of the investigated material [23].

Non-uniformities of larger dimensions are detected using an etchant that reveals macrostructure. The substance acts in greater depth and usually selectively attacks areas with increased energy, especially grain boundaries, twin boundaries, dislocations, inclusions, etc. This type of etchant also reveals dendritic or other structure, crystal orientation or plastic deformation [23].

An etchant revealing microstructure acts only on a weak surface layer and on the surfaces of individual grains and their boundaries. The type of chemical is selected according to the type of alloy being observed, the most common type being alcoholic acid solutions. A two to four percent solution of nitric acid in alcohol, called nital, is most commonly used to reveal the microstructure of ferritic steels. Nitric acid itself is also a frequently used etchant [25].

2.5.2 Tensile testing

When a force is applied to a material, it is deformed. Tensile tests are most often used to describe the deformation behaviour. The test specimen is loaded with an increasing force, while at the same time relative elongation is measured. The course is plotted in a stress–strain curve, see Figure 12 a). The engineering stress σ is plotted on the y-axis, which is defined as the ratio of the force to the initial cross-section of the test specimen. The x-axis shows the relative elongation ε of the sample as a percentage. There are two areas in the tensile diagram. The first region corresponds to elastic deformation and the second region to permanent (plastic) deformation. In the elastic region, the material deforms elastically, i.e. it returns to its original shape after unloading. In this area, the dependence of stress on relative elongation is linear, it is described by Hooke's law:

$$\sigma = E\,\varepsilon, \tag{16}$$

where E is Young's modulus [25].

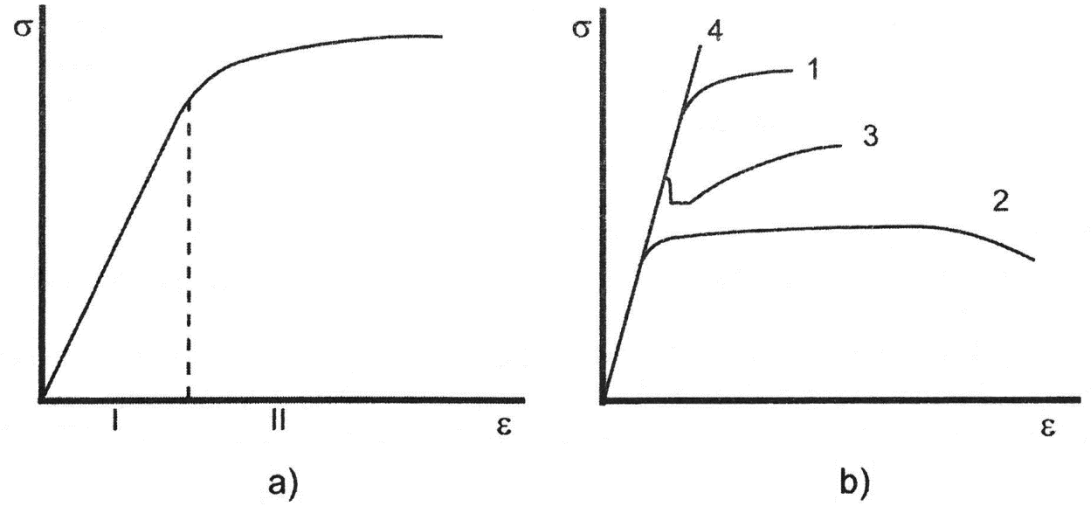

Figure 12: Stress–strain curve for metallic materials: a) area of elastic (I) and plastic deformation (II); b) possible courses of diagrams (1 – solid material, slightly plastic, 2 – more plastic material, 3 – material with a significant yield strength, 4 – brittle material) [25].

In the plastic area, the material does not return to its original shape after unloading. Plastic deformation of metals takes place by slip. This mechanism can be explained by the mutual displacement of two parts of the crystal along the slip plane by means of dislocations. Figure 12 b) shows different stress–strain curves for metallic materials. Curve 1 describes the behaviour of a material that is solid and slightly plastic, curve 2, on the other hand, shows a plastic material. A material with a significant yield strength exhibits the shape of curve 3 while a brittle material corresponds to curve 4 [25].

An important material parameter corresponding to the maximum stress that can be applied to a material in tension is the ultimate tensile strength. Yield strength is the stress at which plastic deformation begins. This is very important information that limits the amount of operational stress to prevent irreversible deformations. For many materials, the transition between elastic and plastic behaviour is smooth and blurred. In this case, the offset yield point (or proof stress) is defined. This is the stress at which the plastic deformation reaches a prescribed value, most often 0.2%. The yield strength is then referred to as $R_{p0.2}$ [25].

2.5.3 Hardness tests

Hardness is an important mechanical property that is most often defined as the resistance of the test specimen to surface deformation caused by a foreign body. Hardness tests are very often used in practice, mainly for their simplicity and speed [46].

There are a large number of hardness tests, which depending on the principle used can be divided into scratch, rebound, and penetration tests. Another distribution can be classified according to the speed at which the indenter acts on the test sample. A distinction is therefore made between static tests (most penetration methods) and dynamic tests (for example, the rebound method) [46].

The most important and most frequently used are penetration hardness tests, in which a suitable indenter is pressed into the examined sample with the prescribed force and then the shape and dimensions of the resulting impression are evaluated. The following is an overview of individual methods with the type of indenter indicated in parentheses: Brinell method (ball); Vickers method (pyramid); Knoop's method (pyramid); Rockwell method (cone, ball) [47].

2.5.3.1 Vickers hardness test

The indenter pushed into the test material in the Vickers hardness test is a diamond quadrilateral pyramid with an apex angle of 136°. To evaluate the hardness, it is necessary to measure the diagonals of the impression. The great advantage of this method is the independence of the hardness value from the load force. The normal loading force is 294 N, the loading time depends on the type of material under investigation [47].

2.5.3.2 Microhardness

Microhardness measurement methods are used to determine the hardness of very small areas, small components, thin films or coatings. Alternatively, it is also possible to measure the hardness of structural components and certain places in the structure. The principle of microhardness measurement is identical to the hardness measurement using the Vickers method, where the loading force of the pyramid indenter ranges from 4 mN to 2 N.

Microhardness and hardness are determined as the ratio of the magnitude of the test load in kilograms and the impression area in square millimetres. The measurement itself is performed on microhardness testers, which are usually connected to an optical metallography microscope to measure the size of the impression created.

The value of hardness and microhardness H is supplemented by a symbol indicating the indenter used. The hardness measured according to Vickers has the symbol HV. The load force is given after the HV symbol in kiloponds, if a normal force of 30 kp is selected, then the value is not given. One kilopond is by definition equal to 9,807 N. The hardness measured according to Rockwell with cone indenter has the symbol HRC [23].

2.5.3.3 Instrumented indentation (nanoindentation) testing

Unlike conventional hardness testing, instrumented indentation does not measure the size of the residual imprint after the test, but the course of the load and the depth of the indentation depth are recorded. The great advantage of this method is the ability to analyse coatings and thin layers, which are difficult to analyse by classical indentation techniques [48].

In instrumented indentation, an indenter of known geometry is driven into the area of the sample to be examined. At a pre-set speed, the indenter is pushed into the material until it reaches a pre-set load or maximum depth. The load is then reduced to zero at the same rate. The mechanical properties of the analysed area can be determined from the resulting dependence of the load versus indentation depth, see Figure 13. Hardness and elastic modulus can be calculated from this dependence using established models [49].

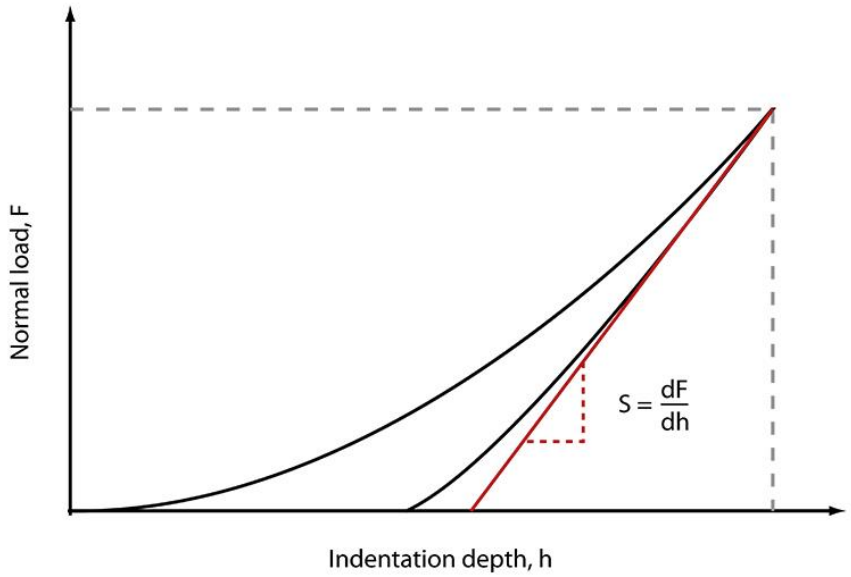

Figure 13: Load versus indentation depth [50].

Figure 14 describes the elastic-plastic response of the material to the indenter imprint, it can be seen that the measured depth h_m is not identical with the contact depth h_c of the Berkovich tip. The contact depth can be calculated according to ISO 14577 using the following equation:

$$h_c = h_m - \varepsilon \frac{F_m}{S}, \tag{17}$$

where h_m is the maximum indentation depth, F_m the maximum load, ε is a constant related to the indenter geometry, and S is the sample's stiffness calculated from the unloading of the indentation curve, see Figure 13 [49].

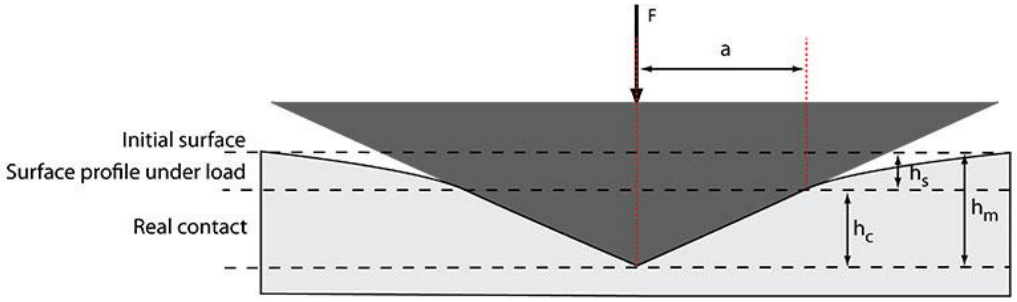

Figure 14: A schematic representation of indentation depth during loading [50].

To calculate the hardness, it is necessary to determine the indenter area function A_p, which in the first approximation corresponds to the equation:

$$A_p = C_0 h_c^2, \tag{18}$$

where the constant C_0 depends on the shape of the indenter used (for example $C_0 = 24.5$ for a Berkovich indenter). However, the tips do not have an ideal shape, so it is necessary to specify this value by precise analysis of the tip or by measuring the hardness of a known material. Finally, the instrumented hardness is expressed by the ratio between the applied load F_m and the contact area A_p [49]. In this case, the hardness symbol H is usually accompanied by the subscript IT, which means instrumented hardness testing. The hardness is given in MPa. To obtain hardness in HV, it is necessary to divide the hardness by a factor of 9.807, which corresponds to one kilopond, and multiply by a geometrical factor to convert the contact area A_p to developed area corresponding to the hardness measurement using a Vickers indenter.

2.5.4 Wear tests

An important area to be addressed is tribology, which examines the processes involved in the movement of two or more materials. When materials interact, material is lost from surfaces and a process known as wear occurs. Since cladding creates a new functional surface, usually with better mechanical properties than the base material, the description of wear resistance of the resulting surface is very important [5].

The wear characterization of materials is performed using various types of tribometers, while the pin on disk test is probably one of the most common, see Figure 15. A stationary pin is pressed with a defined force against a disk which is rotating. During the test, the friction coefficient, the position of the arm with the pin, and the temperature are usually recorded. The pin can have any shape, but a spherical shape is usually used, as this avoids the problem of inhomogeneous loading (a flat surface pin must be exactly perpendicular to the disk). After a certain number of cycles, which is usually determined by distances, the test ends. The distance that the pin travels on the disk is given by the radius R_t and the number of revolutions. After the test, the topology of the worn pin and the disk is determined. Data is used to calculate the worn volume per unit distance and applied force for the pin and per revolution and force for the disk. These standard values can then be compared [51].

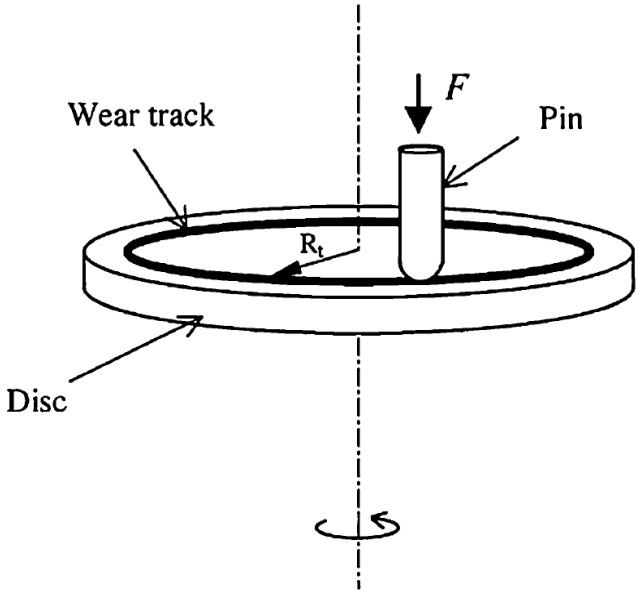

Figure 15: Pin on disk wear test [52].

3 Laser cladding of H13 tool steel in the literature

3.1 H13 tool steel

H13 tool steel is a Cr-Mo-V alloy steel with high hardenability and toughness as defined by standard ASTM A681 (grade 1.2344 or X40CrMoV5-1 according to EU standard EN ISO 4957, 19 554 according to ČSN, or grade SKD61 according to Japanese standard JIS G4404). It is characterized by very good strength properties and high resistance to wear at high temperatures. The steel has good thermal conductivity, resistance to hot cracking and low sensitivity to sudden changes in temperature, which allows water cooling. It has particularly good hardenability in air and vacuum. Under certain conditions, it can be hardened in water. After hardening, it shows small dimensional deformations. In addition, it even has good machinability [53]. Table 1 shows the range of permissible chemical composition of steel according to different standards, the values are similar, but greater tolerances are for ASTM A681. The TTT diagram in Figure 16 describes the achieved hardness and microstructure at different cooling rates. After hardening, tempering to the required hardness according to Figure 17 is required. Tempering must be always performed twice with a minimum holding time of 2 hours. After hardening, retained austenite also occurs in the steel structure, which decomposes at higher tempering temperatures [54]. The mechanical properties of H13 steel depending on the hardness are given in Table 2.

Table 1: Chemical composition of AISI H13 steel according to ASTM A681 [55] and 1.2344 according EN ISO 4957 [56].

	Cr [wt. %]	Mo [wt. %]	Si [wt. %]	V [wt. %]	Mn [wt. %]	C [wt. %]
H13	4.75–5.50	1.10–1.75	0.80–1.25	0.80–1.20	0.20–0.60	0.32–0.45
1.2344	4.80–5.50	1.20–1.50	0.80–1.20	0.85–1.15	0.25–0.50	0.35–0.42

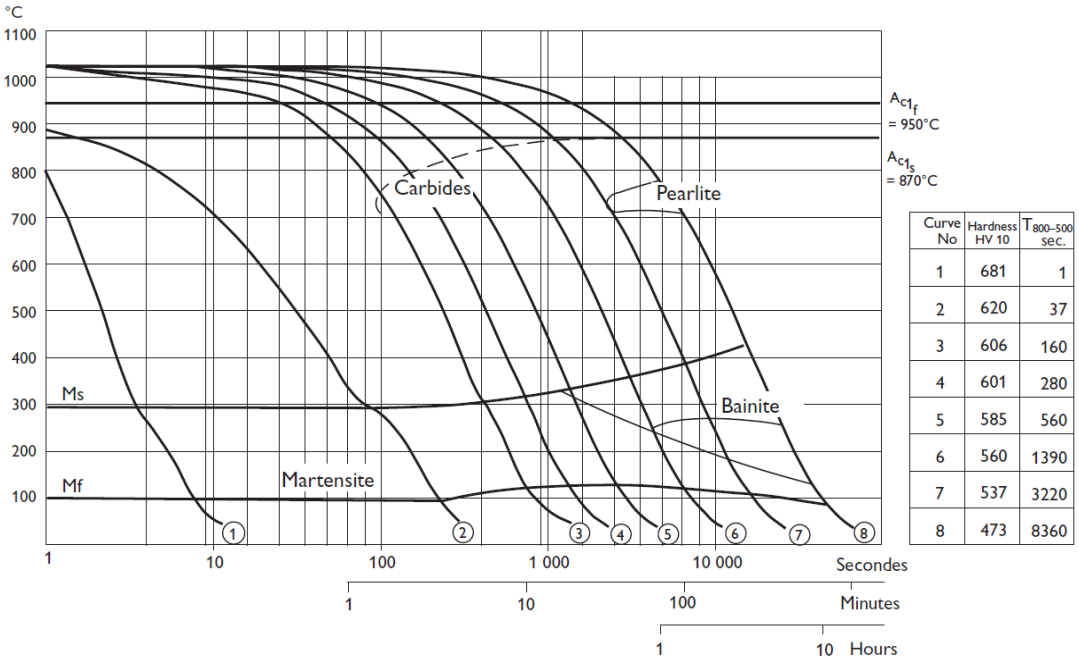

Curve No	Hardness HV 10	$T_{800-500}$ sec.
1	681	1
2	620	37
3	606	160
4	601	280
5	585	560
6	560	1390
7	537	3220
8	473	8360

Figure 16: TTT diagram for H13 steel with achieved hardness and microstructure for different cooling rates and austenitizing temperature 1020°C [57].

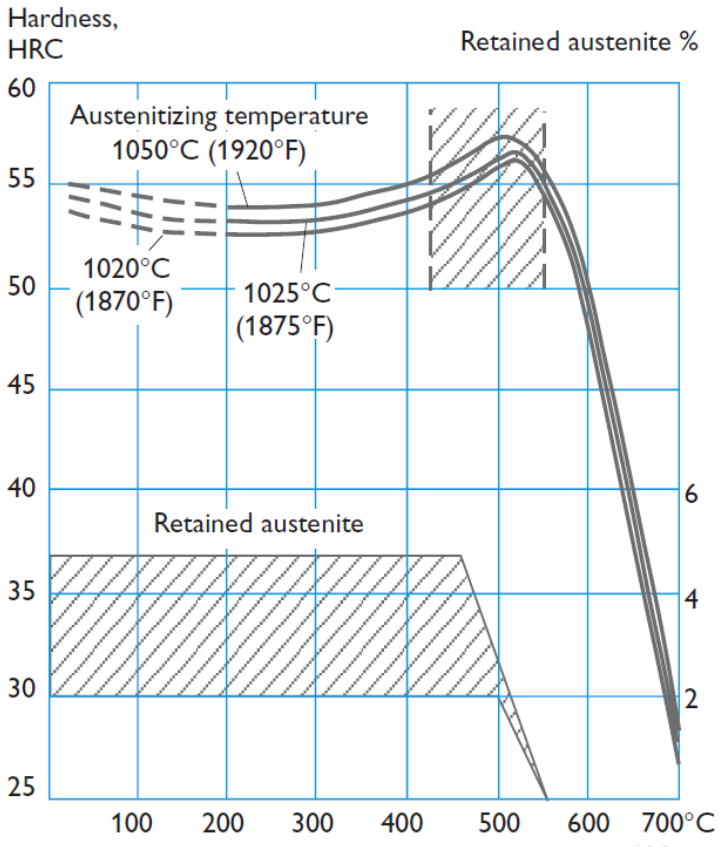

Figure 17: Tempering diagram for H13 steel [54].

Table 2: Mechanical properties of H13 steel [57].

Hardness	550 HV (52 HRC)	450 HV (45 HRC)
Tensile strength, R_m	1820 MPa	1420 MPa
Yield strength, $R_{p0.2}$	1520 MPa	1280 MPa

Universally applicable H13 steel is used for hot stamping tools and die casting moulds. It is mainly used for light metal processing tools, e.g. dies to cast aluminium, zinc, and magnesium, extrusion moulding, forging and moulding dies, mould parts, gears, plastic processing screws, ejectors, scissors knives for hot cutting, punches, extruders for non-ferrous metals, and moulds for plastics [53].

3.2 Laser cladding of H13 tool steel

Dies, moulds, and gears show a variety of damage during their life cycle such as cracks, scratches, broken edges, dents, digging, thermal cracking, plastic deformation, surface irregularities, worn-out geometries, dimensional changes, surface damage, etc. Damage to dies due to poor design, manufacture or incorrect operation will result in a short service life. On the other hand, cracks, scratches and broken edges appear at a later stage and are caused by elastic-plastic deformation, shape distortion, frictional wear, and the combined effect of distortion and wear [58]. For example, dies suffer great damage mainly through surface cracking due to wear and thermo-dynamic stresses during their lifetime [5].

Damage to dies, moulds, and gears leads to a loss of accuracy, size, or shape, which results in poor accuracy and geometry and inaccurate product dimensions. Tool steel is an expensive material that is difficult to machine. Therefore, various methods have been developed for its repair to reduce costs and downtime. The repair process typically begins with removing the damaged volume by one of the machining methods. Then the missing volume is filled through a suitable deposition process using an appropriate filler material. Conventional repair methods are based on an arc discharge [58]. However, with the development of high-power lasers, arc discharge has been increasingly replaced by laser cladding. Another approach is to manufacture dies with conformal cooling using additive manufacturing [6]. The great benefit of laser cladding in this field is its high productivity and precision, along with its minimal impact on surrounding material from thermal stress [4]. The cladding process is highly controlled and repeatable, as a robotic arm is usually used.

3.2.1 Processing parameters of laser cladding

The dependence of the geometry, microstructure, and hardness of a single bead of H13 tool steel on laser processing parameters such as power, scanning velocity, spot size, and powder feed rate was investigated in a paper [59]. It was shown that these parameters strongly affect the height, width, and penetration depth of the resulting clad. The volume of cladded material decreases as scanning velocity increases and powder mass flow rate decreases. The best cladding efficiency (measured as the ratio of powder mass deposited to powder mass blown) was found to be approximately 18%, while the worst efficiency was less than 7%. The microstructure refinement, observed using an optical microscope,

depends on the scanning velocity and the laser spot size. Furthermore, a significant change in the hardness of the newly formed material was observed, ranging from 500 to 800 HV. The authors suggest that this property could be used in repairs, when the resulting hardness of the newly formed surface would be selected based on the given requirements. Based on their conclusion, the repaired product surface would not need further heat treatment, which would lead to additional financial savings [59].

When cladding, one bead is usually not enough, so it is important to study the effect of overlapping tracks and layers. The paper [60] describes a comprehensive three-dimensional numerical model for the double-track laser cladding process of H13 tool steel. The research examines the influence of individual beads, which interact with each other during cladding. It was shown that the maximum temperature for the second bead is reached below the surface of the resulting deposit, not at the surface. This phenomenon needs to be taken into account, as the maximum reached temperature and the cooling rate affect the mechanical properties of the material, as described above. However, the effect of more than two layers on the temperature profile was not described [60].

3.2.2 Microstructure and real structure

The microstructure of one cladded H13 tool steel layer was investigated in [5], where martensite and retained austenite were observed in the clad metal itself. SEM images revealed carbides, probably M_7C_3, where M is different alloying elements between martensitic laths. No retained austenite or carbides were observed by XRD in the same paper. Conversely, based on EBSD analysis, it was found that the clad contains retained austenite, Mo_2C carbides, up to 23 vol. % of $Cr_{23}C_6$ and Cr_7C_3 carbides, and 26 vol. % of VC carbides, see Figure 18. When converted to weight percentages, this corresponds to 20.5 wt. % for $Cr_{23}C_6$ and Cr_7C_3 carbides and 19 wt. % for VC. Although only a small area of the clad was analysed using the EBSD method, this result does not agree with the weight representation of each alloying elements in the used steel, see Table 1, when according to the standard there is only 5 wt. % of Cr in the steel. Also in [61], more than 36 vol. % of carbides were described in one cladded bead using EBSD, which again does not correspond to the chemical composition. In contrast, the authors of the paper describing the surfacing of a chemically similar compound CPM 9V [62], which is used to repair dies and moulds made of H13 steel, were able to index only ferrite and retained austenite.

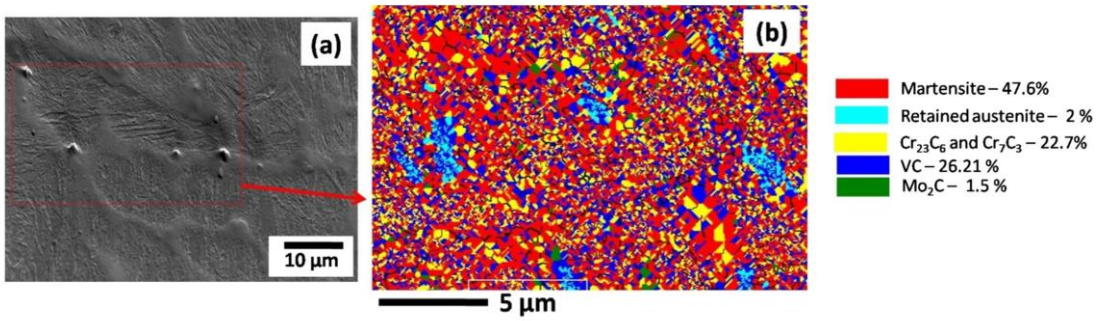

Figure 18: (a) SEM image of laser-cladded AISI H13 tool steel, (b) corresponding phase map obtained by OIM [5].

The effect of annealing has been investigated in a publication [63]. Here it was shown that carbon precipitates from the martensitic matrix and reacts with other elements forming alloy carbides (Mo_2C, VC, Cr_7C_3 and $Cr_{23}C_6$) at the tempering temperature from 550 to 650°C. Further, the matrix of martensite becomes softer due to the decline in the dislocation density and the redistribution of residual stresses. It was shown that hardness also sharply decreased [63].

As X-ray phase analysis cannot distinguish between ferrite, bainite or martensite in low carbon steels, only the major α-Fe phase and retained austenite were observed on as-deposited clads [64]. The paper [64] even states that the proportion of austenite was up to 20% by volume. However, the work [5] concludes that the one-layer clad does not contain retained austenite. It was further reported that the annealing decomposes the retained austenite, as described in Figure 17 [63]. Carbides were not observed using XRD probably due to their small proportion [5] [64]. Samples prepared by the SLM method did not contain carbides either [65]. However, fine carbides between martensite laths can be seen on a transmission electron microscope [63].

Other parameters of the real structure of single cladded bead that can be obtained by XRD, such as crystallite size and microdeformation, were studied in [66]. Here it was shown that the crystallite size of laser-cladded steel is 30% smaller and, conversely, the microdeformation is 30% larger compared to conventionally cast and tempered alloys. As expected, crystallite size increased slightly after annealing at 550°C for two hours and microdeformation decreased. However, there is no more detailed description in the literature of the real structure of the cladded material for one bead or multiple layers.

3.2.3 Residual stresses

The state of residual stress of laser-cladded H13 tool steel has been described in several publications. One paper [66] identified compressive residual stresses on the surface of the cladded bead. However, the direction in which the values were obtained is not precisely defined. Further, in different research [64], tensile residual stresses of about 150 MPa in the direction parallel to the cladding and 120 MPa in the perpendicular direction were observed in as-cladded H13 steel. In [67], authors also reported tensile residual stress in H13 laser clads on AISI 4150 low alloy steel substrate without pre-heating. When the substrate was pre-heated to 500°C, compressive residual stress was observed. When a chemically similar material CPM 9V was cladded, the compressive stresses were described in the cladding direction [68]. The values of residual stresses are opposite in different papers and there is no more detailed description in the literature of the residual stresses of the cladded material along one bead.

The depth profile of residual stresses on a single bead clad was investigated in the paper [69], when a chemically similar material CPM 9V was cladded on H13 steel. In the direction along the cladding, compressive residual stresses were found on the surface, while tensile stresses were found at the interface with the substrate. Other results directly regarding the material H13 are not reported in the literature.

A larger cladded volume was studied in publication [70] using neutron diffraction. Compressive residual stresses on the surface were found up to a depth of approximately 4 mm, see Figure 19. On the contrary, tensile residual stresses were observed at a greater depth, this area also showed a lower hardness of 200 HV. It was stated that the compressive stress states in the top layer are favourable in terms of fatigue life. However, the article does not indicate the direction of the residual stresses [70]. A similar depth was described by a numerical simulation using the finite element method, in which a two-layer clad was simulated. Compressive residual stresses were also experimentally confirmed in the clad itself in the direction perpendicular to the beads, while in the substrate there were tensile residual stresses [71]. However, tensile residual stresses in the surface layer were describe as well when cladding chemically similar material CPM 10V [72].

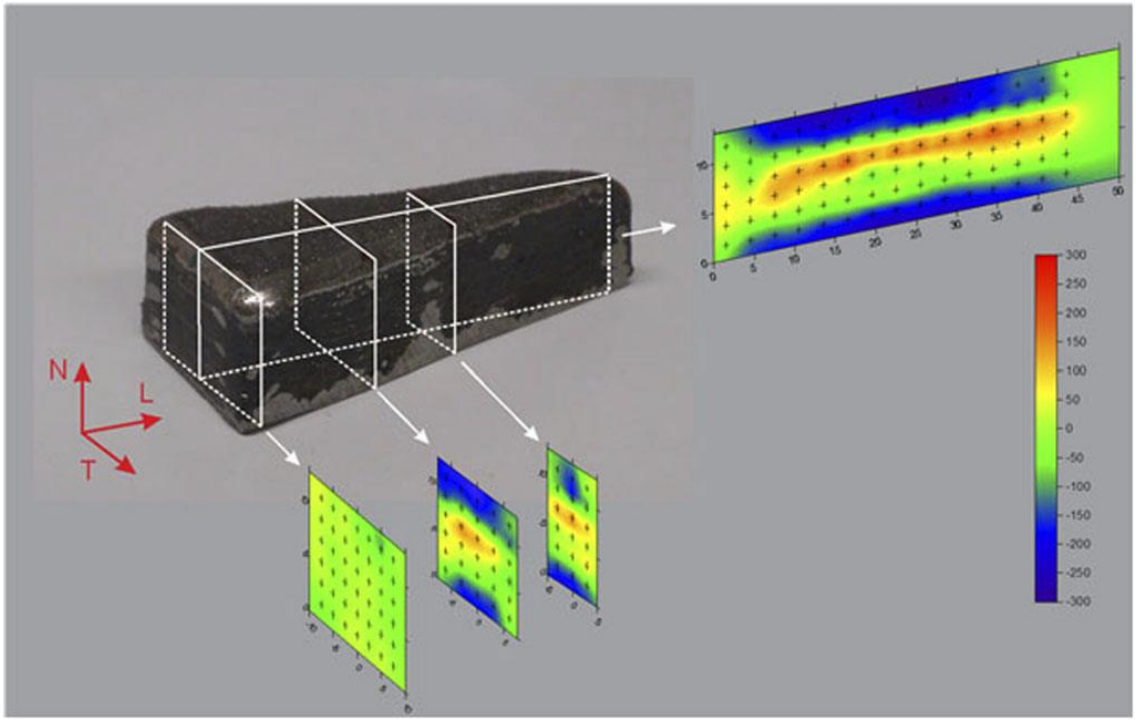

Figure 19: Residual stresses in MPa in four different cross-sections of a laser-cladded wedge [70].

The paper [73] that experimentally investigated and modelled the laser cladding of H13 steel using wire instead of powder states that the maximum residual stresses lie in the junction of the clad and substrate. The von Misses stress was approximately 1270 MPa which is slightly smaller than the yield stress (1280 MPa for 45 HRC). The von Misses stress is a scalar value that can be computed from the stress tensor and predict yielding of materials under complex loading. Therefore, it was shown that the most dangerous location after deposition is the junction of the cladded volume and substrate when cladding larger volumes because of the high residual stresses [73].

3.2.4 Mechanical properties and hardness

The cladded material showed a higher yield strength and a higher tensile strength of up to 300 MPa in comparison with conventionally cast and tempered material. Further, it was found that the yield strength and tensile strength do not depend on the orientation of beads, see Figure 20. Only the sample loaded perpendicular to the cladding direction showed an elongation of 2% at fracture, which is less than half of the sample oriented in the cladding direction. By annealing the clad at 550°C, the yield and tensile strength were

slightly reduced, but at the same time the ductility was increased to values comparable to conventionally processed material [5].

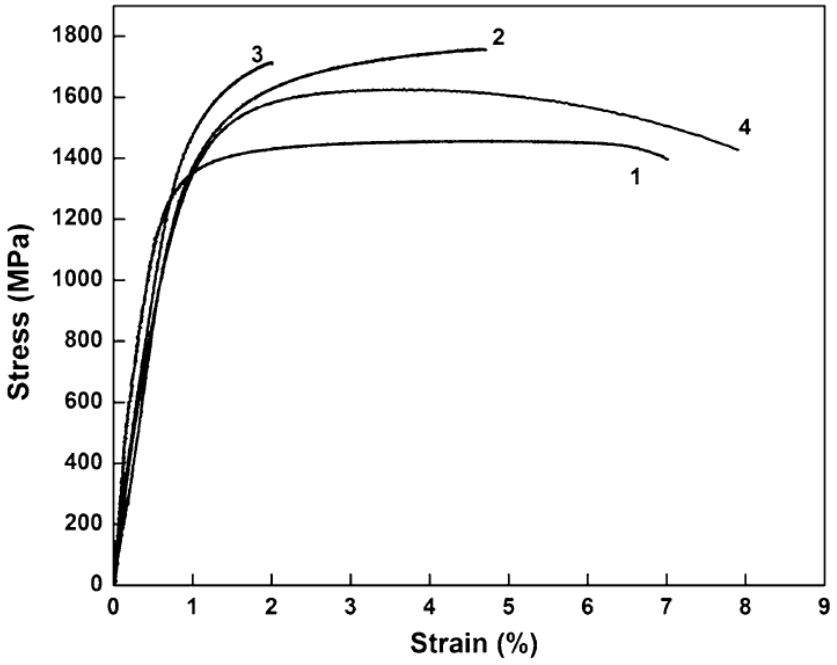

Figure 20: Stress–strain curves for (1) conventionally processed material, (2) laser-cladded sample loaded perpendicular to the cladding, (3) sample loaded parallel to the cladding, and (4) sample loaded perpendicular to cladding followed by tempering at 550°C [5].

Paper [66] describes the depth hardness profile of one cladded bead with optimized parameters. The cladded material had a hardness of 700 HV. The effect of annealing was also investigated, when after two hours at 550°C there was a decrease in hardness by approximately 100 HV. The authors of paper [74] also showed similar results. On the contrary, there was no significant change in hardness during annealing of one cladded layer, in both cases the hardness in the middle of the layer was approximately 600 HV [5].

Other research describes a depth hardness profile in which structural steel was used as a substrate. The heat-affected zone in the annealed substrate just beneath the interface was described. Above the interface, the dilution layer showed slightly lower hardness than the rest of the clad. Furthermore, hardness varying from 560–590 HV0.05 was determined in the cladded volume because the microstructure was heterogeneous [64].

The mechanical properties of a larger volume cladded from many layers were described in research [63]. The as-cladded material exhibited a lath martensite structure with very fine carbides and a hardness of about 570 HV_{IT}. This suggests that when cladding larger volumes, the previous layers are annealed or the cooling is slower, see Figure 16. This can significantly change their microstructure and mechanical properties [75]. Further, heat treatment induced the phase transformation of martensite into tempered martensite with the precipitation of carbides. The hardness shows a slight increase and finally a sharp decrease as tempering temperature increases, with a maximum at 550°C, see Figure 21 [63]. Clad hardness was therefore seen to copy Figure 17, i.e. reaching a maximum hardness after annealing at a temperature of 550°C. Lower hardness values rise close to the surface, at greater depths the values are stable. After annealing, a lath structure of martensite and fine carbides averaging 5 to 15 nm in size precipitated, which caused higher hardness [63].

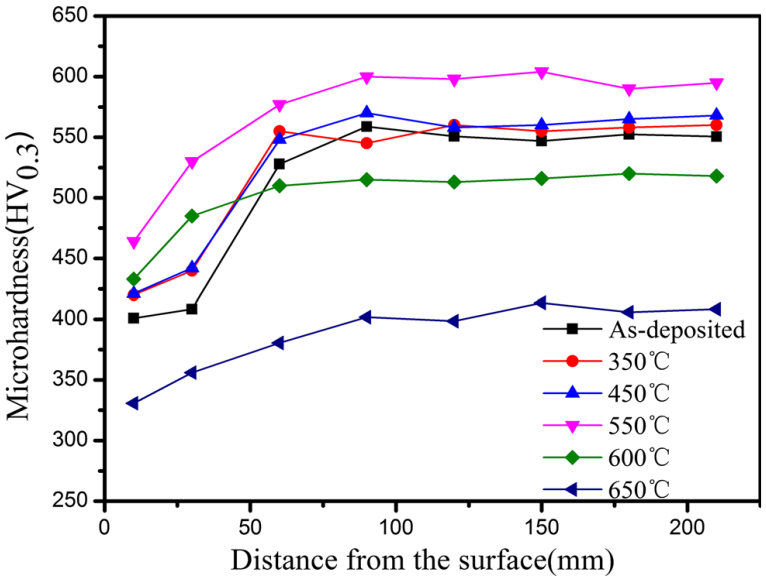

Figure 21: Hardness distribution of samples under different heat treatment [63].

3.2.5 Wear resistance

The authors of article [64] showed that the cladded volume indicates a smaller volume loss compared to conventionally manufactured steel in the classical pin on disk test, where Cr-steel balls with a hardness of around 63 HRC were used against flat H13 specimens. The wear mechanisms for as-cladded H13 steel were different, see Figure 22, which was attributed to the different microstructure, as the clad mainly consisted of martensite and

retained austenite. On the other hand, conventional H13 steel contains tempered martensite and hard dispersed carbides [64].

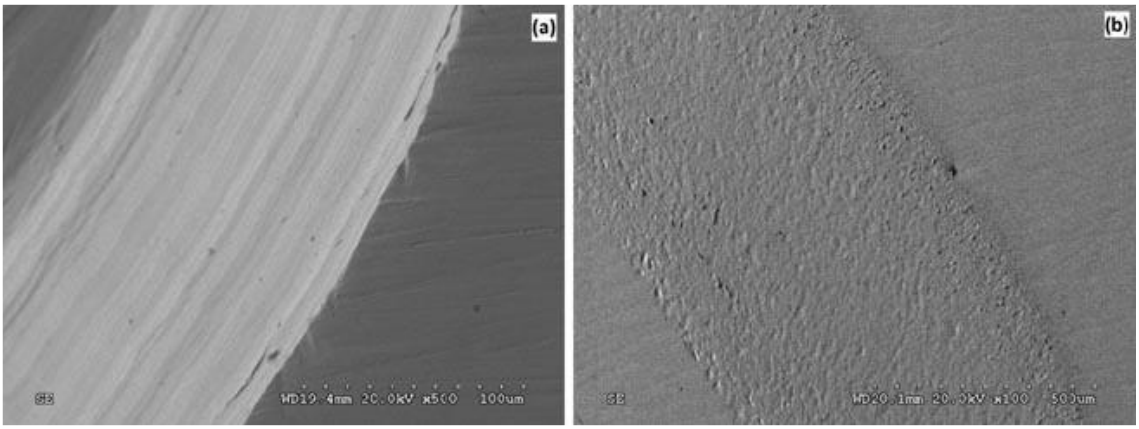

Figure 22: SEM micrographs showing the characteristic morphology of the worn tracks of (a) as-cladded, (b) conventionally manufactured H13 steel (54 HRC) [64].

The wear resistance of the clad was also investigated in paper [5], where an analogy of a pin on disk test was used. A WC ball (with a higher hardness than the clad) was used as a pin, which moved on the surface of the cladded material along a linear path. It was shown that the specific wear rate for as-cladded samples and tempered samples at 550°C is lower than for conventionally hardened and tempered H13 tool steel [5]. The difference is probably caused by the higher hardness of the clads (greater by 200 HV).

In a different study, clads annealed at a temperature of 600°C and higher with lower hardness compared to a non-annealed sample showed higher wear resistance in the pin on disk test at elevated temperature, probably due to the thicker surface oxide layer [63].

3.2.6 Application

The possibilities of using H13 tool steel laser cladding for gear repair are described in paper [76] and Figure 23. The authors propose various cladding strategies, then describe the mechanical properties and choose the most advantageous procedure for repairing a broken gear tooth. Further, the research shows that a tensile sample partly repaired using the cladding process has a slightly lower yield strength in comparison with new ones.

However, the repaired tooth shows higher hardness and better wear resistance than the original, as a higher strength material was used for the repair [76].

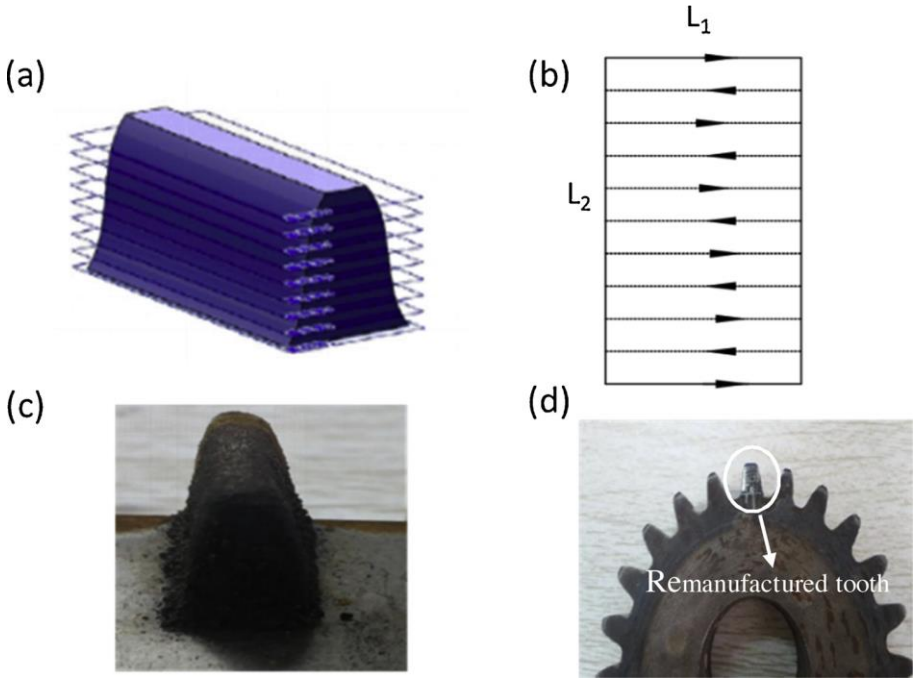

Figure 23: Broken gear repairing process: (a) model of the broken tooth, (b) the cladding strategy of the first layer, (c) remanufactured tooth, (d) gear after post-processing [76].

4 Goals of the doctoral thesis

This work aimed to contribute to a more detailed understanding of the effect of laser cladding on the real structure of AISI H13 tool steel, which is widely used in industry and was chosen as a representative sample. In the literature review, it was shown that results of phase composition obtained using X-ray diffraction and EBSD show irregularities. Further, there is no more detailed description in the literature of the real structure of the cladded material. The values of residual stresses are opposite in different papers and there is not more detailed description of the residual stresses of the cladded material along one bead. Therefore, the goal of this research is, in contrast to the cited papers, to correlate the wide range of results mainly for multilayer cladding, which was prepared using uniform cladding parameters. No such comprehensive research can be found in the literature. Research also took into account the requirements of industry and pressure on efficiency and cost reduction, which will be the main motivation for the production deployment of this advanced technology [1].

For cladding, the goal is to create a new volume that will be at least comparable to the original material with respect to properties. Therefore, it is necessary to ensure an adequate bond with the substrate and the clad must not have any internal defects that could cause rapid degradation [77]. In the first step, one bead will be cladded and subjected to a detailed examination. The microstructure and the real structure will be characterized. As already outlined, residual stresses significantly affect the fatigue life of the component [78], so they will be given considerable attention. After hardening of the tool steels, tempering is required according to the material sheets. Therefore, in the second phase, it will be necessary to investigate the effect of annealing on the microstructure, residual stresses and hardness, and assess the need to perform this costly heat treatment. Based on these results, multi-layer cladding could continue.

The microstructure, real structure, residual stresses, and other mechanical properties are given not only by the cooling rate of the beads and the layers, but also by annealing the already deposited layers with additional cladded ones [63]. Annealing can greatly reduce the mechanical properties needed for a component to function properly. Therefore, in the next part, the cladding of several beads and layers will be examined. Additionally, in-situ tensile testing experiments using a scanning electron microscope can

reveal microstructural changes during deformation. All results obtained will be correlated with local hardness and wear measurements.

In addition, laser cladding does not achieve sufficient accuracy for the newly formed surface to serve without further surface machining [79]. It is necessary to carefully determine whether machining the part into the desired shape will bring areas with poorer mechanical properties to the surface. This would lead to a shorter service life and consequently make laser cladding unprofitable. This possibility has not been considered in the available literature, therefore it is necessary to research the state of the real structure and other mechanical properties on the machined surface.

The following text will try to address these questions and ultimately suggest further steps, as this is very complex scientific research. New findings and correlations of this thesis will find application not only in additional research, but also in the practical production and repair of moulds, dies and other tools made of tool steels.

5 Real structure of single-pass laser-cladded H13 tool steel

The first chapter of the experimental part describes single-pass laser cladding, while the second examines multilayer cladding. In the first case, laboratory samples prepared with an optimized technology were examined. This thesis does not intend to find the proper processing parameters of a given process but rather focuses on describing the effect of laser processing on engineering materials.

First a single bead was laser cladded and tested. The aim of this chapter is to describe the effects of laser processing on the microstructure and residual stresses of AISI H13 tool steel laser cladded on a classic S355 construction steel substrate, which we call as-cladded samples. Additionally, the effects of tempering were studied.

This chapter reports an investigation of residual stresses by X-ray diffraction and microstructure (chemical and phase composition, crystallite orientation), orientation imaging microscopy (OIM) using electron backscatter diffraction (EBSD), and energy-dispersive X-ray spectroscopy (EDS) with scanning electron microscopy of laser-cladded tool H13 steel. The research aims to understand the residual stresses and microstructural characteristics that are among the most important factors influencing product behaviour, especially fatigue life [80].

During laser cladding, rapid cooling could occur, leading to the formation of brittle martensitic microstructure [72]. Hence, it is important to observe the effect of tempering, which subsequently influences the properties of the newly created surface of the cladded volume. Therefore, the effects of tempering were described using instrumented indentation technique, OIM and X-ray diffraction to determine changes in real structure and residual stress.

5.1 Experiment

Laser cladding was carried out using a Laserline 5.5 kW diode laser with a Precitec Y52 optical head with coaxial feeder. Laser power with a density of 108 J/mm^2 (4.5 kW, 500 mm/min) was applied to form a single clad 137 mm long and 6 mm wide with a height of approx. 1 mm above a substrate made of S355 structural steel. AISI H13 tool steel powder was used with an average particle diameter of 53.1 ± 15.9 μm.

Three samples were taken from the clad with average dimensions of 15×12×5 mm^3 to describe the effect of tempering. The first sample from the clad was analysed without heat treatment. The second sample was annealed at 550°C for 2 hours and the third sample was heat treated twice at the same temperature for 2 hours.

5.1.1 Microstructure

Debye-Scherrer diffraction patterns of the {*211*} diffraction line of the α-Fe phase were taken using an ISO DEBYEFLEX 3003 diffractometer with an X-ray tube with a chromium anode, a 1 mm diameter cylindrical primary collimator, and the distance between the measured area on the sample surface and the flat detector was 50 mm.

In order to determine the phase composition of the surface layer, diffraction patterns were obtained by measuring the clad using an X'Pert PRO MPD in classical Bragg-Brentano (BB) focusing configuration with cobalt tube anode and 1×0.25 mm^2 pinholes, see Figure 24. Measured diffraction diagrams were processed using X'Pert HighScorePlus and crystallographic phases were identified using a PDF-2 database. Quantitative analysis was evaluated using Rietveld analysis in TOPAS 4.2 software. The effective depth of penetration (T^{eff}) corresponds to the thickness of the surface layer, which provides about 63 % of the diffracted intensity. In the case of the wavelength used, the T^{eff} is about 5 μm.

Figure 24: X´Pert PRO MPD diffractometer with four-axis positioning device and triangulation laser.

The OIM data was collected using a Philips XL 30 FEG and Lyra Tescan scanning electron microscope equipped with a TSL OIM system based on DigiView 3 and Hikari cameras, EDS EDAX SUTW+ and an EDAX Octane detector. An accelerating voltage of 25 kV and 15 kV and step size of 0.4 μm and 50 nm were used for scanning. A grain boundary is defined in the microstructure as a boundary between two neighbouring scanning points having crystallographic misorientation greater than 5°. All EBSD data were analysed with TSL OIM Analysis 7.3.0 software and only data points with a confidence index higher than 0.05 were used.

5.1.2 Residual Stress Analyses

X-ray diffraction analysis of residual stress (RS) was carried out using an X´Pert PRO MPD diffractometer, see Figure 24, with a chromium tube anode and pinholes determining the irradiated area of the primary beam measuring 1×0.5 mm^2 in the longitudinal (L) direction and 2×0.25 mm^2 in the transversal (T) direction, respectively. Diffraction angle $2\theta^{211}$ was taken as the centre of gravity of the {*211*} diffraction doublet *CrKα*. For residual stress evaluation, the $\sin^2\psi$ method and X-ray elastic constants $½s_2 = 5.76$ TPa^{-1} and $s_1 = -1.25$ TPa^{-1} were used. Full widths of the measured diffraction lines $CrK\alpha_1K\alpha_2$ at half of the maximum (FWHM) were also evaluated for both directions. To determine the depth profiles of macroscopic residual stress, the surface layers of the material [81] were electrolytically etched using a PROTO Electrolytic Polisher with electrolyte A. The etched area was defined by a mask of Ø 5 mm. The depth of the removed layer was measured using a micrometre gauge.

5.1.3 Hardness Tests

Hardness was measured by the instrumented indentation technique. Tests were carried out using a NHT2 nanoindentation instrument with diamond Berkovich indenter. The indentation cycle consisted of loading to a maximum force of 500 mN for 30 s, holding at maximum load for 30 s, and unloading again for 30 s. Data were evaluated using the Oliver-Pharr method [49] and the average values were computed from 3 indents for each depth under the surface of a clad. The error bar represents the standard deviation.

5.2 Results and discussion

5.2.1 As-cladded sample

Table 3 gives the range of the chemical composition of H13 steel determined and quoted by EN ISO 4957 [56], the next row shows average chemical composition and standard deviation obtained by EDS on a cross-section of four randomly selected particles of the powder used; the bottom row shows the average chemical composition and standard deviation in four different clad cross-section areas of dimensions approx. 500×250 μm^2. Table 3 shows that only chromium in the clad is on average about one weight percentage less than the standard prescribes. On the contrary, manganese was observed to be 0.1 % more, which is probably due to the substrate used (S355 structural steel contains up to 1.7 wt. % of manganese). The SEM image of the cross-section of the single clad with specified directions and an area of 200×200 μm^2 which was observed using OIM can be seen in Figure 25. Lack of fusion on the sides of the clad was observed, which probably resulted from the improper setting of laser power density.

Table 3: Chemical composition of AISI H13 steel according ISO 4957 [56], the AISI H13 powder used and the clad.

	Cr [wt. %]	Mo [wt. %]	Si [wt. %]	V [wt. %]	Mn [wt. %]	C [wt. %]
H13 1.2344	4.80–5.50	1.20–1.50	0.80–1.20	0.85–1.15	0.25–0.50	0.35–0.42
H13 Powder	5.10 ± 0.07	1.79 ± 0.08	0.92 ± 0.11	1.08 ± 0.02	0.45 ± 0.07	
Clad	3.77 ± 0.05	1.21 ± 0.05	0.72 ± 0.01	0.84 ± 0.03	0.62 ± 0.03	

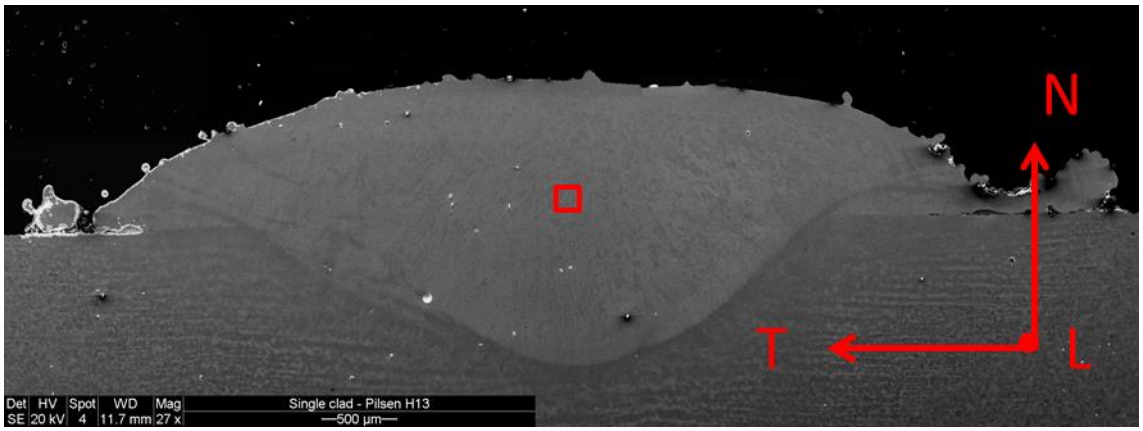

Figure 25: SEM image of the cross-section of the AISI H13 tool steel single clad with marked directions and area which was observed using OIM.

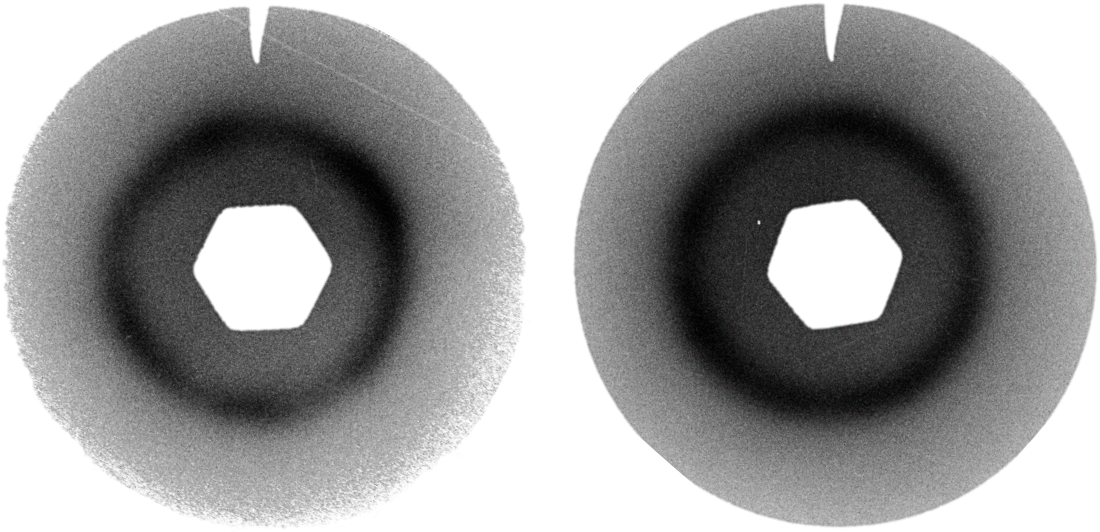

a) Surface b) 100 µm

Figure 26: Debye-Scherrer diffraction patterns of the {*211*} diffraction line of the α-Fe phase for the surface and after removing 100 µm, where the mark in the image points in the L direction.

Figure 26 shows two patterns recorded using the Debye-Scherrer method in the reflection arrangement, where some difference can be seen between the surface of the sample and after electrolytic etching of 100 µm. The diffraction pattern for the surface shows inhomogeneity of intensity around the circle, which indicates a slight texture, which is not so pronounced with depth. The line is wide on both patterns, indicating higher microdeformation and/or small crystallites. In general, it can be stated that the character of {*211*} α-Fe diffraction lines obtained from cladded material indicates that the {*211*} α-Fe planes are suitable for X-ray analysis of residual stress when a sufficiently

large irradiated volume is selected. In this case, the application of the $\sin^2\psi$ method is completely correct.

The comparison of surface RS obtained by XRD in direction L and T is plotted in Figure 27. RS at the beginning and the end of the clad are comparable with the experimental error. In the L direction, RS exhibit slight compressive stresses along the clad. However, in the T direction, tensile RS were obtained. This agrees with the literature ([66] and [68]), where compressive residual stresses were analysed in the cladding direction when cladding a chemically similar material, CPM 9V.

According to the linear equation developed by Andrews [82], M_s temperature is 316°C for the lower limit of alloying elements and 268°C for upper limit of alloying elements [83]. So if we assume that the coefficient of thermal expansion for H13 steel is 12.5×10^{-6} K^{-1}, relative shrinkage of 0.0034 results from cooling from the average M_s to room temperature [84]. On the other hand, the volume changes during phase transformation in steels are a function of carbon content. Dimensional change during transformation from spheroidite to martensitic microstructure is 0.0026×(wt. % of C) [83]. For H13 steel, the dimensional change is therefore between 0.0020 and 0.0024. Shrinkage and expansion are therefore the same order of magnitude and depend on the specific situation that prevails. Consequently, the particular situation dictates which effect will be dominant. In this case, the transformation stresses in the L direction appear to prevail as compressive residual stresses have been observed in this direction.

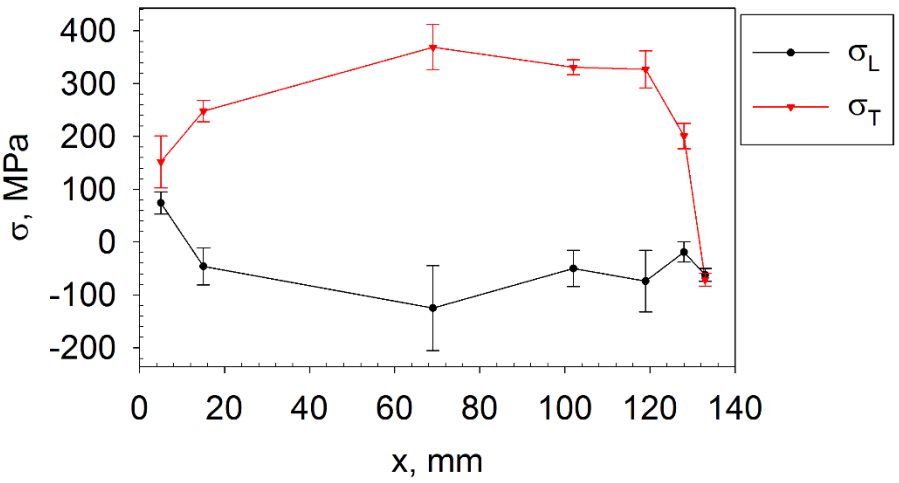

Figure 27: Surface RS on the top of the clad in direction L and T along the length of the laser track, where x is the distance from the beginning of the clad.

The depth profiles of macroscopic residual stresses were acquired at the end of the clad for x = 115 mm, see Figure 28. The values were obtained by gradual electrolytic etching and analysis of the new surface in two directions. It can be seen from the figure that the tensile RS in the T direction decreases rapidly and at a depth of about 150 μm, RS is compressive. This is followed by an area with slightly tensile values and at a depth of more than 500 μm there is only compressive RS. In the L direction, there is compressive residual stress throughout the entire analysed depth. This state of residual stress is convenient because after removing the top layer of material, on the surface there will be areas with suitable compressive stress that improves mechanical properties.

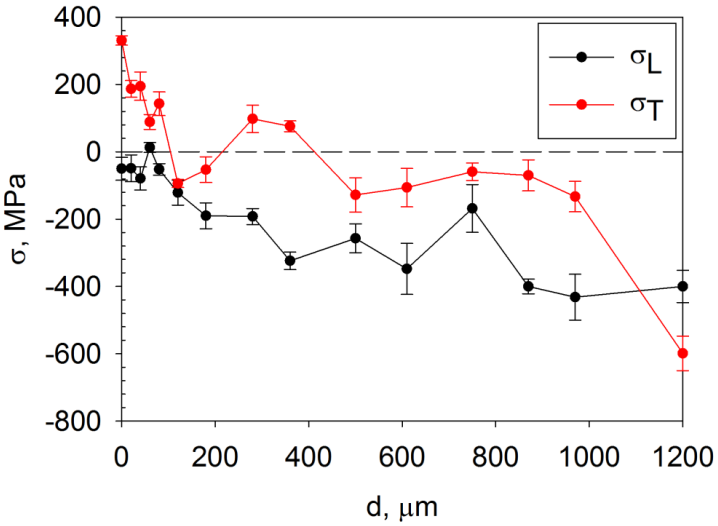

Figure 28: Depth profile of the macroscopic residual stresses in direction L and T at a place x = 115 mm, where d is the depth from the surface.

Mass weight content of γ-Fe in the surface layer depending on the distance from the beginning of the clad is plotted in Figure 29. It can be seen that at the beginning of the clad, γ-Fe content increases to around 4 %, and in the end no retained austenite was observed by XRD. This could be due to a slower cooling rate at the end as the heating of the substrate occurred. After obtaining these results, the real structure and the microstructure of the single clad was further evaluated by OIM on a 5 mm cross-section from the beginning of the clad.

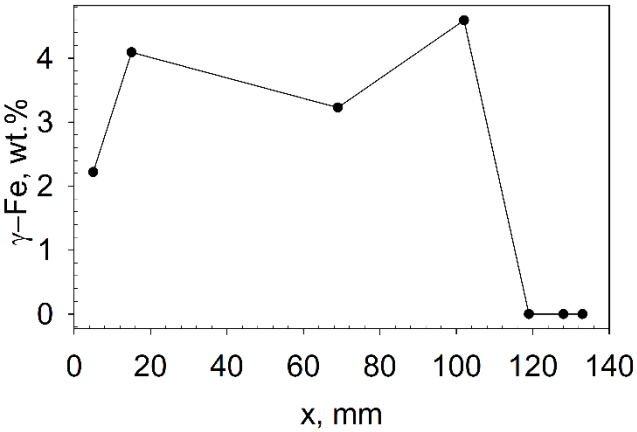

Figure 29: Mass weight content of γ-Fe in the surface layer obtained by XRD.

The main phase detected in the clad was body-centred cubic iron. Figure 30 shows inverse pole figure (IPF) maps of α-Fe in the selected area, wherein individual colours correspond to the normal vectors of crystallographic planes that are parallel to the given sample direction. The original austenite grains with a characteristic size of 20-50 μm, which were established during the transition of the melt into a solid phase and which were subsequently transformed into martensitic or bainitic laths, are clearly seen in the figure. It has to be noted that the EBSD technique is not able to directly distinguish ferrite and martensite. Carbides of alloying elements were not observed using EBSD. However, in the analysed area, 1.1 % of retained austenite was confirmed. The discrepancy with the XRD value could be due to the errors of each method and the larger volumes analysed by XRD, especially along the clad. At the beginning of the clad, the proportion of retained austenite seen in XRD increases. Another reason may be that XRD was performed on a cladding surface where the retained austenite content may vary.

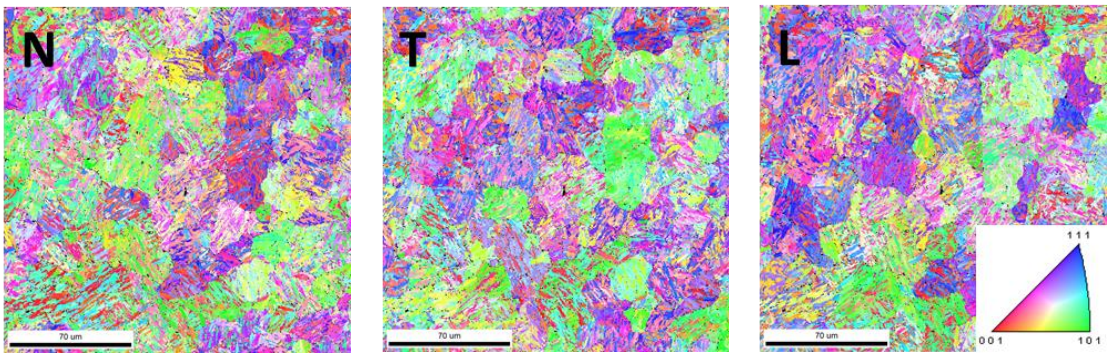

Figure 30: IPF maps of α-Fe for different directions in the selected area.

Figure 31 gives an idea of the relative distribution of individual alloying elements in the selected area obtained by energy-dispersive X-ray spectroscopy mapping. Darker colours indicate higher concentration of the element.

Figure 32 shows the relative distribution of chromium, where an EDS map of the entire clad was obtained. In this image, a lighter blue indicates a higher concentration of chromium. Since structural steel without added chromium was used as the substrate, the mixing of the material is clearly visible. A Marangoni flow was formed, which arises due to varying surface temperature across the melt pool surface, which causes fluid surface tension gradients and induced surface fluid flow from areas of low to high surface tension [85]. Strong mixing is undesirable as it leads to a reduction in the proportion of alloying elements when cladding different materials.

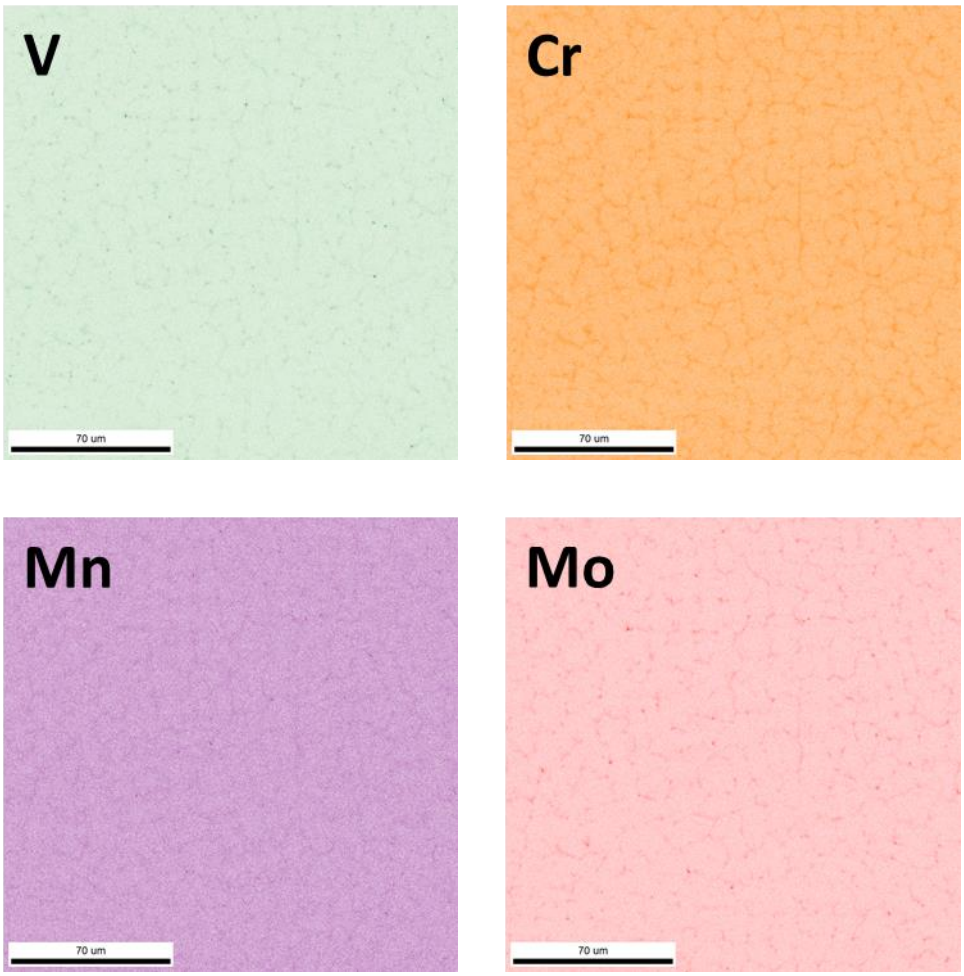

Figure 31: Relative representation of alloying element content in the selected area acquired by EDS.

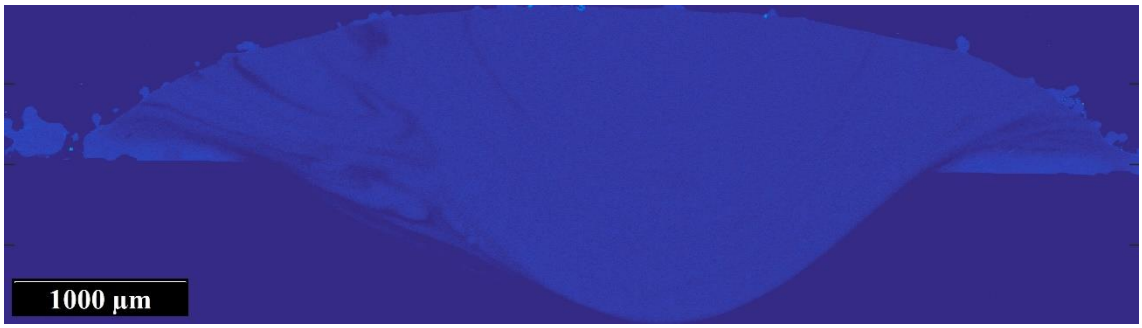

Figure 32: Relative representation of chromium content acquired by EDS.

Subsequently, the distribution of the misorientation angle in the selected area is plotted in Figure 33. Paper [86] showed that misorientation angles between the variants that satisfy the Kurdjumov-Sachs orientation relationship of phase transformation from face-centred cubic phase to body-centred cubic phase are up to 21.06° and then higher than 47.11°.

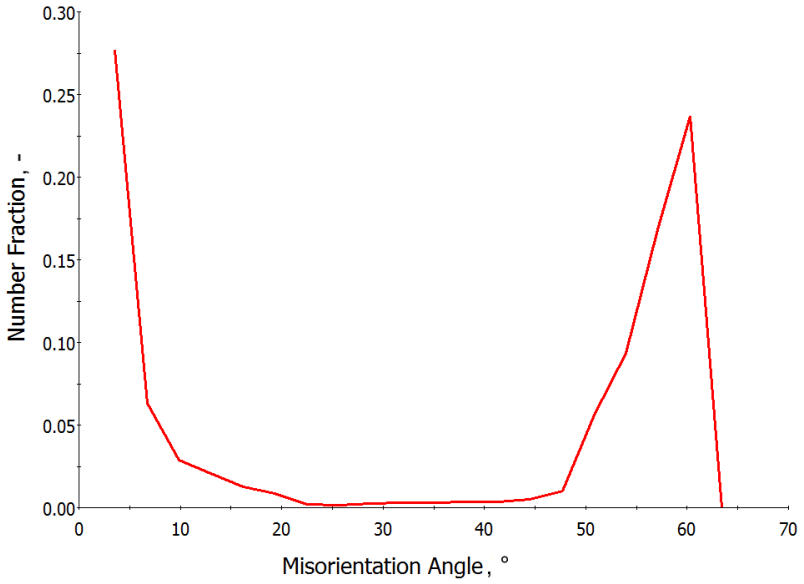

Figure 33: Misorientation angle distribution in the selected area.

Figure 34 compares the map of relative representation of chromium content and the IPF map with highlighted grain boundaries between 21.06° and 47.11°. It can therefore be clearly seen that a higher concentration of chromium corresponds with the random grain boundaries between 21.06° and 47.11°. These boundaries relate to the grain boundaries of the original austenitic grains which were formed during cooling of the melt. The unequal concentration of alloying elements is caused by the lever rule during

solidification. This could induce inferior mechanical properties of the steel as carbides of alloying elements were not observed.

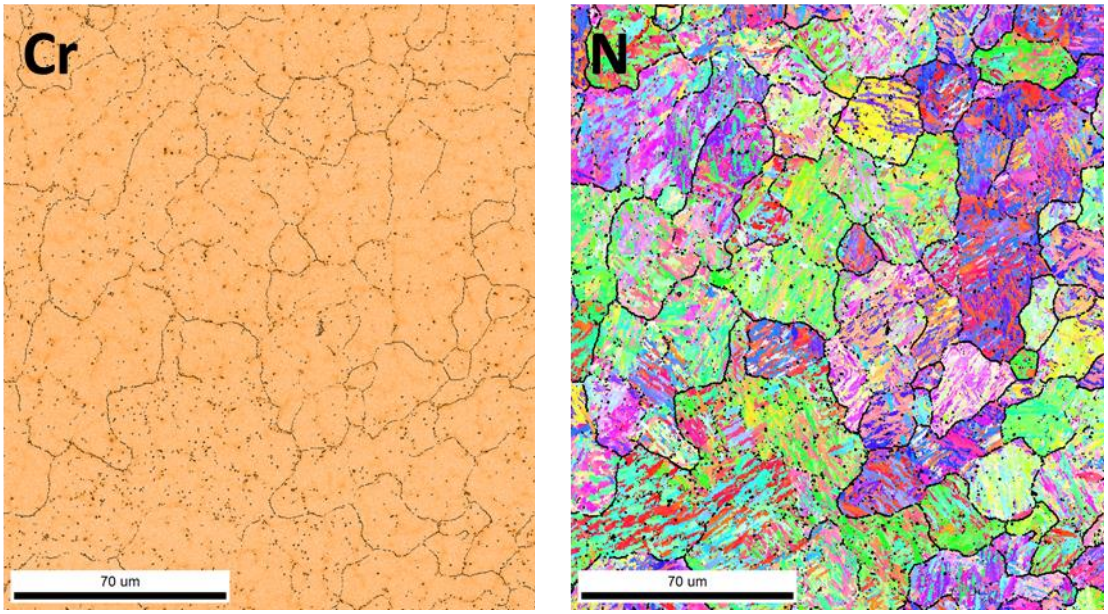

Figure 34: Comparison of the map of relative representation of chromium content and the IPF map with highlighted grain boundaries between 21.06° and 47.11°.

5.2.2 Effect of tempering

Three samples were compared to describe the effect of tempering, one as-cladded, the second was annealed once, the third twice. Results of surface RS and FWHM are compared in Figure 35. The FWHM is the average value obtained from both directions with the standard deviation as the margin of error. After cutting the clad, the tensile residual stress in both directions was analysed on the surface.

After the first annealing a noticeable decrease in RS and FWHM was observed. In addition, mild compressive RS was detected in the L direction (along the clad). After the second annealing there was a slight increase in RS and, above all, a significant reduction in the error. The FWHM dropped slightly. This effect is due to a lower density of dislocation and a decrease in macrostrain caused by annealing.

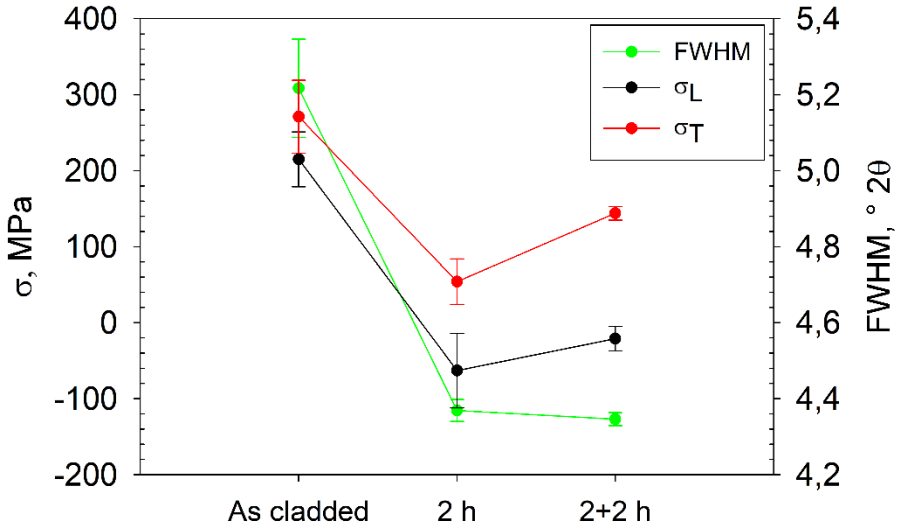

Figure 35: Surface RS and FWHM of the clad depending on tempering.

Depth gradient of hardness is shown in Figure 36. Parameter d represents the distance from the surface of the clad. It can be seen from the figure that the as-cladded sample exhibits a higher hardness of approximately 50 HV_{IT}. In addition, a slower drop in hardness towards the bulk values compared to annealed samples may be observed. However, there is no difference in hardness between the annealed samples.

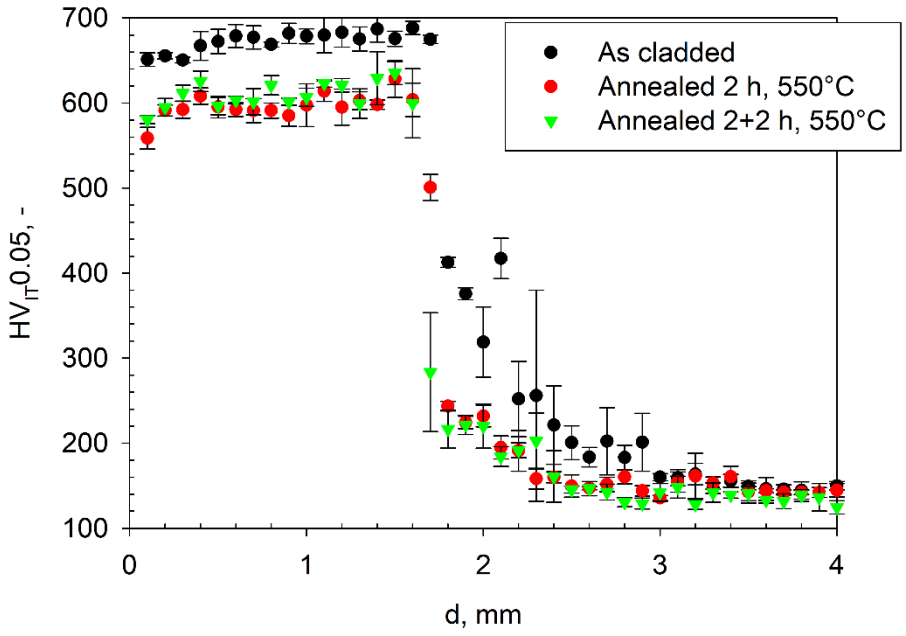

Figure 36: Depth gradient of hardness, where x is distance from the surface of the clad.

Figure 37 graphically illustrates the effect of annealing on the microstructure of the clad. An area 20×20 μm^2 in the middle of the cross-section of the clad was observed using OIM. Three differently annealed samples were used, so the measured area was not the same. As shown also in Figure 38, it can be stated that the annealing time increases the proportion of carbides and decreases the austenite fraction. This effect is well known and not surprising when diffusion is facilitated by higher temperature. However, the weight percentage of the carbides that were indexed during the measurement (see Figure 38) is inconsistent with Table 3. Carbides have been indexed three times more than the steel composition obtained by EDS analysis. It is difficult to distinguish between phases with the same crystal lattice using EBSD. Therefore, carbides were indexed with a low confidence index.

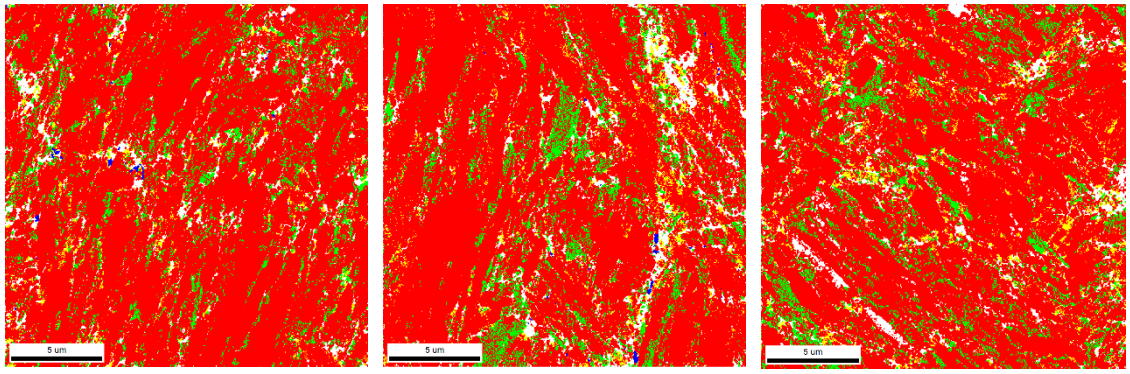

Figure 37: Effect of annealing on the phase composition of the clad where ferrite is red, $Cr_{23}C_6$ green, VC yellow and austenite blue (left as-cladded, middle after 550°C annealing for 2 h, right after 550°C annealing for 2+2 h).

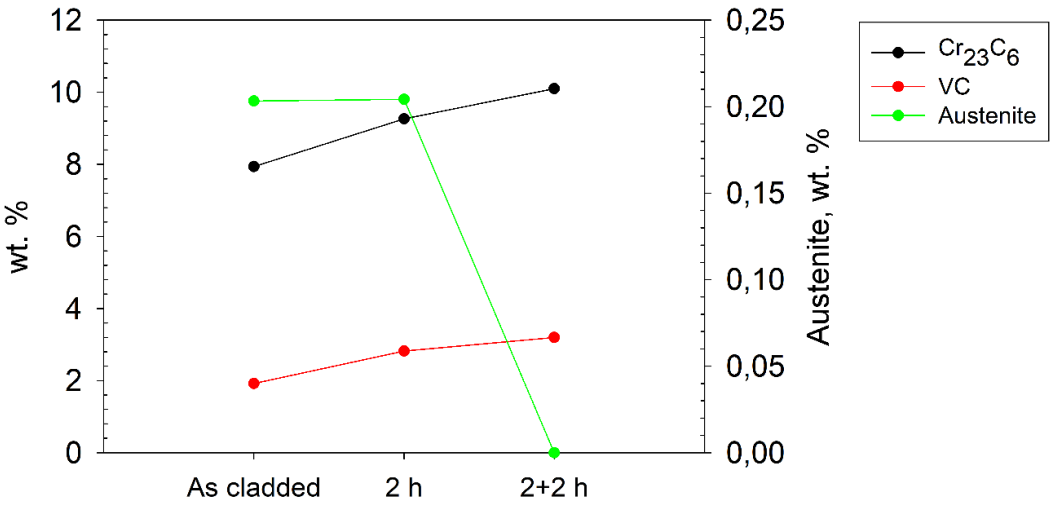

Figure 38: Effect of annealing on the phase content of the clad.

Inverse pole figures of ferrite in the selected area before and after annealing are shown in Figure 39, where [001] denotes direction L. The martensitic structure could be observed in all samples. However, a slight rounding of the corners of martensitic laths can be found after annealing for 2+2 hours.

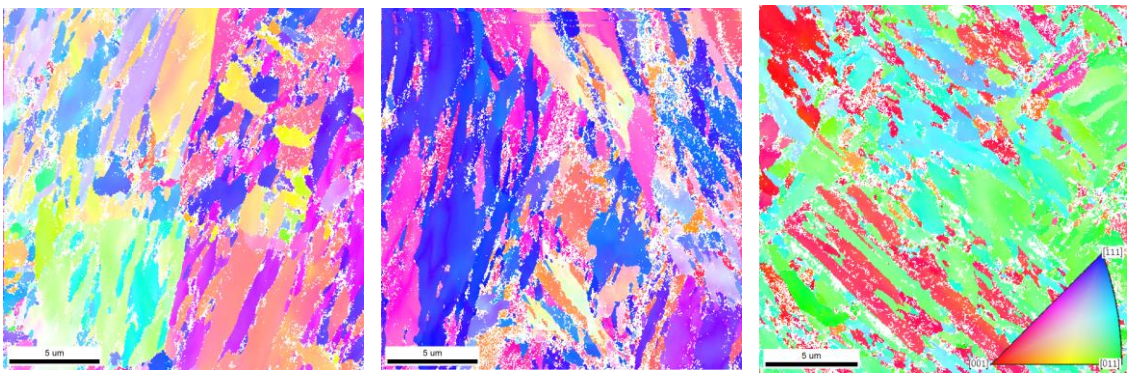

Figure 39: [001] IPF maps of the ferrite (left as-cladded, middle after 550°C annealing for 2 h, right after 550°C annealing for 2+2 h).

5.3 Conclusion

Laser deposition of H13 tool steel showed great application potential. Martensitic structure dominates in the single clad. This suggests high cooling rates and quenching of the clad. Further, no carbides and half the retained austenite compared with XRD were observed using EBSD. Laser deposition of H13 induced significant residual stress. Differences in residual stress at the beginning and end of the track are statistically insignificant within the margin of error. In the longitudinal direction, RS exhibits a slight compressive character along the clad. However, in the transversal direction tensile RS was detected. It may be concluded that in this case of laser cladding, phase transformation and not shrinkage is likely to be the dominant effect on the formation of residual stress in the L direction along the clad. This caused tensile RS in the perpendicular T direction. Analysed depths were mainly found to have compressive residual stress, which is convenient. In future research it will be necessary to describe the influence of cladding subsequent beads and layers.

Residual stress declined after tempering, which could have a beneficial effect on component service life, as compressive stress delays crack initialization and also slows its propagation [80]. The difference between phase composition detected by EDS and EBSD has not yet been accurately explained, so further measurements of the indexing parameters will be needed. Although it is possible that carbides cannot be reliably

distinguished by EBSD. Nevertheless, based on these results, tempering does not seem to be needed after cladding.

6 Real structure of laser-cladded H13 tool steel in multilayers

In the next step of the research, a larger volume of H13 tool steel was cladded and the impact of overlapping beads was investigated. Real structure and other mechanical properties are given not only by the cooling rate of the beads and the layers, but also by annealing the already deposited layers with additional cladded ones. Therefore, the research in this chapter is focused on this issue.

Further, due to the formation of brittle martensitic or bainitic microstructure [72], it is important to study material properties of the cladded material and the effect of tensile strain on the microstructure, which subsequently influences the properties of the newly created die parts. In-situ tensile testing experiments were performed to observe microstructural changes during deformation of laser-cladded samples. A scanning electron microscope with a tensile stage was used and the microstructure changes were monitored using orientation imaging microscopy (OIM) based on electron backscatter diffraction (EBSD). Results were compared with local hardness measurements.

As the hardness of the cladded volume can strongly affect the wear resistance, these results were also compared with each other.

Since H13 tool steel cladding will mainly be used to repair dies, moulds, and others, H11 tool steel was chosen as a substrate for further research. H11 tool steel according to the ASTM A681 standard (grade 1.2343 or X37CrMoV5-1 according to EU standard EN ISO 4957, 19 552 according to ČSN, or grade SKD6 according to Japanese standard JIS G4404) is also a Cr-Mo-V alloy steel. A comparison of the chemical composition of AISI H11 and H13 steel according to the relevant standard is given in Table 4. H11 steel is less alloyed compared to H13, the biggest difference is in the vanadium content. Compared to H13 steel, H11 steel achieves lower tensile strength and hardness at elevated temperatures.

Table 4: Chemical composition of AISI H11 and H13 steel according to ISO 4957 [56].

	Cr [wt. %]	Mo [wt. %]	Si [wt. %]	V [wt. %]	Mn [wt. %]	C [wt. %]
H11 1.2343	4.80–5.50	**1.10**–1.50	0.80–1.20	**0.30**–**0.50**	0.25–0.50	**0.33**–**0.41**
H13 1.2344	4.80–5.50	1.20–1.50	0.80–1.20	0.85–1.15	0.25–0.50	0.35–0.42

6.1 Adjusting cladding parameters

According to EDS chemical analysis, the substrate used for cladding meets the chemical composition requirements, only the manganese content is at the upper limit, see Table 5. The substrate was soft annealed with a hardness of 238 $HV_{IT}0.05$. Different powder was used for further cladding, therefore average chemical composition and standard deviation on a cross-section of four randomly selected particles is given in Table 5. The average particle diameter of the powder used was 94 ± 24 μm.

Table 5: Chemical composition of H11 substrate and H13 powder.

	Cr [wt. %]	Mo [wt. %]	Si [wt. %]	V [wt. %]	Mn [wt. %]	C [wt. %]
Substrate	5.14 ± 0.02	1.21 ± 0.03	0.91 ± 0.01	0.49 ± 0.01	**0.53** ± 0.02	
H13 Powder	5.34 ± 0.02	1.33 ± 0.04	1.05 ± 0.01	1.10 ± 0.02	**0.60** ± 0.02	

Since a different laser (IPG 3 kW Yt:YAG fibre laser) was used to prepare additional samples, the processing parameters had to be adjusted, see Figure 40. The original speed of 500 mm/min proved to be high, as the newly used laser had less power. The optimal cladding speed turned out to be 300 mm/min with an output of 2 kW, which corresponds to a laser power density of 90 J/mm^2. The diameter of the laser beam was 4.5 mm. The cladding build-up rate was 5.2 g/min. Argon was used as the transport and shielding gas.

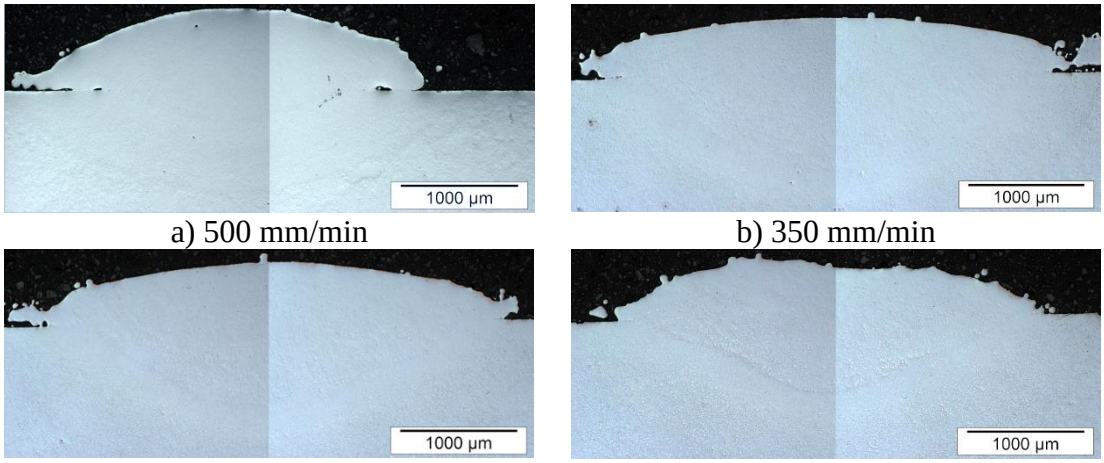

a) 500 mm/min b) 350 mm/min

c) 300 mm/min d) 250 mm/min

Figure 40: Optical image of the cross-section of the AISI H13 tool steel single clads with different cladding speeds.

The single clad cross-section in Figure 40 c) shows that material has been sufficiently mixed with the base material and the deposit does not show any defects, especially pores. There are no large areas lacking fusion on the edges of the clad that could act as notches.

Based on these results, multilayers, which are necessary to form larger volumes, were cladded with the same parameters. Five-layer samples were formed from six and seven overlapping beads on a substrate made from AISI H11 tool steel. The axes of the beads in one layer were 2 mm apart and the next layer was placed at the intermediate positions of the previous layer, see Figure 41. The cladding began in the upper left corner and continued to the right. This type of clad was selected for most analyses, which aimed to describe the effect of laser cladding on the real structure.

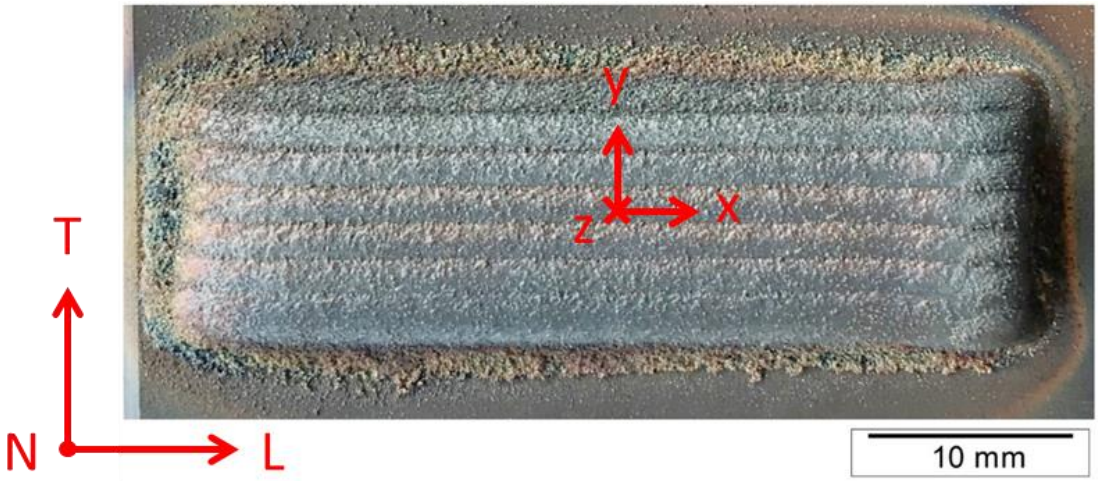

Figure 41: Laser-cladded sample of AISI H13 tool steel with five layers (top view) with directions marked by N(z), L(x) and T(y) for normal, longitudinal and transverse.

Figure 42 is an overview image of the clad, where the beads from which the volume is formed are clearly visible. The microstructure was revealed using nital (5% nitric acid). It can be seen on the cross-section that there has been sufficient mixing with the substrate and under the remelted material there is a heat-affected zone of the base material. The volume shows no macroscopic internal defects, which are undesirable. Only on the sides, a thin layer was formed which is not sufficiently bonded to the substrate. Further, the figure defines the directions and the analysed area using OIM.

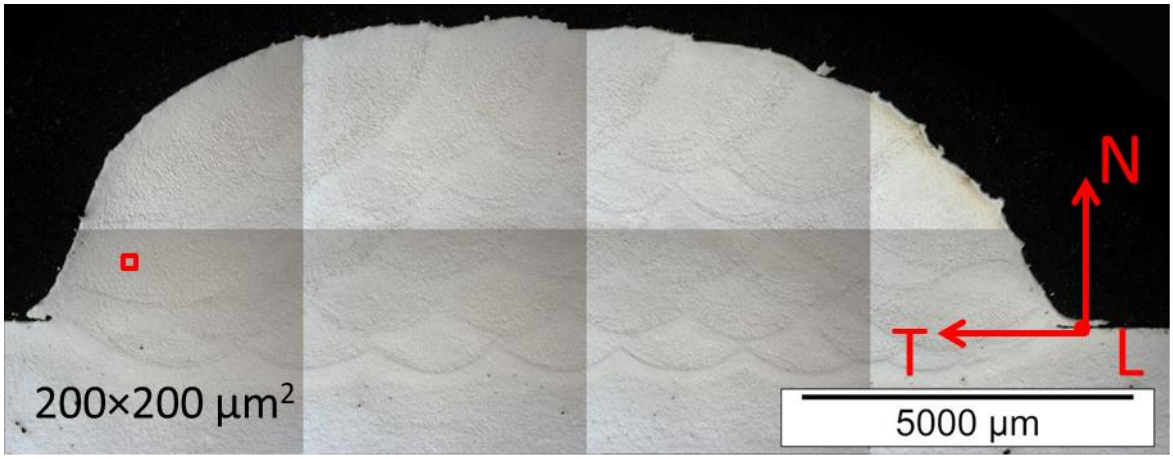

Figure 42: Optical image of the cross-section of the clad with marked directions and area which was observed using OIM.

6.2 Experiment

Laser cladding was carried out using an IPG 3 kW Yt:YAG single-mode fibre laser with off-axis powder feeder in against hill conditions. Laser power density of 90 J/mm^2 was applied to form clads in multilayers, see Figure 41. A five-layer sample was formed from six and seven overlapping beads on the substrate made of AISI H11 tool steel, see the cross-section in Figure 42. The longitudinal axes of the beads in one layer were 2 mm apart, and the tracks in the next layer were placed at the intermediate positions of the tracks in the previous layer. The real structure, the state of residual stress, hardness distribution, and wear resistance were investigated in three identical experimental samples.

6.2.1 Metallography

For metallographic analysis, the sample was cut on the T-N plane, then ground, and afterwards, polished. The steel surface was treated with an etchant of 2% Nital (2% nitric acid in ethanol) and Picral (1 g picric acid, 5 mL HCl, 100 mL ethanol). The analysis was described based on images obtained using a Neophot 32 metallographic microscope and JEOL JSM-7600F scanning electron microscope equipped with a low-angle backscattered electron detector. The legend of the images contains the scale and the designation SEI or LABE. SEI indicates that the images were taken using secondary electrons and LABE that the images were taken using a low-angle backscattered electron detector. The LABE detector is more sensitive to surface information. It can describe both compositional and topological information in one image.

6.2.2 Hardness Tests

Hardness measurements made through instrumented indentation technique (HV_{IT}) were carried out using a NHT2 nanoindentation instrument with diamond Berkovich indenter. The indentation cycle consisted of loading to a maximum force of 500 mN, holding at maximum load, and unloading for 30 s, 10 s, and 30 s, respectively. Data were evaluated by the Oliver-Pharr method [87] [88]. Two lines of indentations were made with 75 μm spacing and the values were averaged. For further hardness measurements, a Vickers

hardness tester was used equipped with a Vickers diamond quadrilateral pyramid with a top angle of 136°. The load during the experiment was 1 kilopond for thirteen seconds.

6.2.3 Microstructure

In order to determine the phase composition of the surface layer, diffraction patterns were obtained by measuring the clad with an X'Pert PRO MPD in classical Bragg-Brentano (BB) focusing configuration with a cobalt tube anode and 1×0.25 mm^2 pinholes. Measured diffraction diagrams were processed with X'Pert HighScore Plus and crystallographic phases were identified using a PDF-2 database. Quantitative analysis was evaluated using Rietveld analysis in MStruct software [89]. The effective depth of penetration (T^{eff}) corresponds to the thickness of a surface layer that provides about 63 % of the diffracted intensity. In the case of the wavelength used, the T^{eff} is about 5 μm. Crystallite size and microdeformation values were used to calculate dislocation density using the Williamson and Smallman method, see equation (1).

The OIM data was collected using a Philips XL 30 FEG scanning electron microscope equipped with a TSL OIM system based on a DigiView 3 camera. An accelerating voltage of 25 kV and step size of 0.2 μm and 50 nm were used for scanning. Misorientation larger than 5° was defined as a crystal boundary. All EBSD data were analysed with TSL OIM Analysis 7.3.0 software and only data points with a confidence index higher than 0.05 were used. The analysed area is indicated by a red square in Figure 42.

6.2.4 Residual Stress Analyses

Surface macroscopic residual stress was described using X-ray diffraction and an X'Pert PRO MPD diffractometer with chromium radiation. The values of surface macroscopic residual stress were calculated from the lattice deformations, which were determined based on experimental dependencies of 2θ ($sin^2\psi$) assuming a bi-axial state of residual stress without gradients in the normal direction, where θ is the diffraction angle, ψ the angle between the sample surface and the diffracting lattice planes [90]. The diffraction angle was determined as the centre of gravity of the Cr$K\alpha_1\alpha_2$ doublet diffracted by the $\{211\}$ crystallographic lattice planes of the α-Fe phase. The X-ray elastic constants ½s_2 = 5.76 TPa^{-1}, s_1 = –1.25 TPa^{-1} were used to calculate stress using X'Pert Stress software.

The sample was analysed by XRD in both the perpendicular T and parallel L directions to the cladding. The irradiated volume was defined by experimental geometry, the effective penetration depth of the X-ray radiation (approx. 4–5 μm), and the pinhole size (1×1 mm^2).

Neutron diffraction measurements to describe bulk macroscopic residual stress were performed at the Neutron Physics Laboratory of the Centre of Accelerators and Nuclear Analytical Methods at the Nuclear Physics Institute of the Czech Academy of Sciences [91] using an SPN-100 two-axis diffractometer and a 2D ^{3}He position-sensitive detector with an active area of 230×230 mm^2 and resolution of 2×2 mm^2. The wavelength of the beam was set to $\lambda = 0.213$ nm with a bent Si(111) crystal monochromator. Cd-slits of 2×5 mm^2 were used to shape the incident beam and a radial collimator with a full width at half maximum (FWHM) of 2 mm defined the gauge volume. The sample was placed with a vertical axis for strains in the N and T directions, while for strain in the L directions the sample was placed horizontally with the L-T plane parallel to the scattering vector. The 2D area detector was positioned at $2\theta = 63°$ to study the reflection of {*110*} crystallographic lattice planes of the α-Fe phase. Five lines were scanned (for three sample orientations) in the normal direction in a T-N plane in the middle of the sample with 2 mm steps for the substrate and 0.5 mm steps in the cladded region. A Gaussian function was used to fit the diffraction peaks using StressTex-Calculator software [92].

Bulk residual stress in the L, N and T directions were calculated with Hooke's law using Young's modulus $E = 214.9$ GPa and Poisson's ratio $\nu = 0.242$ corresponding to the {*110*} plane calculated using the XEC program by Wern [93]. Measurements were performed at the middle in the longitudinal direction; therefore, a homogeneous distribution of residual stress in this region was assumed and stresses in the transversal direction were self-equilibrated. This assumption is based on the requirement that force and moment must balance across any selected cross-section. In the absence of confident stress-free references for both substrate and cladded regions, the equilibrium conditions were applied. Therefore, scanned lines in the substrate were used to calculate the stress-free reference for this part. With the scanned line at the centre (where the cladded volume is higher), the stress-free reference of the cladded region was calculated assuming a linear dependence across the heat-affected zone from the substrate to the cladded region.

6.2.5 Tensile Testing

For tensile testing, volume from 14 layers with a length of 50 mm, widths of 40 mm and 30 mm, and height of 10 mm was cladded onto a substrate made from AISI H11 tool steel, see Figure 43. The cladding began in the upper right corner and continued to the left. The volume on the right was cladded first, the left one second. From the cladded volumes, specimens for tensile tests with width of 1.6 mm in the narrowest area and thickness of 1.6 mm were cut using EDM (Electric Discharge Machining), see Figure 43. Samples 1–4 were prepared in a perpendicular direction to cladding, samples 5 and 6 were parallel. For each number, two samples were prepared. Sample *A* was cut from the upper layers and *B* from the bottom. Samples from the substrate were marked *S*. This atypical sample shape was used due to the requirements of the in-situ SEM tensile stage designed for an in-situ EBSD experiment.

The OIM data for EBSD was collected using a Lyra Tescan scanning electron microscope equipped with a TSL OIM system based on a Hikari Super camera. An accelerating voltage of 25 kV and step size of 0.7 μm were used for scanning. Misorientation larger than 5° was defined as a crystal boundary. All EBSD data were analysed with TSL OIM Analysis 7.3.0 software and only data points with a confidence index higher than 0.05 were used. The electron microscope was equipped with a Kammrath & Weiss Tensile/Compression 5 kN Module. Sample elongation was obtained from jaw movement and a displacement rate of 5 μm/s was used. Hardness of tensile specimens was obtained using a Vickers hardness tester and at least six values were averaged from both sides of the sample.

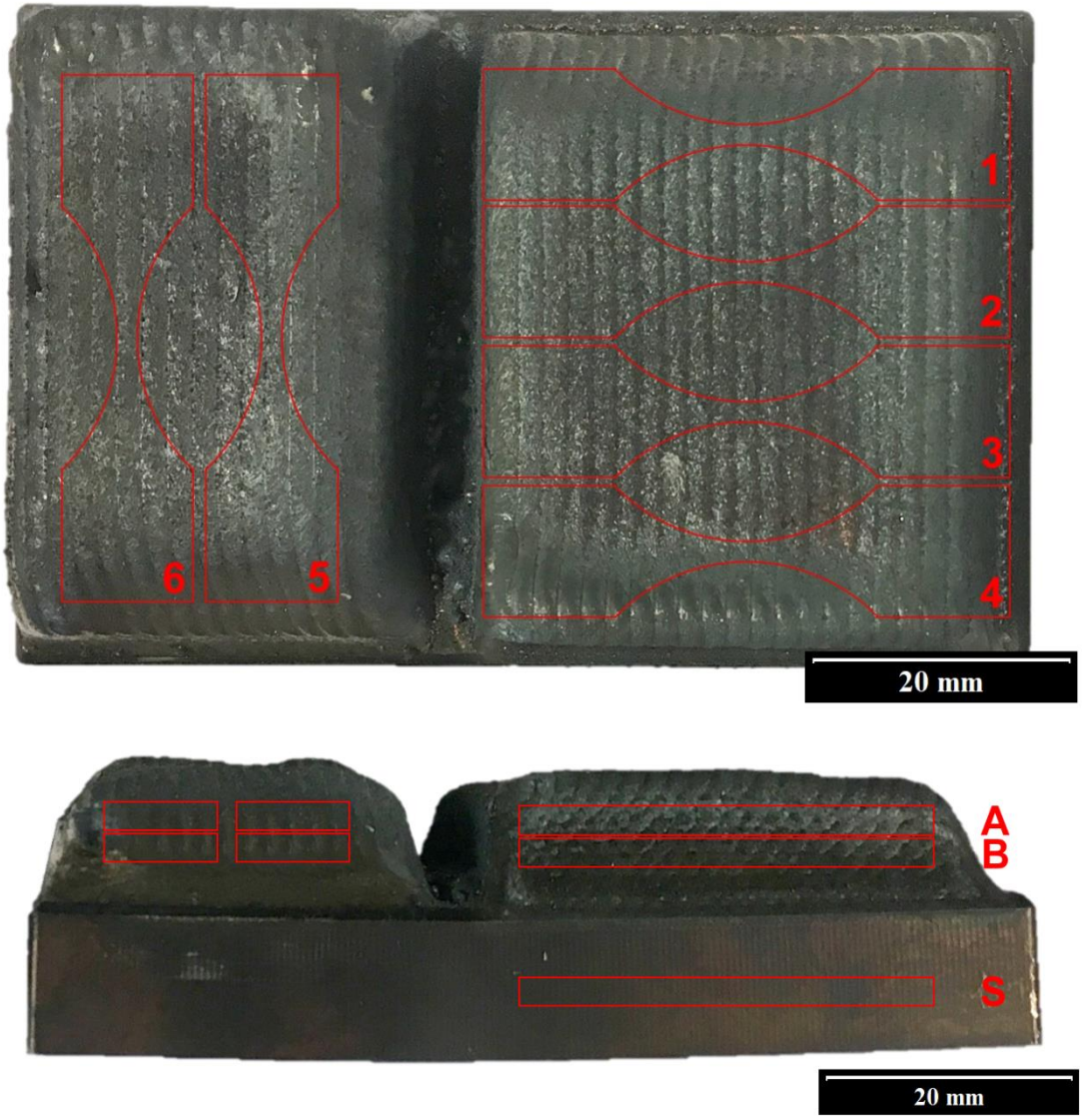

Figure 43: Top and side view of the cladded volumes with specimens marked for tensile testing.

6.2.6 Wear Resistance Testing

Wear resistance properties of laser-cladded material were studied using a dry sliding pin on disk test and CSM HT Tribometer. Figure 44 shows a pin that was cut from the cladded material. The pins were 6 mm in diameter and their cladded side was rounded to a ball shape. During the sliding test, the pin was fixed in a pin holder and the pin axis made an angle of 45° to the normal of the disk surface. The pin holder was continuously loaded with 5 N, 10 N, and 15 N, respectively, and the rotation speed of the disk was set to a value that corresponds to a sliding speed of 3 to 15 cm/s at ambient temperature. The number of rotations was fixed to reach a sliding distance of 500 m. Both contact surfaces

were polished before the test with 800 grit sandpaper. The disc was made of EN 100Cr6 (AISI 5210) steel with a hardness of 840 ± 10 $HV_{IT}1.0$. The worn surface, see Figure 45, was analysed with a confocal microscope and the worn volume was evaluated using NFMsurf 6.1 software. From the volume, the specific wear rate was calculated, which is the ratio of volume, load, and sliding distance.

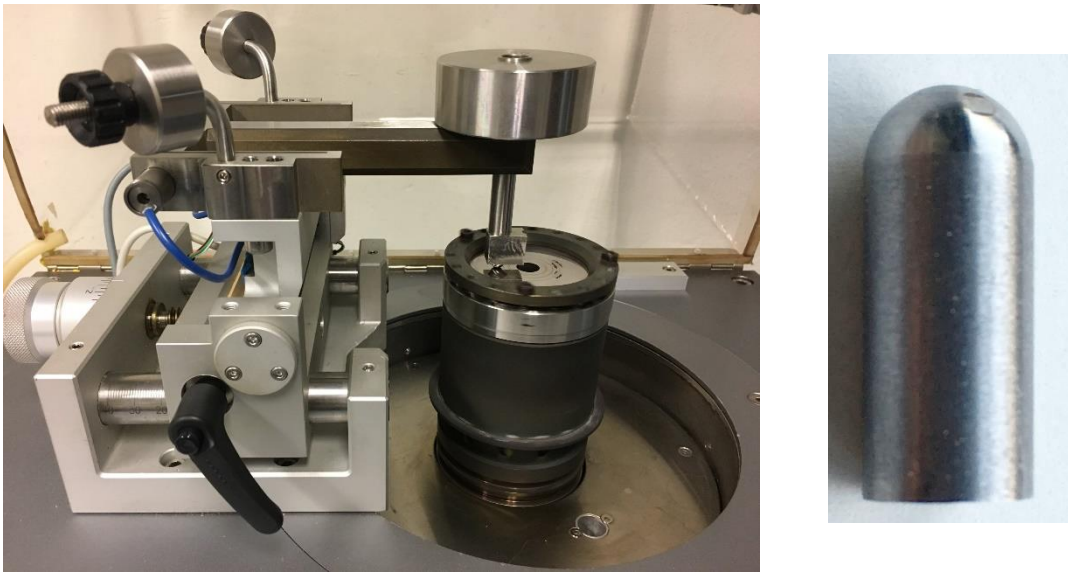

Figure 44: CSM HT Tribometer and pin with ball-shaped cladded side.

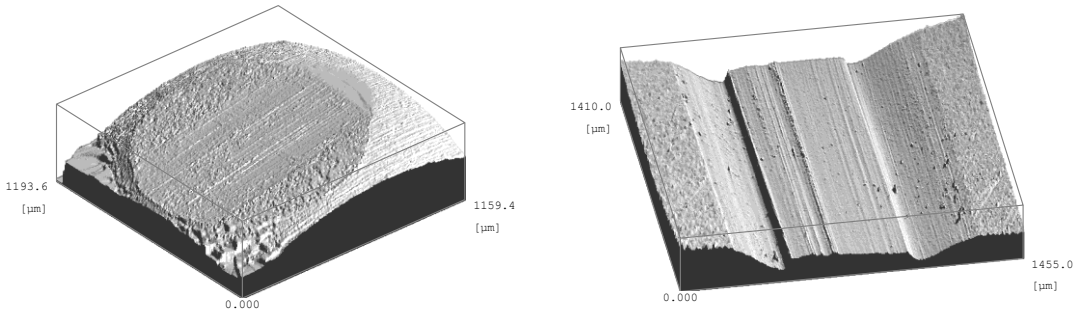

Figure 45: Example of worn surface of pin (left) and disk (right).

6.3 Results and discussion

The following subchapters will describe the results and discuss their consequences. First of all, the microstructure was described using an optical, electron microscope and EBSD technique. The course of hardness within the thickness of the cladded volume was also characterized. In the next step, the real structure and residual stress of the surface of the clad were investigated. Bulk residual stresses were obtained by neutron diffraction. Furthermore, the influence of tensile strain on the microstructure was investigated, where the hardness of the test sample was correlated with tensile strength. Subsequently, wear resistance was analysed, which is important to monitor for the durability of the repaired mould. Last but not least, it is necessary to describe the effect of surface finishing, as the surface of the clad will always be machined. The distribution of the real structure, residual stress, and hardness was monitored on the ground surface.

6.3.1 Metallography

The shape and microstructure of a cross-section of AISI H13 tool steel with five layers of cladding were described.

6.3.1.1 Light microscopy

In the macro image of the clad in Figure 46 with structure revealed by picral (4% picric acid), several different areas can be characterized that differ from each other. The top layer, which was cladded last, has a significantly different structure than the first. Additionally, a ferritic area occurs between these regions. The transition between the clad and the base material was also observed. The areas and their microstructure were described by electron microscopy.

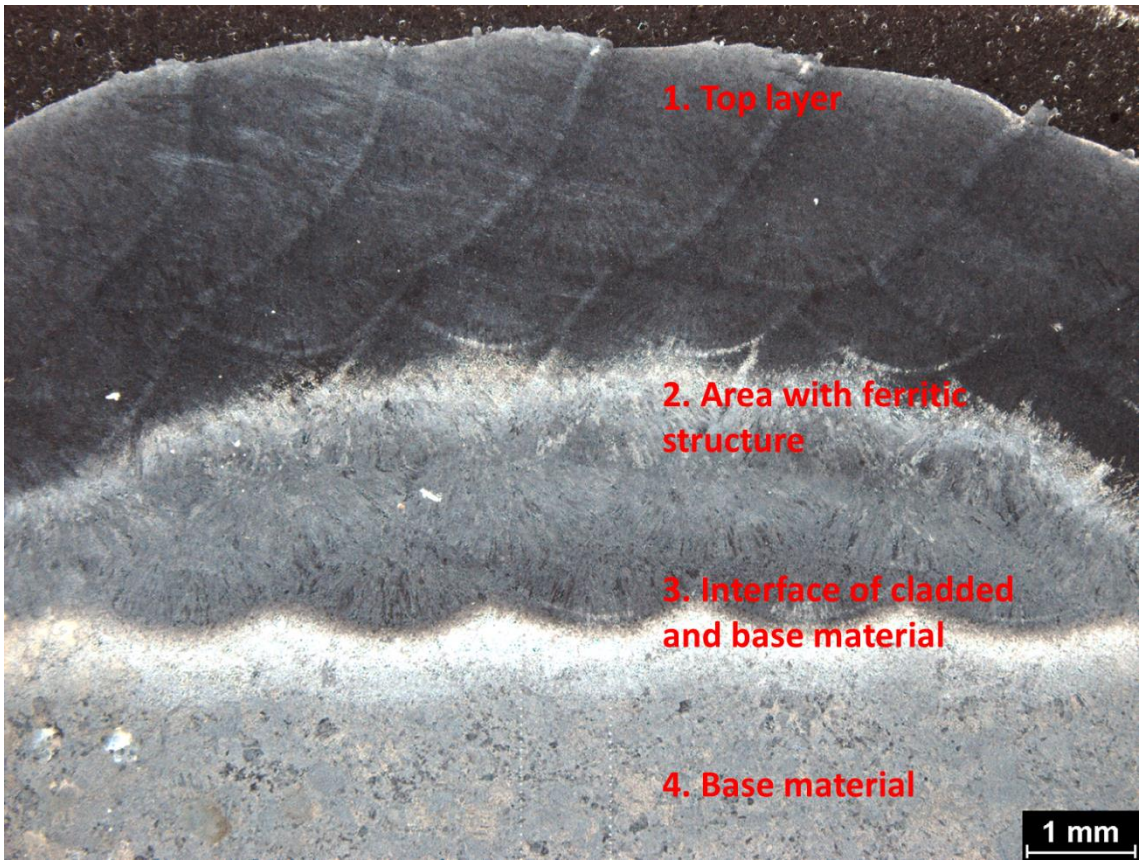

Figure 46: Macro image of the clad with marked areas that differ significantly.

6.3.1.2 Electron microscopy

6.3.1.2.1 Top layer

In this area, martensitic structure with a low proportion of bainite predominates. Occasionally, localized areas with increased bainite can be observed. Ferritic envelopes are formed around the grains, which also cross the primary austenitic grains. Retained austenite (RA) in the structure could also be observed, see Figure 47. Cracks can be found on the surface, see Figure 48, which were probably caused by cooling. The image also shows an island of bainite, in the upper layer it is a unique occurrence.

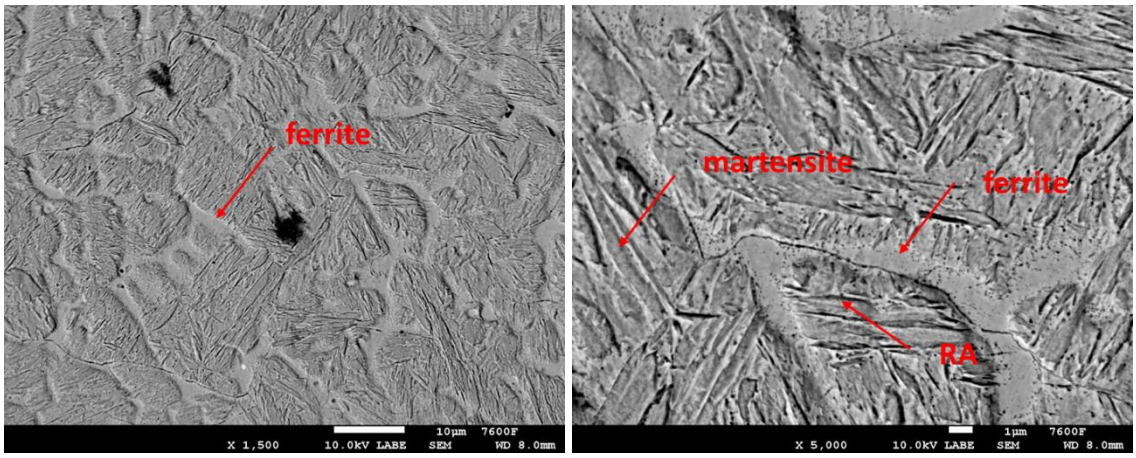

Figure 47: Ferritic envelopes, inside martensitic needles and retained austenite (RA).

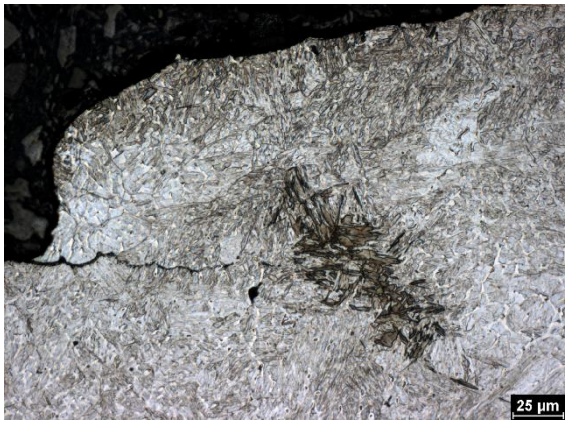

Figure 48: Optical image of the clad surface with a crack, the dark area is bainite.

6.3.1.2.2 Area with ferritic structure

In this area there is ferrite and mostly bainite with a low proportion of martensite. Inside the needles and laths are fine carbides. The presence of ferrite in the microstructure will have a significant effect on the decrease in hardness. In the ferritic phase there are bounded areas with carbides (using EDS a higher proportion of C, V, Mo was found), or other phases (most often based on V), see Figure 49.

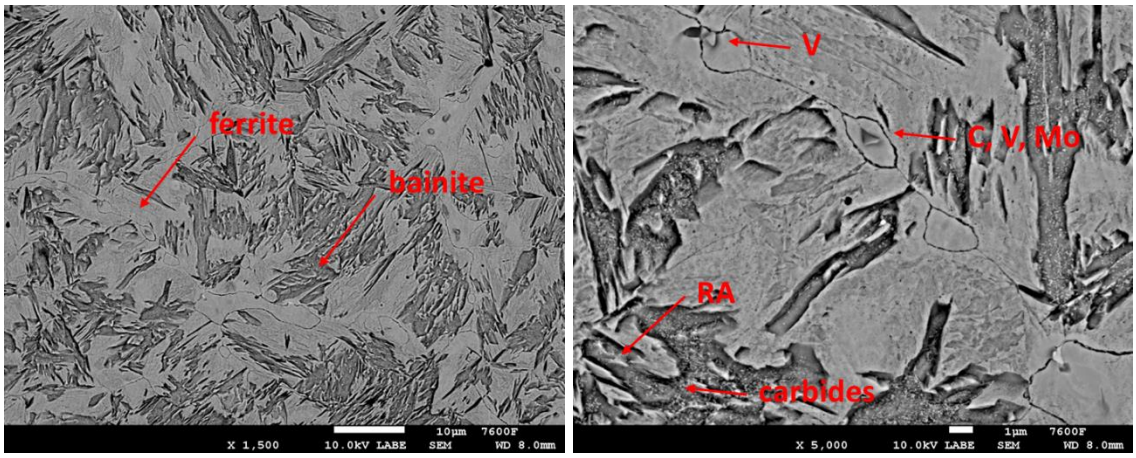

Figure 49: Microstructure of ferritic area.

6.3.1.2.3 Interface of cladded and base material

The first layer itself consists of a mixture of martensite and bainite, acicular ferrite, and retained austenite, see Figure 50. Occurrence of martensite-austenite laths is also likely. The upper part of the interface is martensitic with more pronounced bainitic regions, see Figure 51. The bright areas in Figure 52 from a bright-field optical microscope are ferrite, which again forms envelopes. The lower part of the interface, respectively the heat-affected zone (HAZ) is strongly tempered, so there is a large amount of carbides (C+Cr, C+Mo, C+Cr+Mo+V), ferrite, martensite-austenite (M-A), and possibly isolated islands of pearlitic colonies, see Figure 53 and Figure 54.

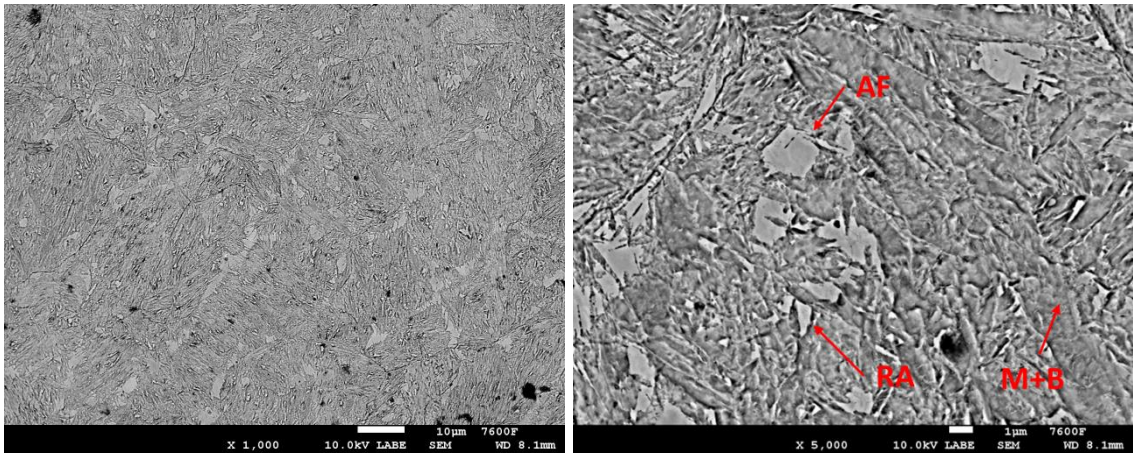

Figure 50: Microstructure of the first layer with acicular ferrite (AF), martensite/bainite (M+B) and retained austenite (RA).

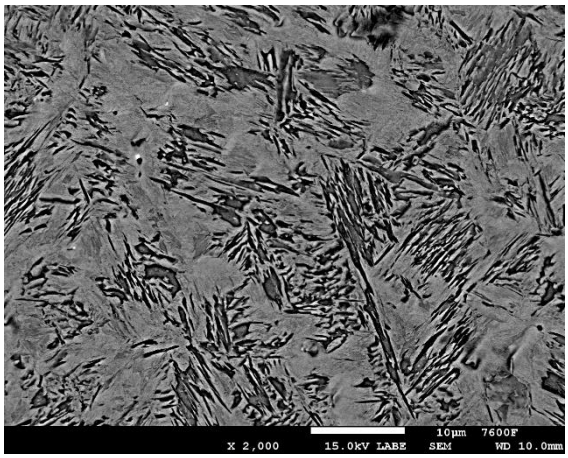

Figure 51: The upper part of the interface with bainitic colonies with occasional occurrence of martensite.

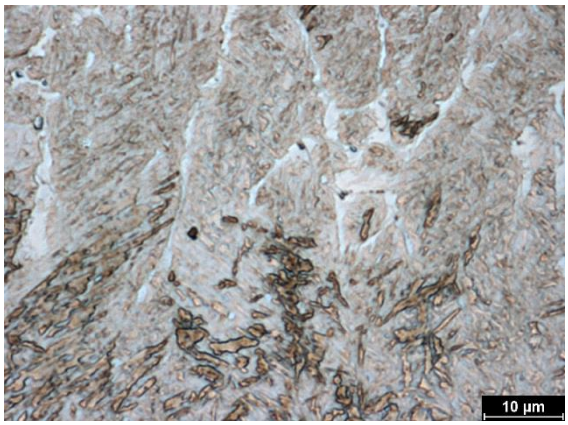

Figure 52: Microstructures of the upper part of the interface with bainitic colonies and ferritic envelopes.

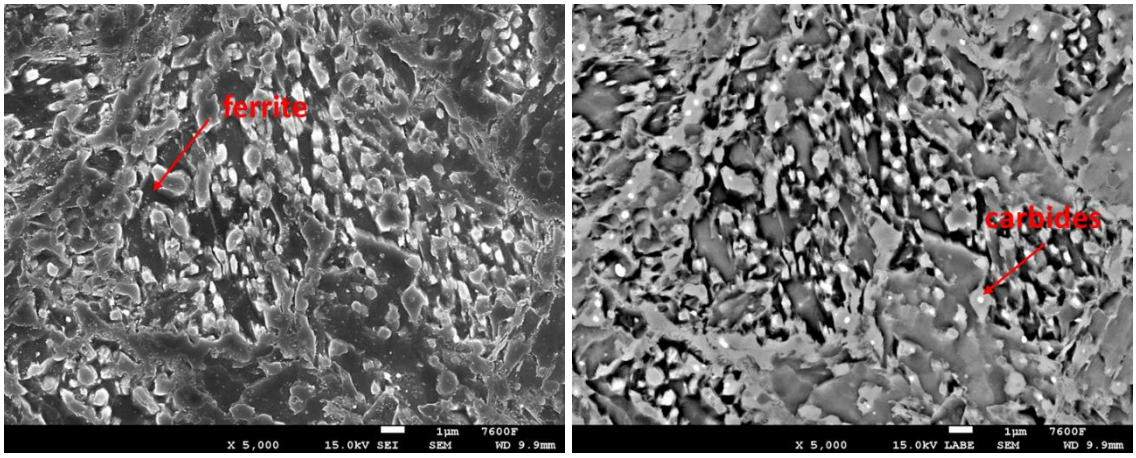

Figure 53: HAZ microstructure with intercritical ferrite, martensite-austenite regions, and carbides.

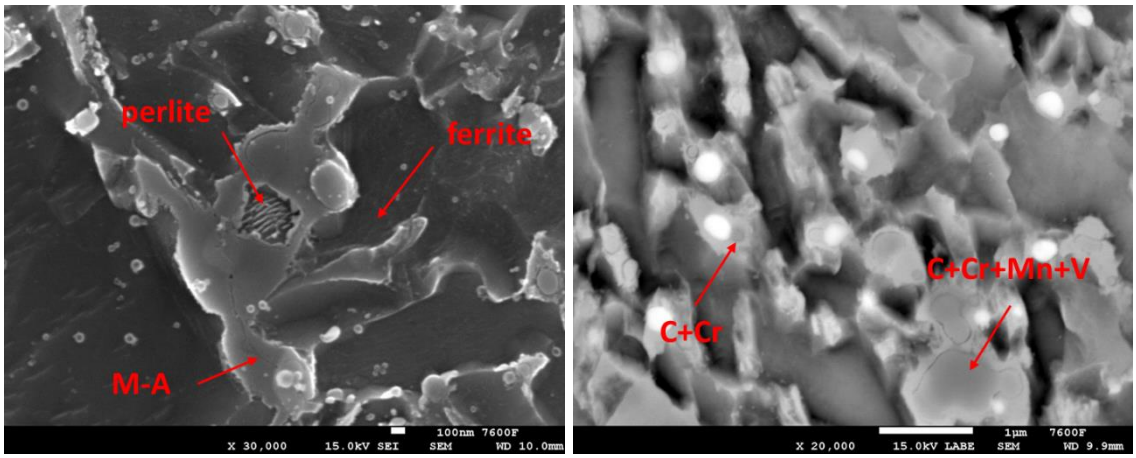

Figure 54: Isolated islands of perlite, martensite-austenite (M-A), and carbides in HAZ.

6.3.1.2.4 Base material

The base material consists of tempered martensite. Fine carbides are found in the matrix and along the boundaries of the primary austenitic grains, see Figure 55.

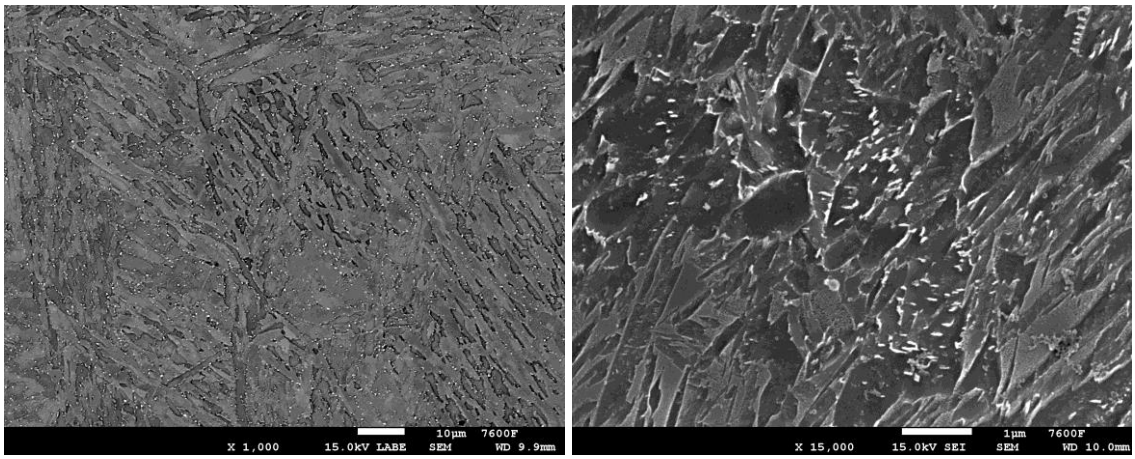

Figure 55: Fine carbides in the structure of the base material.

6.3.2 Hardness distribution

The hardness of the five-layered clad was described from the surface of the clad to the substrate, see Figure 56. The microstructure was first revealed using nital, and then picral was used to etch martensitic grains. From the surface of the clad (top), two lines of indents were made with a spacing of 75 micrometres, see Figure 57.

The hardness of the clad to a depth of approximately 2.5 mm, which corresponds to the last two layers, is around 700 HV_{IT}. This is followed by a significant drop in hardness of 200 HV_{IT}, which reaches its minimum at a depth of 3.3 mm. Then the values

rise again to the same values as for the surface. From 5.2 mm, the hardness decreases to 230 HV_{IT}, which corresponds to the annealed state of H11 steel.

The area with lower hardness overlaps with the darker area in the cross-section and an area with ferritic structure which was found in the description of the microstructure, see Figure 56. The change in the microstructure and thus the change in hardness was due to the cladding of the last layers. According to Figure 16, very fast quenching after cladding took place within a few seconds, because the resulting hardness reaches 700 HV_{IT}. The decrease in hardness corresponds, according to Figure 17, to annealing at a temperature of approximately 600°C. This effect is very interesting, as the second and third layers were annealed due to heat input from the cladding of following layers, not the first one. From this it can be concluded that the strategy of cladding process and temperature control can significantly affect the resulting material properties. On the other hand, it is very important to set the process to avoid low hardness close to the surface. Part of the cladded volume is always machined and lower layers serve as the functional surface. Low hardness values on the surface of moulds or gears can significantly reduce service life.

Figure 56: Image of a cross-section of the clad with visible microstructure and indents.

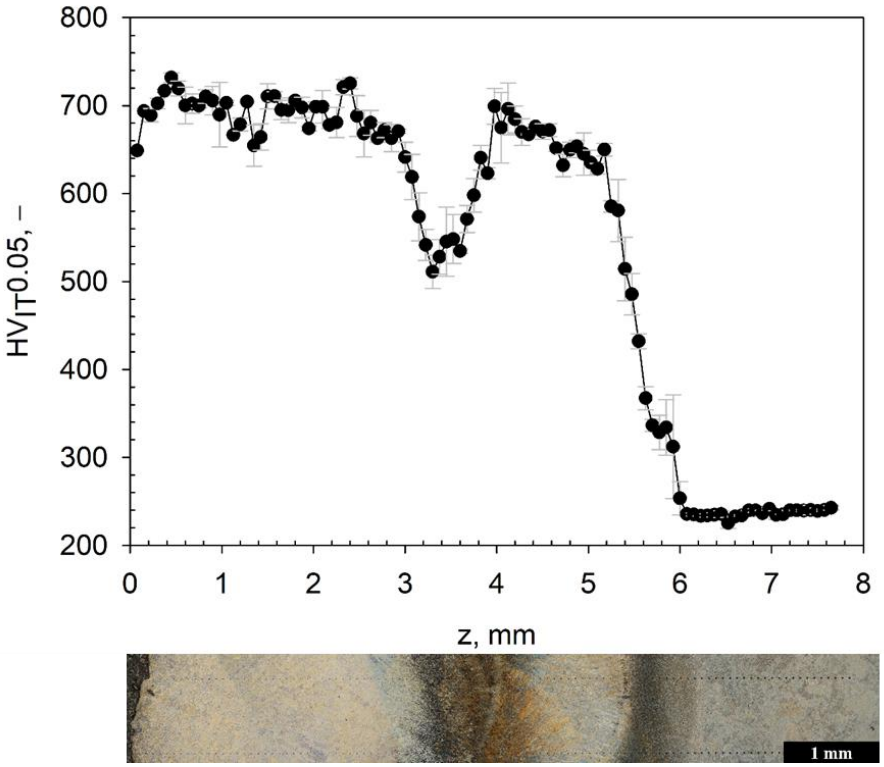

Figure 57: Hardness profile from the clad surface to the substrate in comparison with a macro image.

6.3.3 Microstructure

6.3.3.1 Electron Diffraction

The microstructure was further observed in a cross-section of the clad using electron backscattering diffraction, see inverse pole figures (IPF) of ferritic phase in Figure 58 and detail in Figure 59. Due to the arrangement inside the electron microscope, the area at the edge of the cladded volume was analysed, see Figure 42.

The figures clearly show the original austenite grains 20–50 μm in size that were established during the transition of the melt into a solid phase and which were subsequently transformed into martensitic or bainitic laths. It has to be noted that the EBSD technique is not able to directly distinguish ferrite and martensite in low carbon steels due to the low proportion of a/c lattice parameters of the tetragonal martensite lattice.

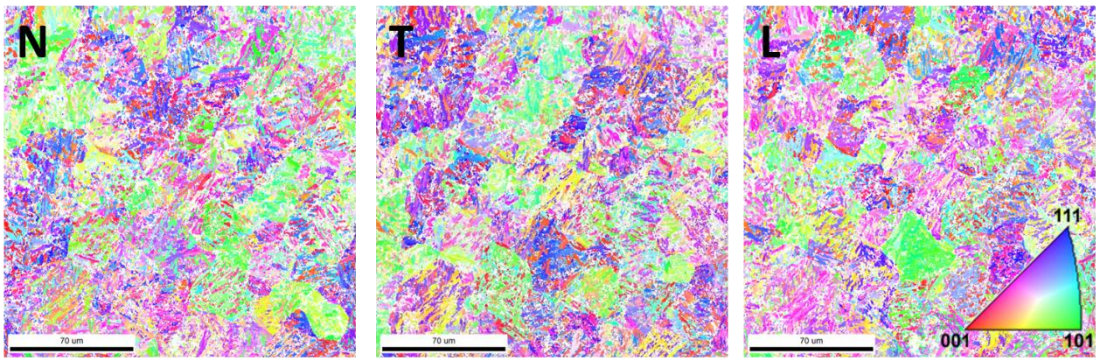

Figure 58: IPF maps of ferritic phase for different directions in the selected area, where N, T, and L denote the direction.

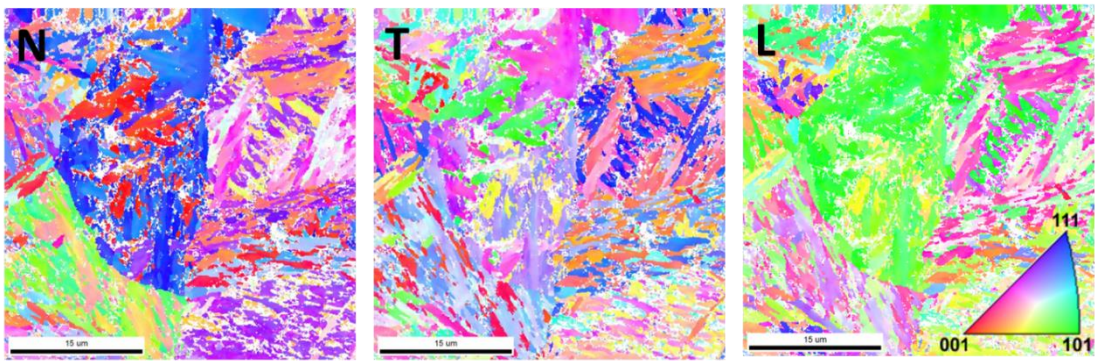

Figure 59: Detailed IPF maps of ferritic phase for different directions.

No other phases were indexed with sufficient confidence in the scanned area. Retained austenite and carbides of alloying elements can be expected according to previous results, but their confidence index was very small. It is very difficult for the software to distinguish between the cubic lattice of ferrite and $M_{23}C_6$ carbide, the only difference is the width of the Kikuchi lines. Information on the local chemical composition can also be used for indexing, but even this path did not lead to better phase resolution due to the different volume from which the information for both methods comes from, see Figure 10. Using diffraction methods, it was not possible to reliably identify the carbides in the clad.

6.3.4 X-ray Diffraction

The real structure was described on the surface of the clad, which was first lightly sanded with sandpaper to remove adhering partially melted powder particles and then electrolytically etched. As a result, a thin surface layer of approximately 150 μm was

removed without force and, most importantly, the surface was levelled. High surface roughness leads to undesirable effects in X-ray diffraction analysis, which has a penetration depth into metallic materials on the order of micrometres. On the one hand, the diffraction pattern deteriorates and, on the other hand, the residual stress is redistributed at sharp edges. Furthermore, the real structure was also described for a cross-section, mainly in order to characterize layers that show a different microstructure and hardness.

6.3.4.1 Surface real structure

The real structure of the surface is characterized in the following maps, each of which consists of 33 values and the data are linearly interpolated between them. Figure 60 describes the phase composition of the clad surface, see Figure 41. Only ferrite and retained austenite were characterized on the surface by quantitative phase analysis. The proportion of phase composition and real structure was determined by Rietveld refinement, where Figure 61 describes the crystallite size and Figure 62 the microdeformation. It should be noted that due to the low carbon content in the steel, X-ray phase analysis cannot distinguish between ferrite and martensite and bainite, due to the low proportion of a/c lattice parameters. The error in calculating the proportion of ferrite is less than 0.1 %, the total error of the phase analysis depends on many factors, but is stated to be approximately 1 to 2 % [94]. The average crystallite size error is 1.3 nm while for microdeformations it is 0.9×10^{-4}.

The proportion of ferrite and thus also the proportion of retained austenite varies by up to 10 wt. %. From the figures it is possible to observe a certain correlation between the proportion of retained austenite and crystallite size. Crystallite size increases with a larger proportion of retained austenite and vice versa. The microdeformation shows a lower variance and no obvious relation to other parameters of the real structure.

Based on these results, it can be stated that the cladding is not homogeneous in all places. An inhomogeneous structure is formed on the surface of the clad, which therefore has different mechanical properties.

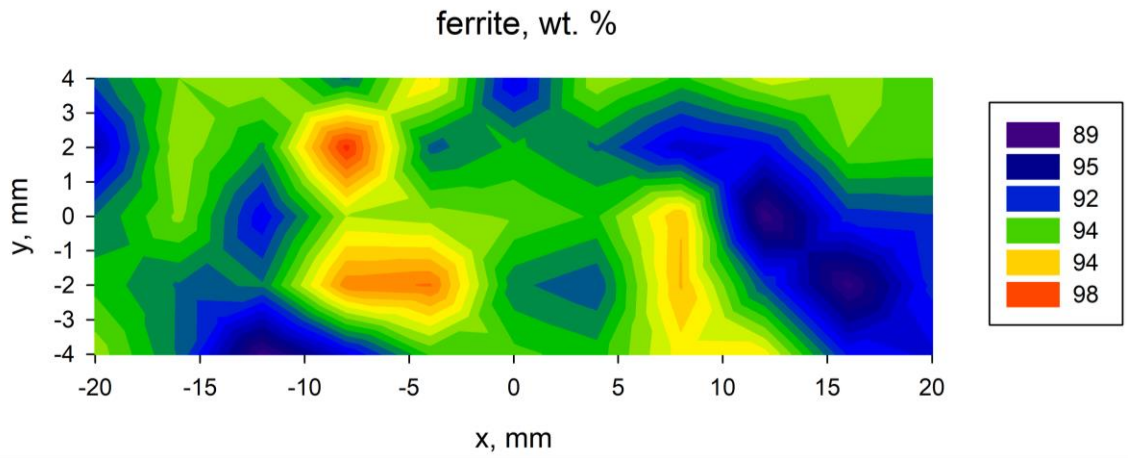

Figure 60: Map of the proportion of ferrite on the surface of the clad.

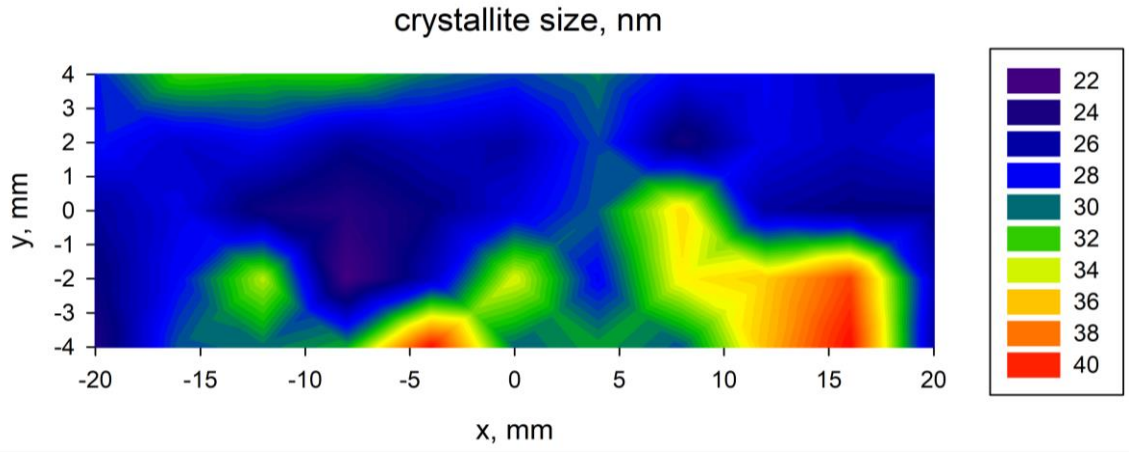

Figure 61: Map of crystallite size of ferrite phase on the surface of the clad.

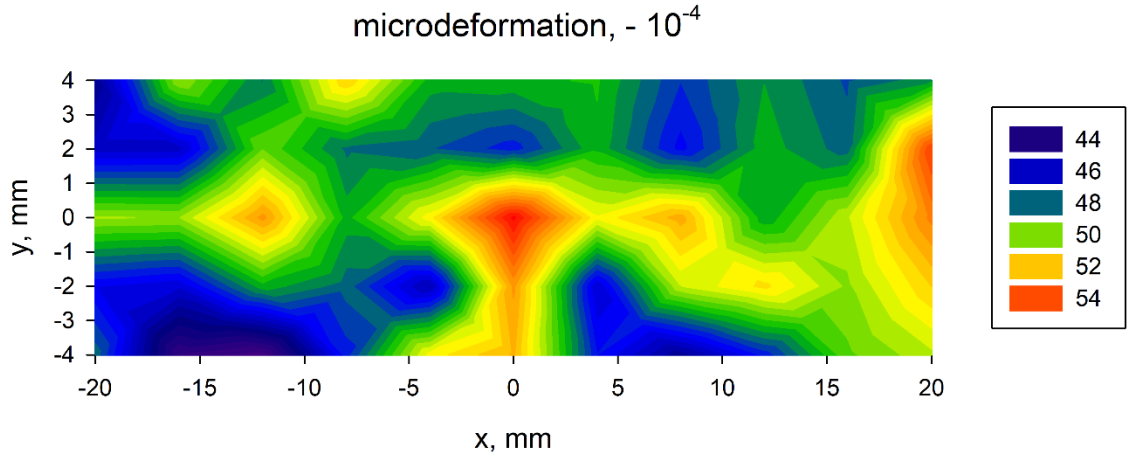

Figure 62: Map of microdeformation of ferrite phase on the surface of the clad.

6.3.4.2 Real structure in the cross-section

The real structure was also investigated in a cross-section of the cladded volume, where a phase analysis of each layer, heat-affected zone (HAZ), and substrate was performed. In the following graphs describing the results, layers are numbered from the surface, i.e. the last cladded layer is numbered 1 and the first is numbered 5. The HAZ is numbered 6 and the substrate 7.

According to X-ray phase analysis, see Figure 63, the proportion of austenite is highest in the first cladded layer, approximately 11 wt. %. On the contrary, the lowest proportion is in the area with lower hardness (Figure 57), less than 2 wt. %. Using X-ray phase analysis, only ferrite could be determined in the HAZ and the substrate. There was one extra maximum on the diffraction pattern of the substrate. This is probably M_7C_3 carbide, where M is different alloying elements. However, based on one maximum, carbides were not sufficiently characterized by X-ray diffraction as they are very small and probably monocrystalline.

The crystallite size according to Figure 64 is almost constant for both phases in the cladded layers. In area 4 it was not possible to determine other parameters of the real structure, because the proportion of retained austenite is very low. The crystallite size increases significantly in the HAZ and substrate, with 500 nm being the maximum that the MStruct software can evaluate. Since the H11 tool steel substrate was soft-annealed, it showed a significant coarsening of the grains, which have fewer dislocations. This results in higher values of crystallite size.

The microdeformation also differs depending on the layer, see Figure 65. The microdeformation of both phases is identical within the margin of error, again reaching the lowest values in the area with the lowest hardness, which indicates a higher temperature reached when cladding the other layers. The HAZ and substrate show low values due to heat treatment.

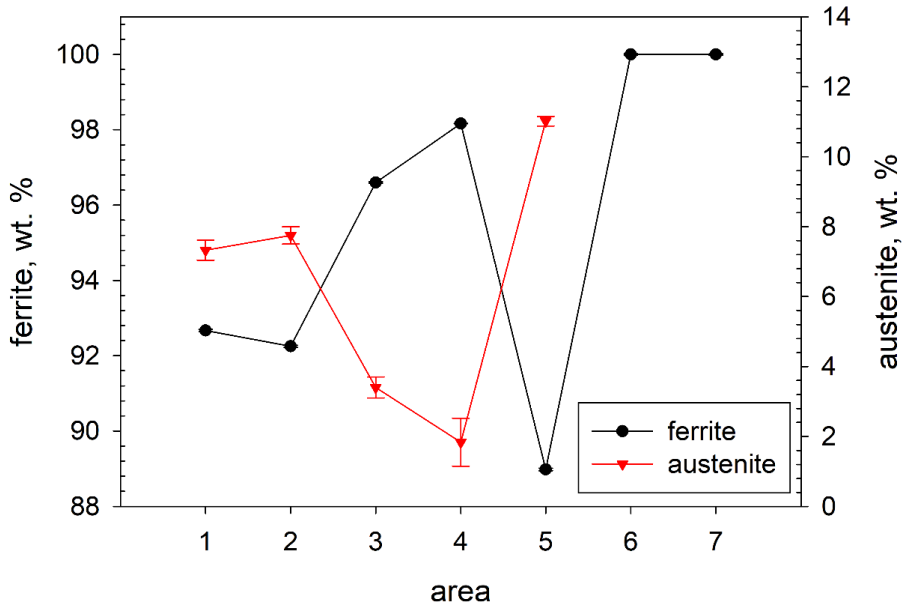

Figure 63: Phase composition of the cladded layers, where 1 is the last cladded layer, 5 the first one, 6 HAZ, and 7 substrate.

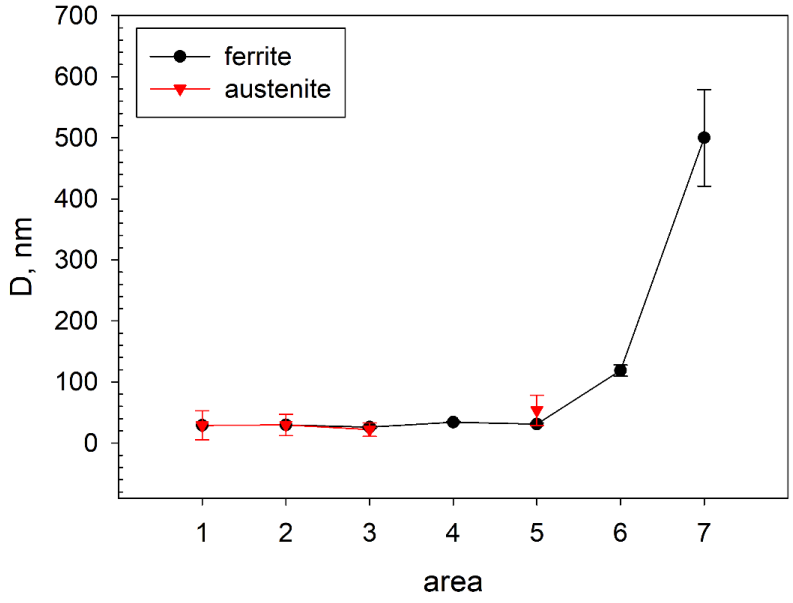

Figure 64: Crystallite size of the cladded layers.

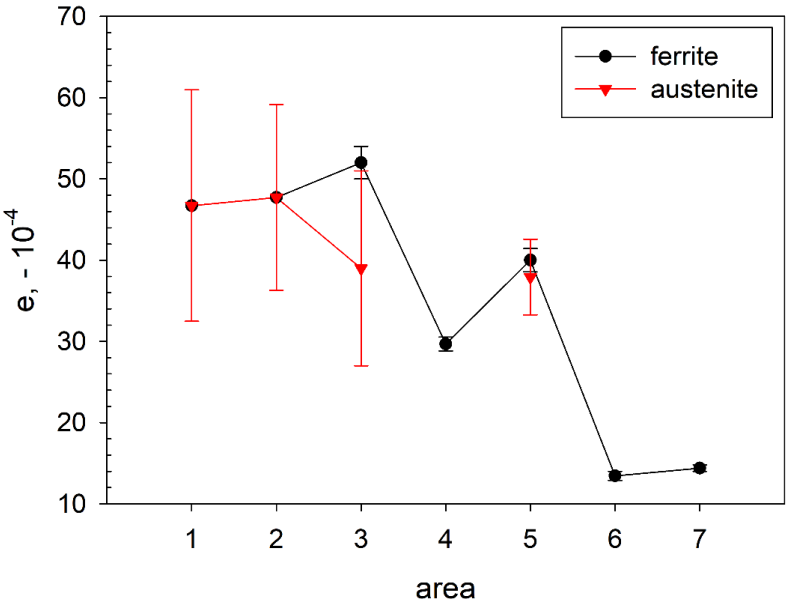

Figure 65: Microdeformation of the cladded layers.

6.3.5 Residual stress distribution

Using X-ray diffraction, the surface macroscopic residual stresses of the five-layer clad were determined. The sample was prepared in the same way as when analysing the real structure. Furthermore, bulk macroscopic residual stresses were characterized by neutron diffraction on the same sample.

6.3.5.1 Surface residual stress

Figure 66 and Figure 67 describe the surface macroscopic residual stresses in the L and T directions, i.e. in the cladding and perpendicular directions, respectively. The maps consist of 33 values and the data are linearly interpolated between them. The average error of the residual stress calculation is approximately 50 MPa for both directions.

Residual stress in the L direction mainly reaches compressive values, only at the edges are there areas with tensile stress. On the contrary, tensile residual stress predominates in the T direction, with only a few exceptions. Compressive residual stress has a positive effect on possibly slowing down crack growth, which spreads perpendicular to the beads. On the contrary, tensile stress in the T direction accelerates the propagation of cracks along the beads. The presence of such crack was detected in the cross-section.

This state of residual stress is surprising, since the greatest shrinkage due to cooling takes place in the direction along the cladding, the direction in which tensile

residual stress could be expected. At the same time, residual compressive stresses in the perpendicular direction have been observed in the literature for two-layer cladding [71]. Thus, even with a multilayer clad, the transformation effect prevails over the shrinkage.

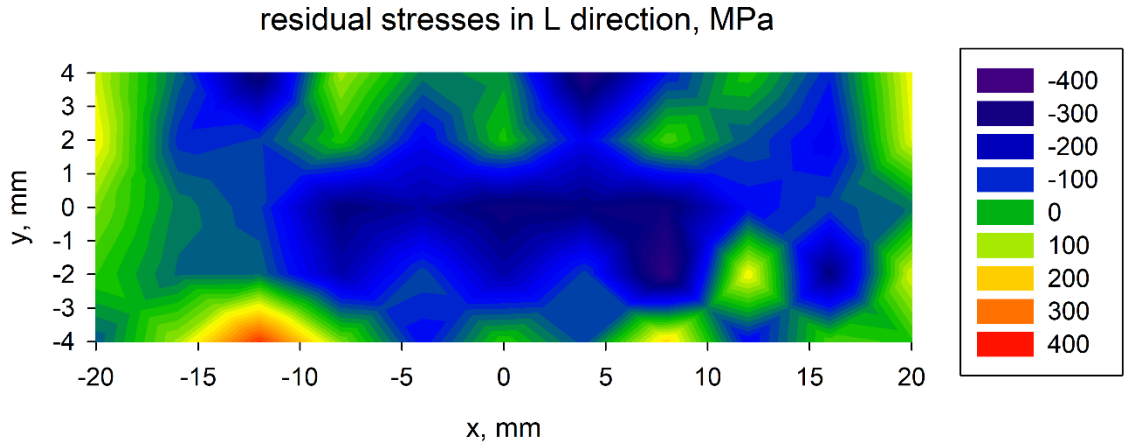

Figure 66: Map of residual stresses on the surface of the clad in the L direction.

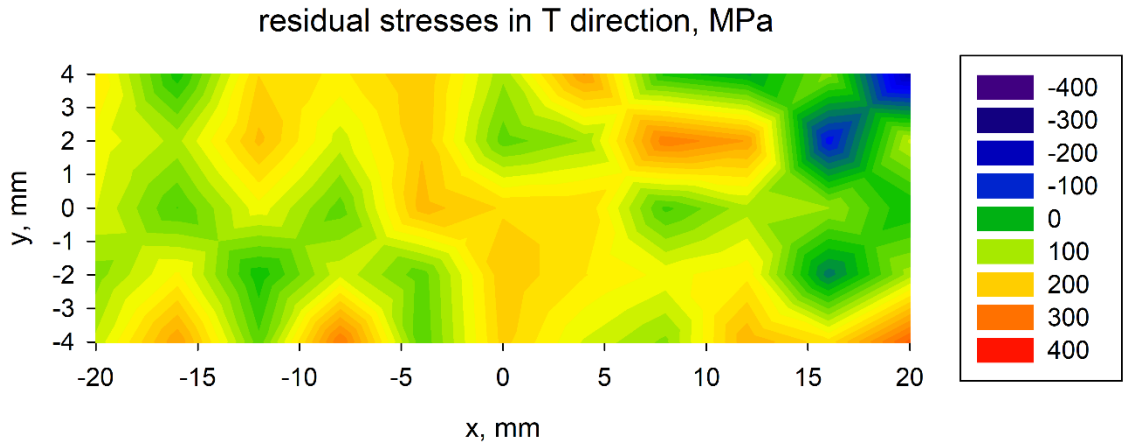

Figure 67: Map of residual stresses on the surface of the clad in the T direction.

6.3.5.2 Bulk residual stresses

The state of residual stress and the dependence of the FWHM parameter were determined using neutron diffraction in the middle of the sample in the plane perpendicular to cladding. Bulk macroscopic residual stresses are plotted in Figure 68, where all three major components of the stress tensor have been described. Only stresses with the gauge volume totally inside the bulk of the material are shown, therefore, the values are not up to the edges of the marked clad in the figure. The average statistical error of the residual stress calculation was approximately 13 MPa for all directions. The FWHM parameter was also evaluated from the diffraction patterns, see Figure 69.

It was found that the greatest gradient of residual stress (RS) is in the direction normal to the surface (N – normal direction). According to the literature study, for example [70] and [71], the maximum residual stresses are located 4 mm below the surface and compressive stresses prevail in the T direction. The substrate, on the other hand, exhibits tensile residual stresses. However, according to results in the clad itself in the T direction, tensile RS predominate. On the contrary, in the substrate compressive RS with one maximum of tensile RS approximately 3 mm below the surface of the substrate were determined. Unfavourable tensile stresses at the surface of the clad were determined in the L and also T direction. In the T direction, they reach higher values of up to 250 MPa. Tensile residual stresses reduce fatigue life and promote crack growth, which have been observed by electron microscopy, see subchapter 6.3.1.2.

FWHM parameter maps are similar for all directions. In the base material, the FWHM parameter is less than 0.5°. It increases towards the clad and exceeds 1° in the clad itself. The increase is due to the higher density of dislocations and the greater microdeformation, which was described by X-ray diffraction. Furthermore, it is caused by the microstructure of the clad, where retained austenite is present, which has a diffraction maximum close to the diffraction maximum of α-Fe. Due to the real structure and width of the diffraction maximum, these two peaks appear as one. Last but not least, the increased value of FWHM is due to the presence of martensite with a tetragonal lattice in the structure. The ratio of the a/c lattice parameters is very close to one, therefore it appears on the diffraction record as one with a larger FWHM value.

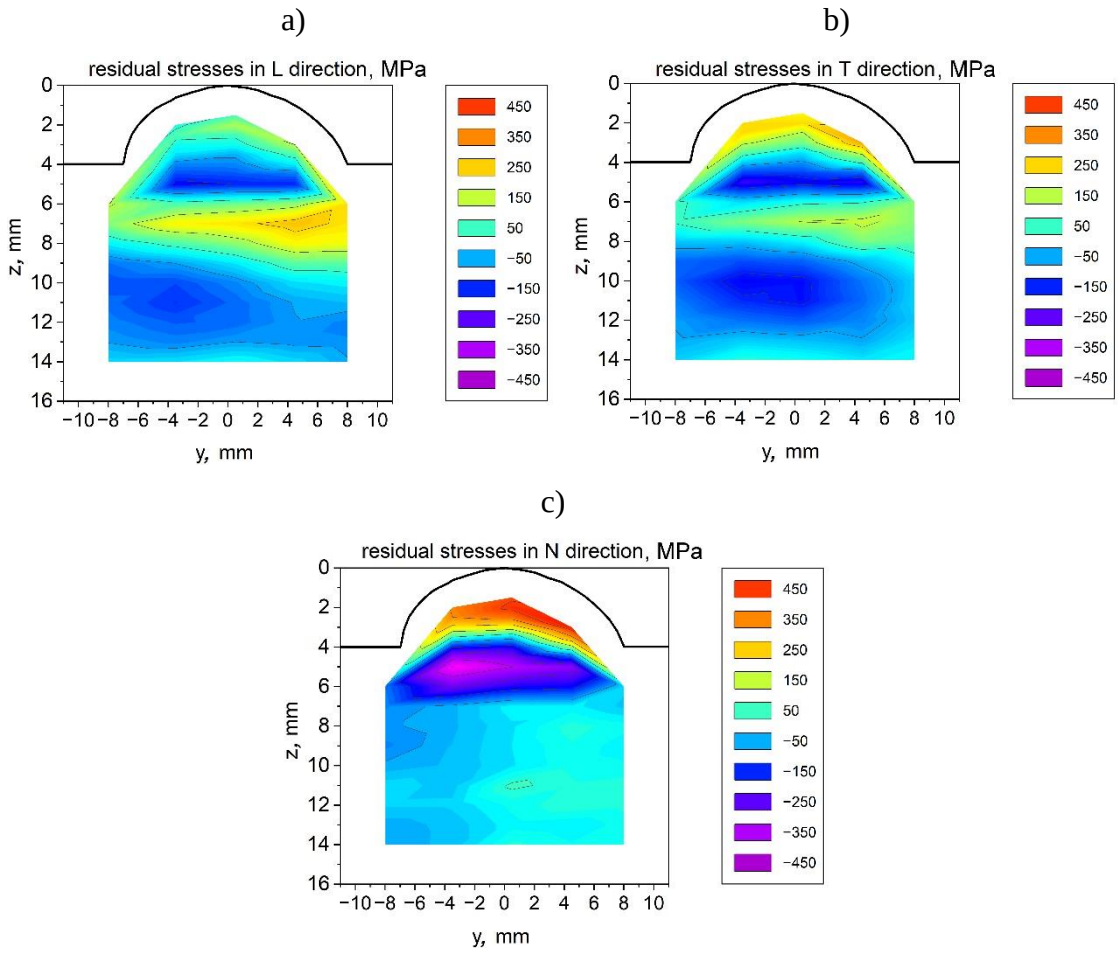

Figure 68: Map of bulk residual stresses in the cross-section of the clad in a) L, b) T, and c) N direction.

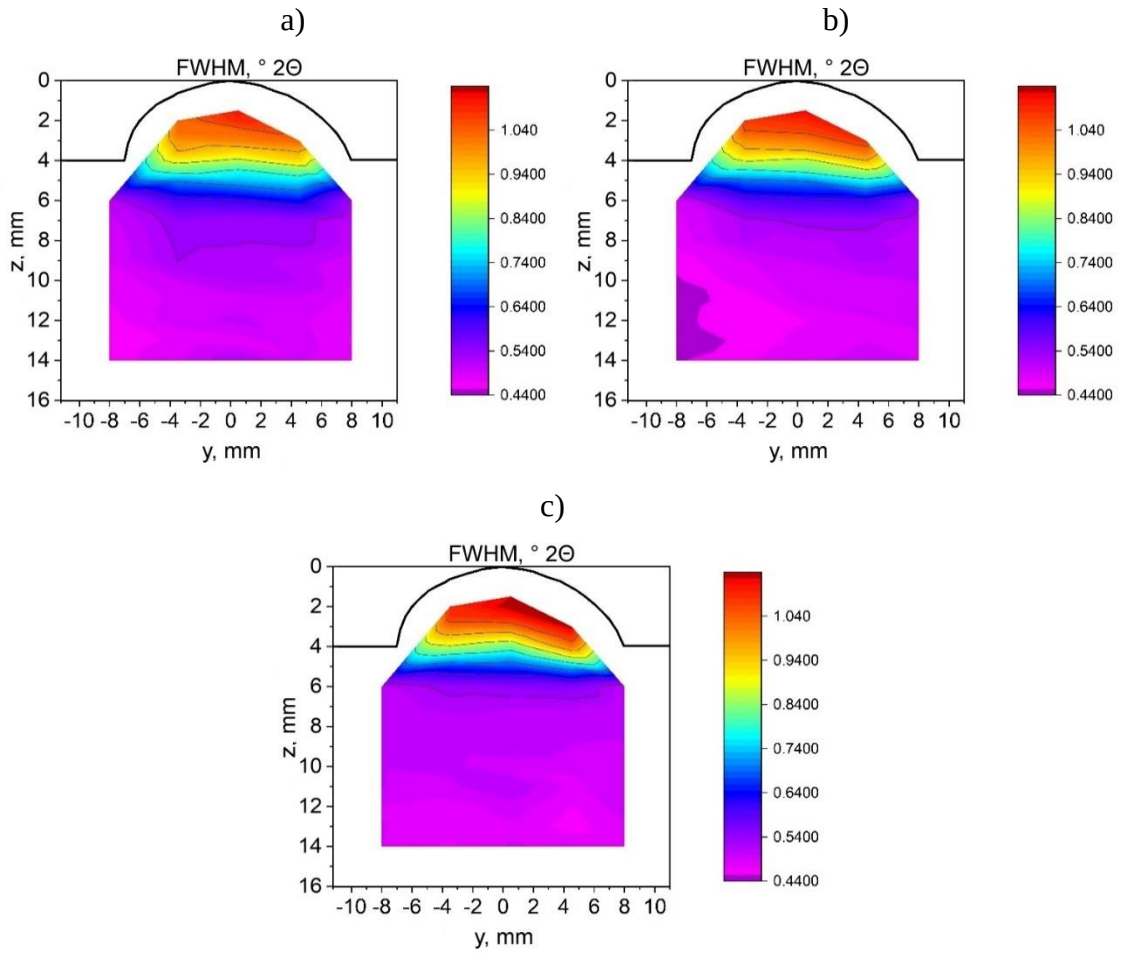

Figure 69: Map of FWHM parameter in the cross-section of the clad in a) L, b) T, and c) N direction.

6.3.6 Effects of tensile strain on the microstructure

Table 6 indicates the hardness values with standard deviation and tensile strength of selected samples where not all of the samples were subject to a tensile test. Samples 1–4 were prepared in a perpendicular direction to cladding, while samples 5 and 6 were parallel. For each number, two samples were prepared. Sample A was cut from the upper layers and B from the bottom. Samples from the substrate were marked S, see Figure 43.

Figure 70 graphically illustrates the hardness. The difference in hardness for samples A and B is clearly visible. According to [95], A samples with hardness higher than 600 HV1.0 had to be quenched using a cooling rate of 8°C/s. The reduced hardness of B samples (approx. 500 HV) in comparison with quenched condition of A samples was most probably due to the cladding of successive layers. This drop in hardness corresponds to tempering at more than 600°C for this steel [95]. Substrate was soft annealed before cladding.

Table 6: Hardness and tensile strength of the selected samples.

Sample	Hardness, HV1.0	Tensile strength, MPa
1A	569 ± 6	1809
1B	494 ± 12	1503
2A	553 ± 13	2052
3A	619 ± 11	
4A	620 ± 16	1994
4B	494 ± 14	
5A	656 ± 8	
5B	451 ± 13	1602
6A	628 ± 5	
6B	515 ± 20	1762
1S	233 ± 4	749
2S	233 ± 2	

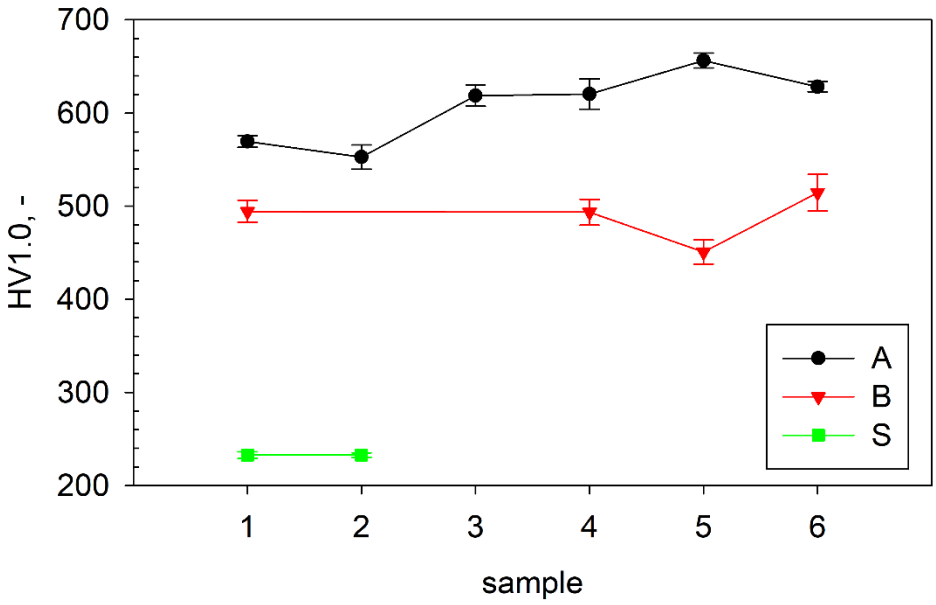

Figure 70: Hardness of the selected samples.

Figure 71 shows the example of stress-elongation curves for the 1B sample for the narrowest area of the specimen (neck) and the area where EBSD maps were obtained. EBSD maps were always taken from the same area (1.3 mm from the final fracture) close to the longitudinal axis at different elongations (0, 150, 300, and 500 μm). The plastic deformation in this area after fracture was approx. 1%. Tensile strength could be deduced

from stress-elongation curves. The highest stress reached was used as the tensile strength value. Small interruptions on the stress-elongation curves are the places where the EBSD maps were obtained. During the measurements, which lasted about 15 minutes, jaw movement was stopped and a slight relaxation took place.

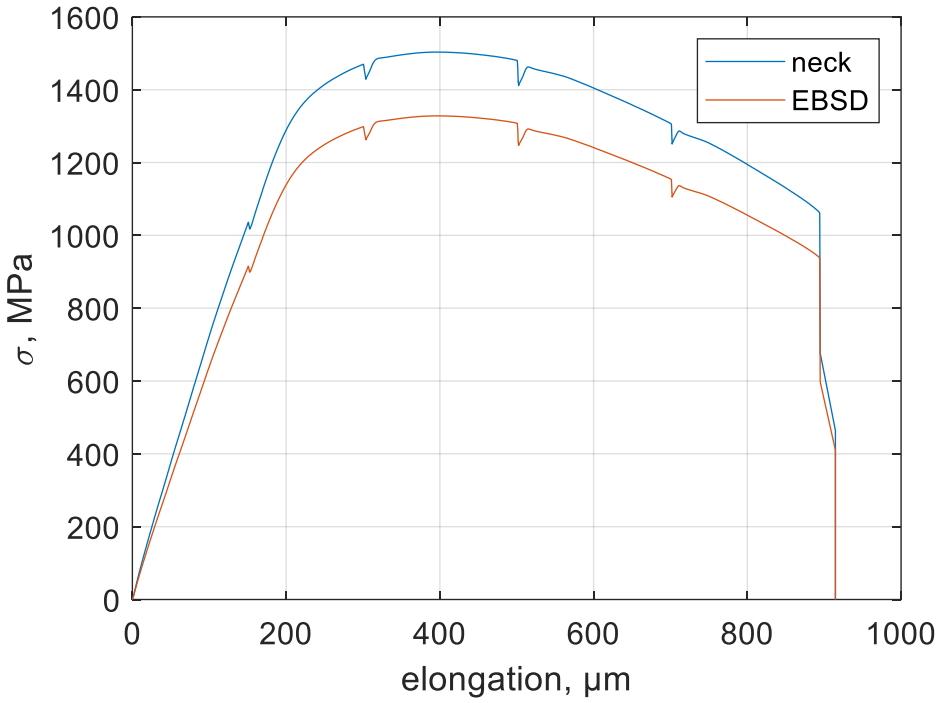

Figure 71: Stress-elongation curves for the narrowest area (neck) and area where EBSD maps were obtained.

Figure 72 compares values of hardness and tensile strength. Based on these results, a clear general correlation between hardness and tensile strength can be found. With higher hardness, higher tensile strength was observed. However, sample 2A had higher tensile strength (200 MPa) than sample 1A, even though they had the same hardness within the margin of error. On the contrary, sample 4A exhibited lower tensile strength (60 MPa) than sample 2A, which was harder by almost 70 HV. Differences between B samples cut out perpendicular (1) or parallel (5, 6) to the cladding were not demonstrated. An average from more samples should be used to evaluate appropriate tensile strength but this is difficult when each sample has a different hardness.

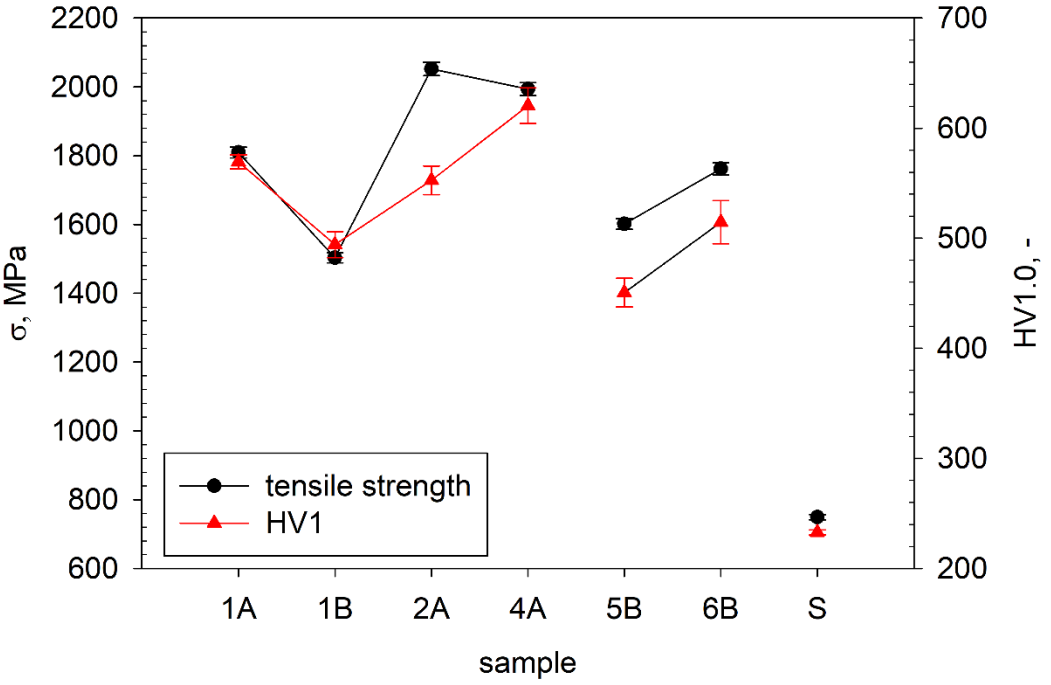

Figure 72: Hardness and tensile strength of the selected samples.

For the in-situ tensile test, sample 1B cut out perpendicular to the cladding direction was used. [001] Inverse pole figures (IPF) of ferritic phase at different displacement values are shown in Figure 73, where individual colours correspond to the normal vectors of crystallographic planes that are parallel to the normal vector of the sample surface. Grain boundaries from angle range 21.06°–47.11° relate mainly to the grain boundaries of the original austenitic grains, which were formed during solidification of the melt, as was already shown for single clad. The original austenite grains with a characteristic size of 20–50 μm were subsequently transformed into martensitic or bainitic laths, see Figure 73. Tensile stress was applied in a direction of 10° from the horizontal direction clockwise. The figure shows the deformation and elongation of the individual grains in the direction of applied stress. White areas in the figure are non-indexed points. With higher deformation, the non-indexed areas increase due to increased roughness of the surface.

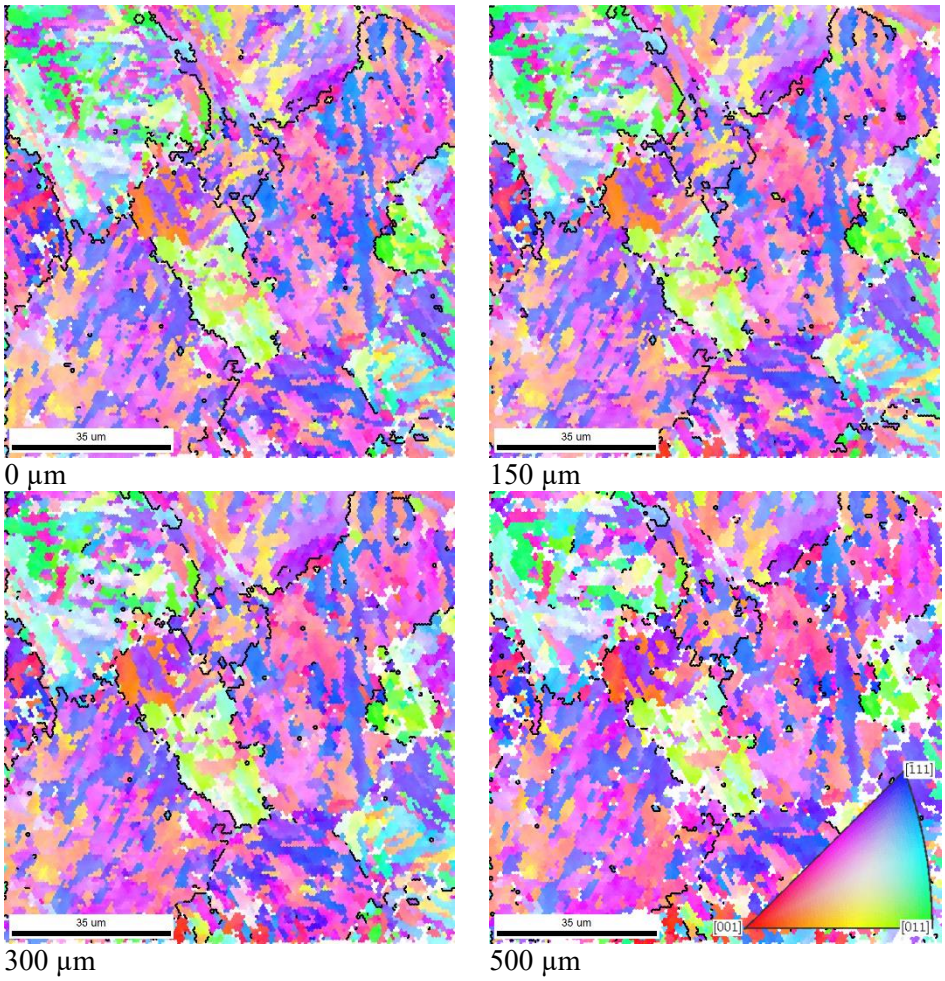

Figure 73: [001] IPF maps of the same sample area corresponding to the specified elongation with highlighted grain boundaries having misorientations between 21.06° and 47.11°.

Maps of Kernel Average Misorientation (KAM) with same highlighted grain boundaries misorientations are shown in Figure 74. KAM value is the average misorientation with respect to closest neighbour of a certain point with a 5° maximum. Higher KAM values could be correlated with a higher concentration of geometrically necessary dislocations [43] [42], and therefore are a measure of local strain. Figure 74 shows the highest KAM values for a non-loaded sample (average KAM value is 1.41° for 0 µm elongation, 1.25° for 150 µm, 1.23° for 300 µm, and 1.20° for 500 µm). This interesting result could be explained by the hypothesis that the map for 0 µm elongation showed local strain due to compressive residual stresses. This stress is gradually removed in tensile testing, therefore the average KAM value decreased. White areas in the figure are non-indexed points. During the tensile test, tensile strain was much more locally concentrated in areas that were not properly indexed in the EBSD experiment, and therefore tensile strain was not properly detected in the EBSD experiment. This

hypothesis was confirmed by the measurement of residual stresses by X-ray diffraction, where tensile residual stress (approx. 260 MPa) was found close to the fracture and compressive stress (approx. –280 MPa) at a greater distance.

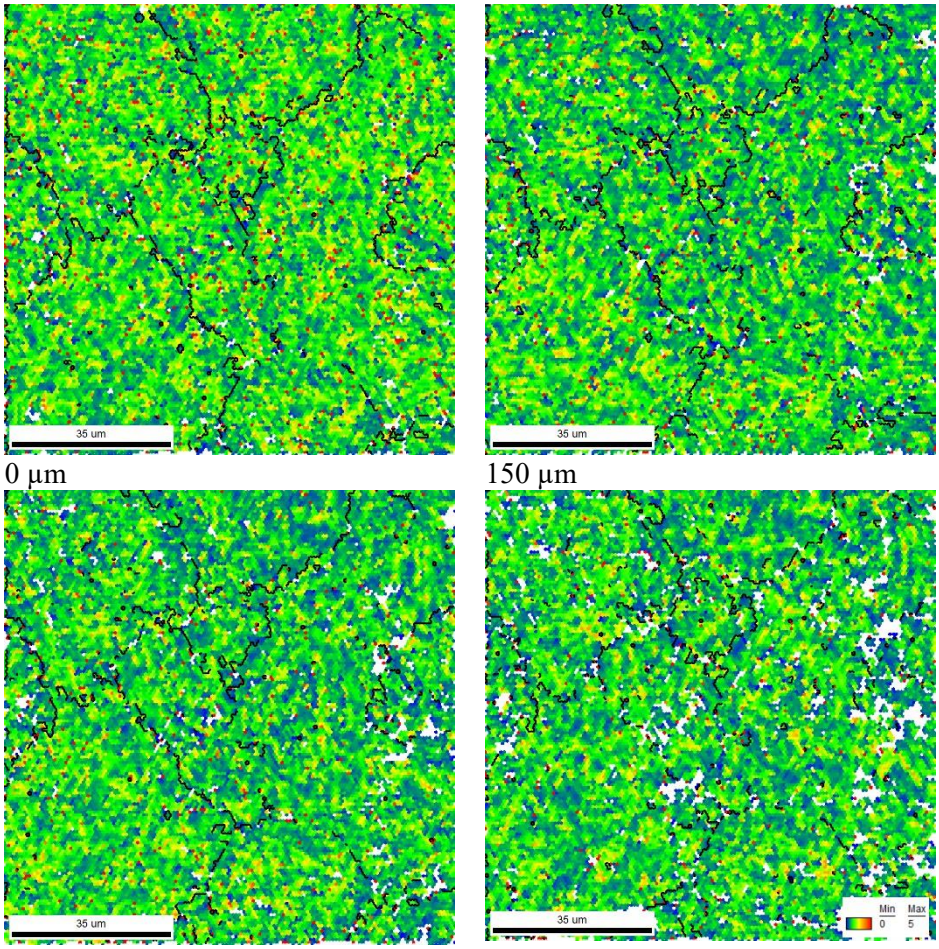

0 µm 150 µm

300 µm 500 µm

Figure 74: KAM maps corresponding to a certain elongation with highlighted grain boundaries having misorientations between 21.06° and 47.11°.

6.3.7 Wear resistance

Figure 75 shows SEM images of pins and disks. Secondary electrons were used to determine the topology while backscattered electrons (BSE) described the change in chemical composition. From the SEM images and Figure 45, where the shape of the worn surface is shown, it can be suggested that the main surface contact is in the centre of the pin and the worn track on the disk. Areas with lower BSE brightness are visible at the edges, indicating the presence of oxides. These oxides act as an abrasive, which results in the formation of depressions at the edges (see Figure 45). The morphology of the worn tracks is similar to that in the literature, see Figure 22.

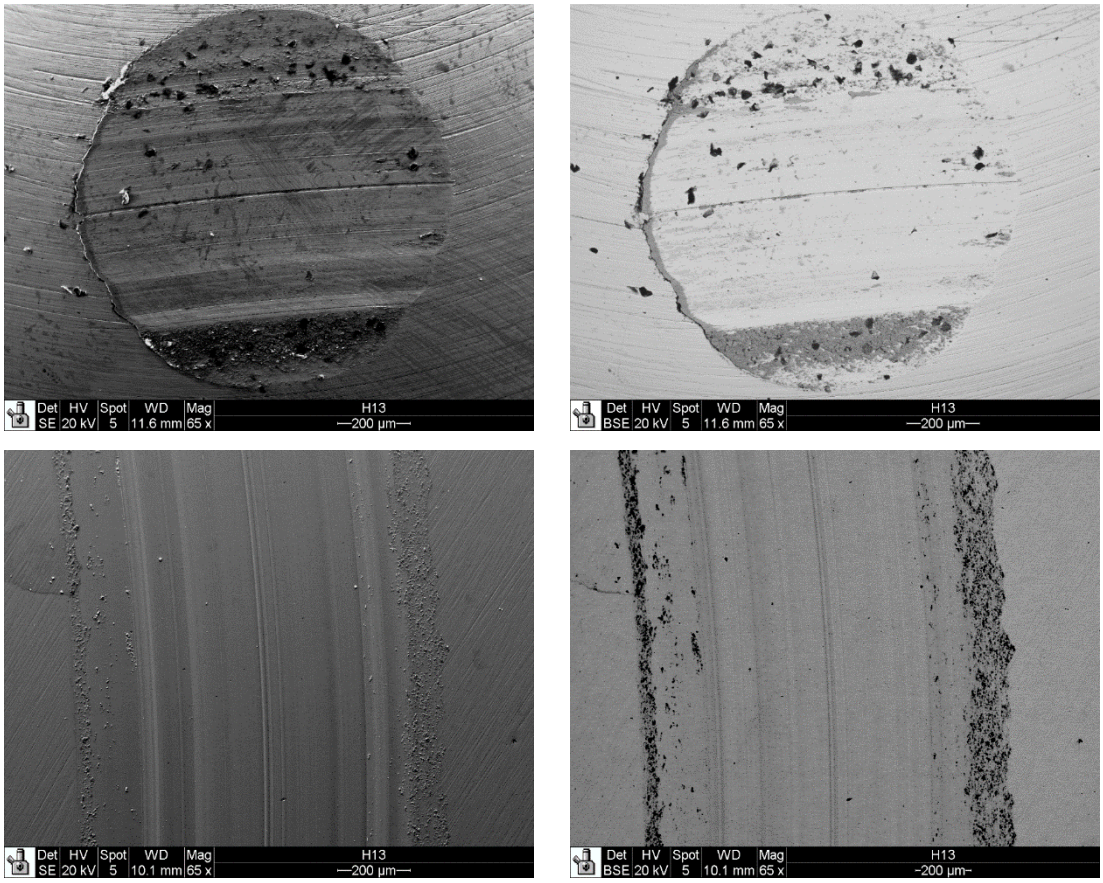

Figure 75: SEM images of pins (top) and disks (bottom), images on the left are obtained from secondary electrons, on the right from backscattered electrons.

Figure 76 to Figure 79 define the wear resistance results. The specific wear rate, see Figure 76, differs by almost an order of magnitude for pins loaded with different forces and different sliding speeds. No dependence on the results is obvious, sometimes further repetition shows a significantly different result. The smallest dispersion shows a higher sliding speed. The disc specific wear rate also shows similar results, see Figure 77. The values also vary by an order, with the dispersion decreasing with higher sliding speed, with the exception of one value. When comparing the disk specific wear rate and the specific wear rate in Figure 78, some linear dependence can be observed, but again certain values show considerable variance.

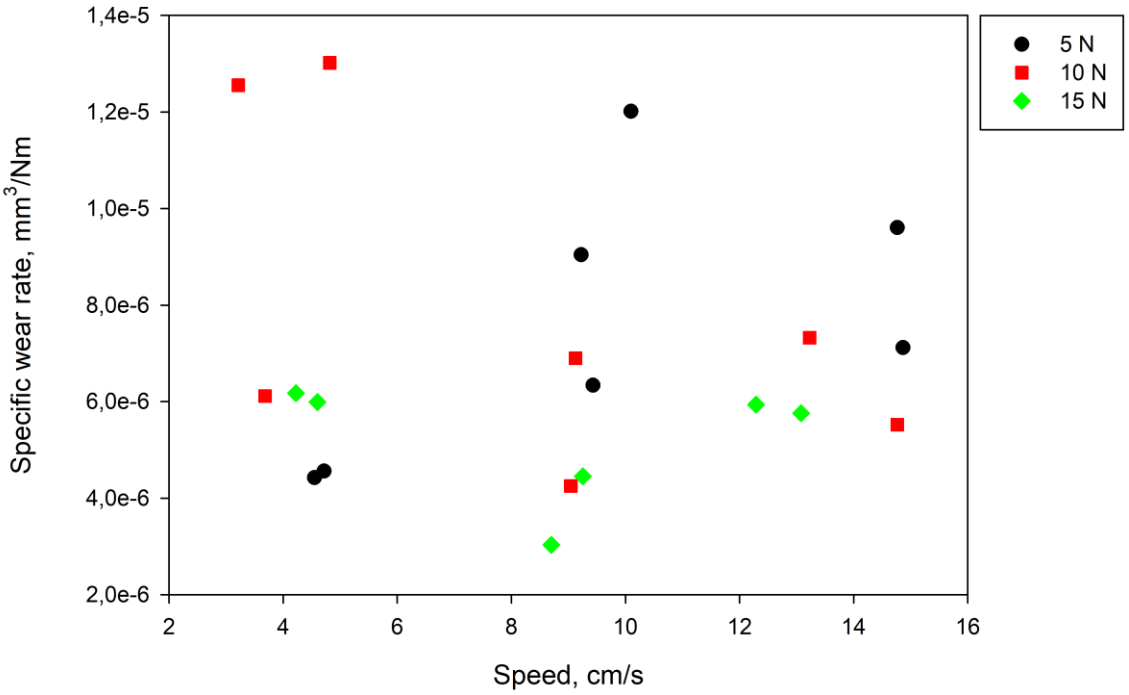

Figure 76: Dependence of specific wear rate for different sliding speeds and loads.

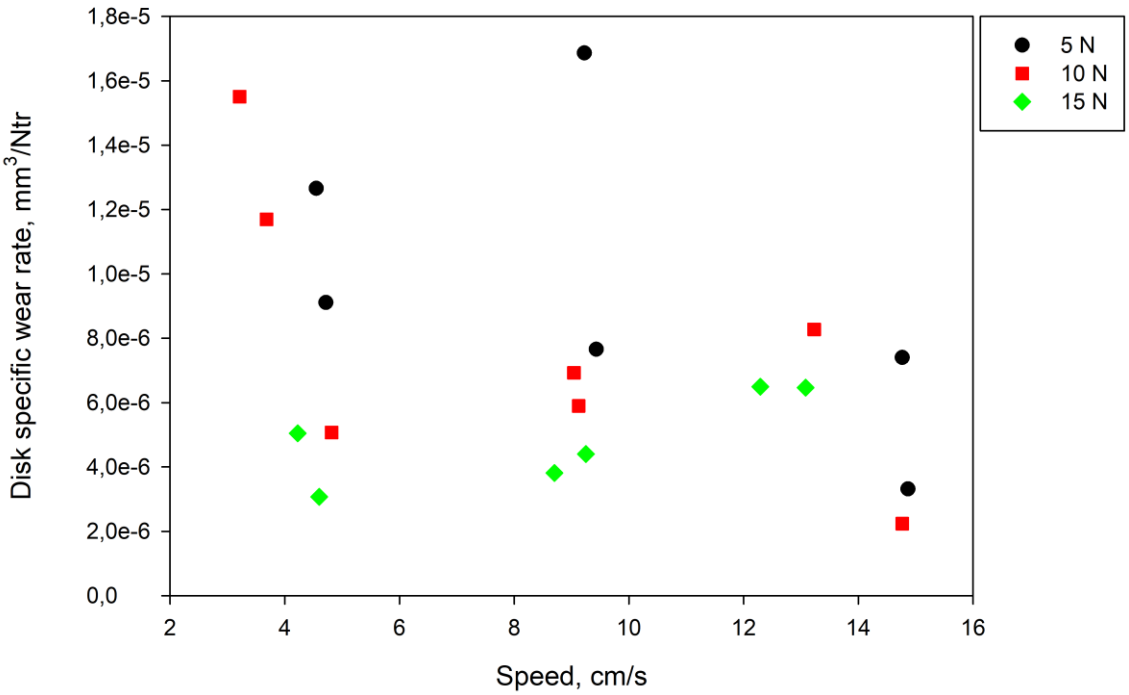

Figure 77: Dependence of disk specific wear rate for different sliding speeds and loads.

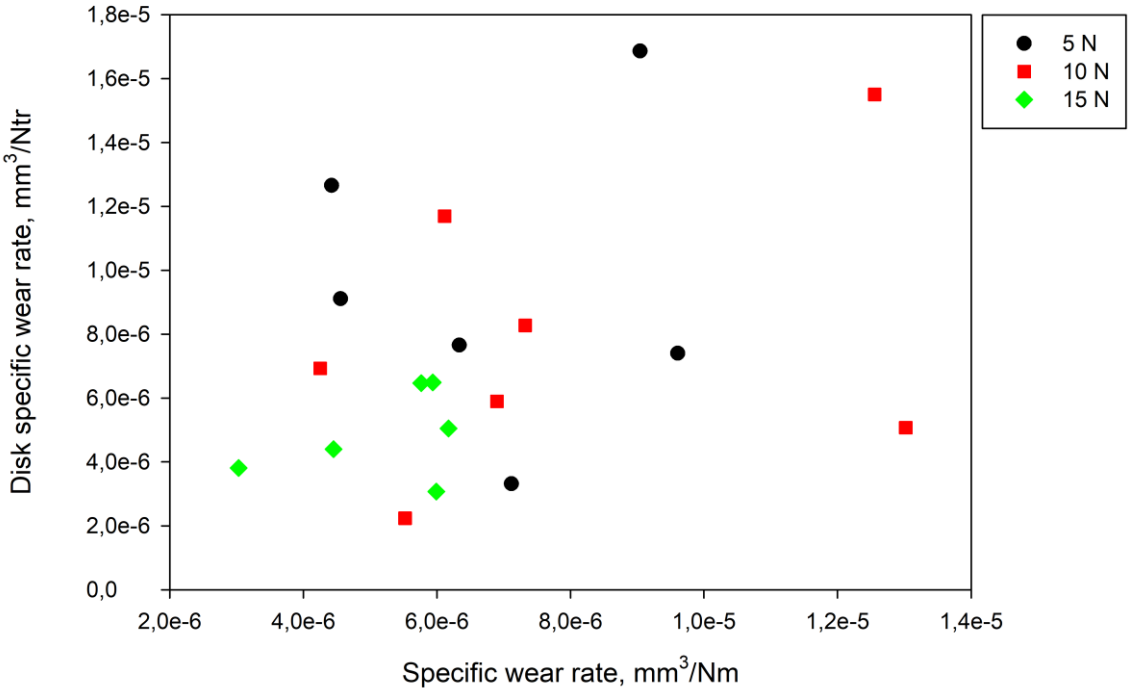

Figure 78: Dependence of disk specific wear rate and specific wear rate.

Figure 79 characterises the dependence of the microhardness of the pins on the specific wear rate. Hardness was obtained from six measurements on the worn surface of the pins. The comparison was made due to the hypothesis that different pin hardness could cause a large variance in wear resistance results within the same sliding speed and load. The correlation between hardness and wear resistance was clear. With increasing hardness, the specific wear rate decreased, which agrees with the conclusions in the available literature [5]. However, it should be realised that increasing hardness also means an increase in the elasticity strain limit and a reduction in ductility, leading to a lowering of fatigue resistance and hence to more brittle failure. For ductile failure, the ratio of hardness to Young's modulus E is a more suitable parameter for predicting wear resistance. This is understandable since the fracture toughness of the clad coatings defined by the 'critical strain–energy release rate' would be improved by both a low E and a high hardness [96]. Thus, it can be stated that in this case the resulting wear resistance of the cladded volume will be significantly affected by the hardness of the functional surface. In turn, the hardness is significantly affected by the cladding process and the temperature reached during the cladding of the following layers.

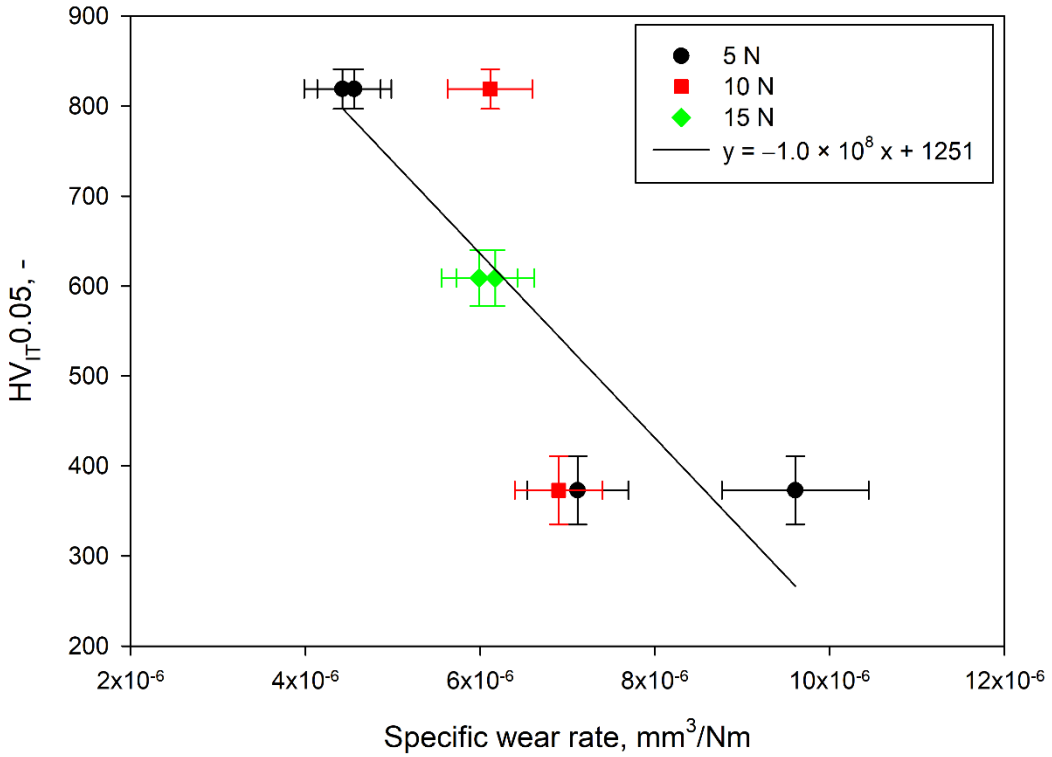

Figure 79: Dependence of specific wear rate and hardness with a linear fit.

6.3.8 Surface finishing

Since laser cladding is less accurate, for example, than the selective laser melting (SLM) process which uses a powder bed, after cladding the material it is always necessary to machine the surface to the required final shape. This chapter describes the real structure, the surface state of residual stress, and the hardness of the ground surface. These values significantly affect the properties of the surface and thus the service life of the repaired part.

The grinding conditions were as follows:

- Machine: Mikronex BRH 20 CNC oscillating surface grinder,
- Grinding wheel: 3M Cubitron™ II 99% 240x15x50,8 99DA54/80 F15VPLF901W,
- Process fluid: Rhenus XY 121 HM in a 3% concentration,
- Cutting speed: 30 m/s,
- Workpiece speed: 15 m/min,
- Step to the side during oscillation: 1 mm,

- Depth of cut per pass: 0.005 mm,
- Total thickness taken: 1.7 mm from the contact,
- Stroke in front and rear dead centre.

6.3.8.1 Real structure

The real structure is described in the following maps, each of which consists of 33 values and the data are linearly interpolated between them. Figure 80 characterizes the phase composition of the ground surface. Only ferrite and retained austenite were characterized on the surface by quantitative phase analysis. The proportion of phase composition and real structure were determined by Rietveld refinement, where Figure 81 denotes the crystallite size, Figure 82 the microdeformation and Figure 83 the dislocation density. The error in calculating the proportion of ferrite is less than 0.1 %, the total error of the phase analysis depends on many factors, but is stated to be approximately 1 to 2 %. The average crystallite size error is 0.8 nm while for microdeformations it is 1.0×10^{-4} and for dislocation density 1.86×10^{14} m^{-2}.

The proportion of ferrite and thus also the proportion of retained austenite varies only by up to 5 wt. %. From the figures it is not possible to observe a certain correlation between the proportion of retained austenite and the size of the crystallites and microdeformation. The left half of the ground surface shows slightly higher values of crystallite size and, conversely, microdeformation and dislocation density is higher to the right. However, the obtained values show a low standard deviation – 1.2 nm and 1.8×10^{-4}, which is almost comparable to the average error. Therefore, in terms of real structure the ground surface appears more homogeneous than the unground surface.

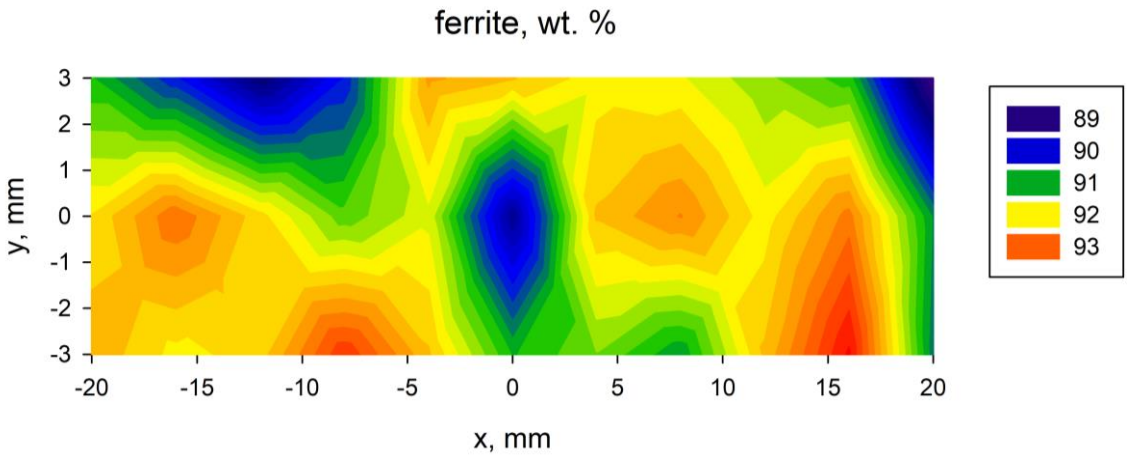

Figure 80: Map of the proportion of ferrite on the ground surface of the clad.

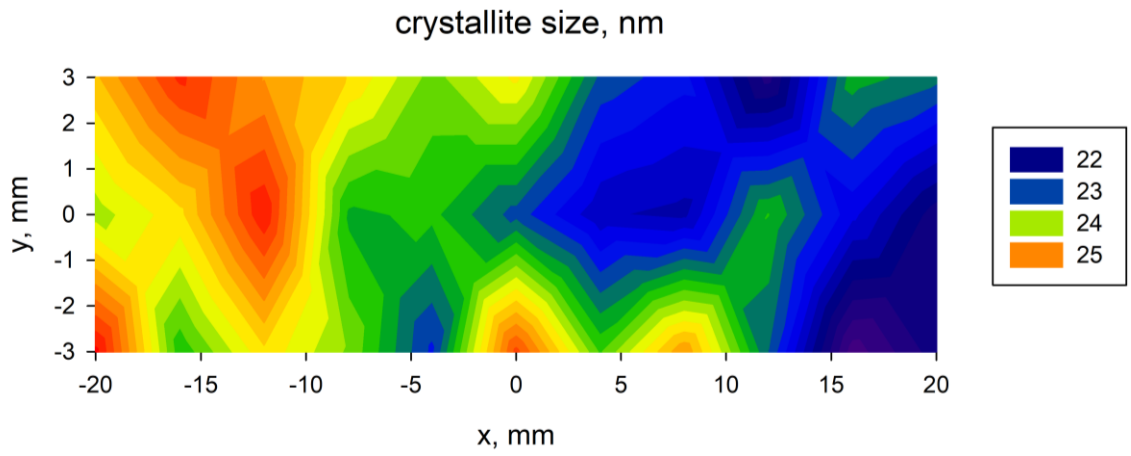

Figure 81: Map of crystallite size of ferrite phase on the ground surface of the clad.

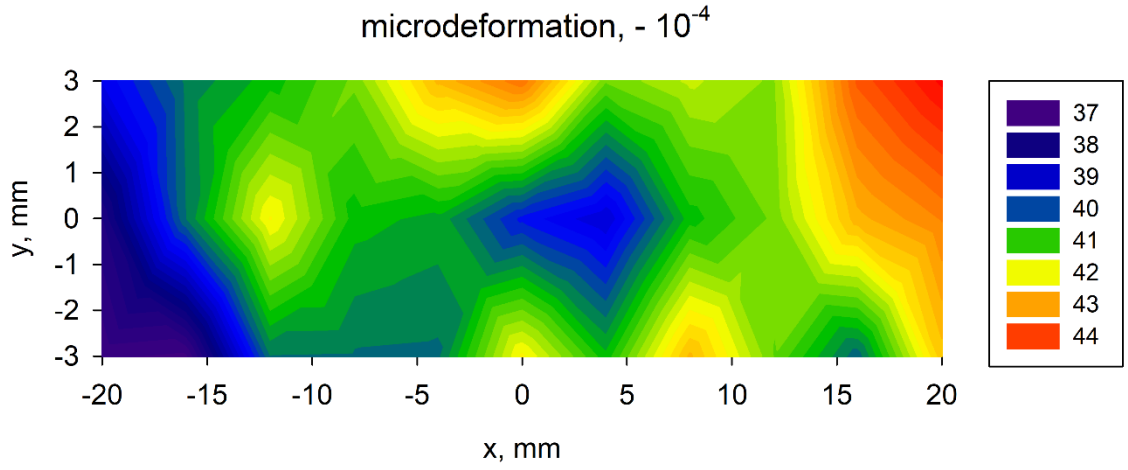

Figure 82: Map of microdeformation of ferrite phase on the ground surface of the clad.

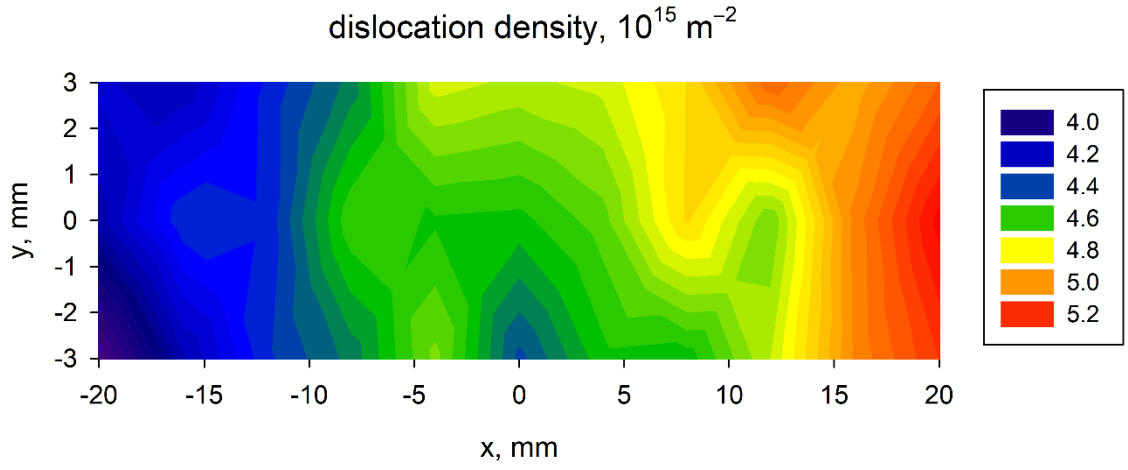

Figure 83: Map of dislocation density of ferrite phase on the ground surface of the clad.

6.3.8.2 Surface residual stress

Figure 84 and Figure 85 characterize the surface macroscopic residual stresses of ground surface in the L direction, i.e. in the cladding and grinding direction, and in the T direction, i.e. perpendicular, respectively. The average error of the residual stress calculation is 26 MPa for both directions.

With respect to the creation of residual stress during grinding, the direction of grinding is unfavourable, i.e. in the direction of the grinding lines (in this case the L direction). The material is strongly plastically deformed in this direction during grinding, which can cause tensile residual stresses, especially if the depth of cut per pass is large. However, only compressive residual stresses were analysed in both directions. In the L direction, as expected, the compressive residual stresses are smaller (–551 MPa with a standard deviation of 28 MPa vs. –867 MPa with a deviation of 34 MPa), but due to the small depth of cut per pass and sufficient cooling, tensile residual stresses did not occur.

From the figures describing the residual stresses of the ground surface, it can be seen that higher values of compressive stresses occur in the right part of the clad for both directions. In the same area, higher microdeformation and smaller crystallite size were determined. This dependence is most likely caused by the cladding process, when the beads from which the clad is made end on the right side. Therefore, a different cooling rate probably occurred at this area.

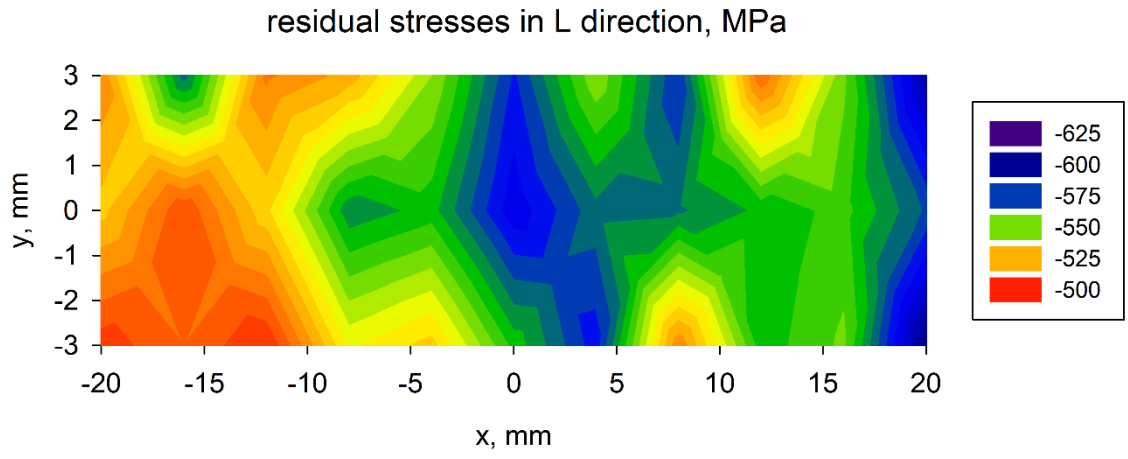

Figure 84: Map of residual stresses on the ground surface of the clad in the L direction.

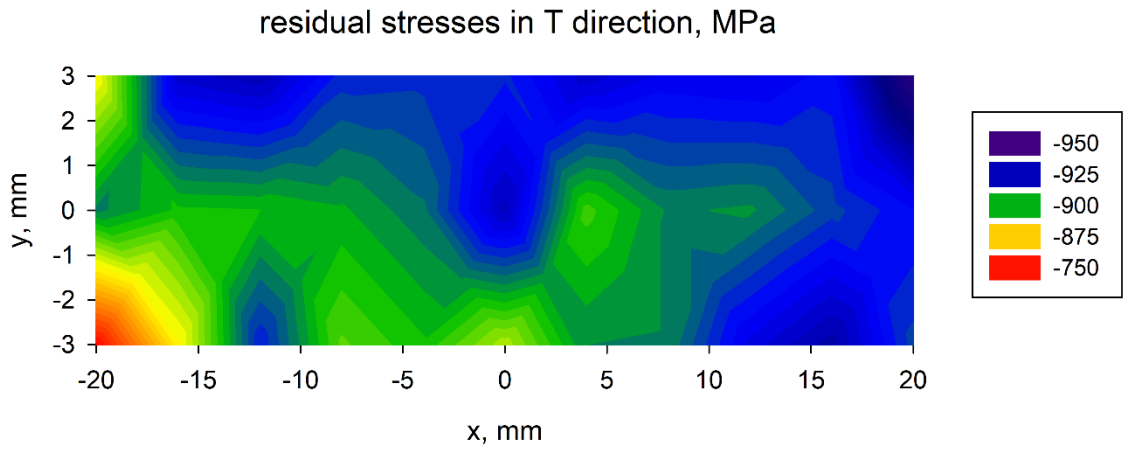

Figure 85: Map of residual stresses on the ground surface of the clad in the T direction.

6.3.8.3 Hardness

Figure 86 defines the hardness $HV_{IT}1.0$ of the ground clad. The average hardness value is 681 $HV_{IT}1.0$ with a standard deviation of 50 $HV_{IT}1.0$. At a distance of approx. x = –15 mm on the upper and lower side of the clad, the hardness reaches only 535 HV. The occurrence of an area with a lower hardness value on the surface of the repaired part is unfavourable in terms of its service life. Based on the previous results, it can be stated that test specimens with lower hardness showed a lower yield strength and, on average, a higher specific wear rate.

It is also clear from the figure that the higher hardness values are in the right side of the clad. Although the differences between microdeformation values and crystallite size are small, it is possible to observe the dependence that higher hardness values are in areas with smaller crystallite size and higher microdeformation. This is due to the concentration of dislocations and boundaries of crystallites, which in turn leads to higher hardness. Yield stress (represented by hardness) increases with increasing dislocation density ρ (following a $\rho^{1/2}$ relationship) and with decreasing grain size d (according to Hall-Petch effect following a $d^{-1/2}$ relationship), since the crystallite size often correlates with grain size. It is important to note that ductile failure during wear, the determining factor is not just yield stress but also toughness following a d^{-1} relationship upon decreasing grain size (the strength of the toughness effect is correlated to the difference in fracture toughness between grain boundary and grain interior toughness) [97]. In the area with higher hardness, the compressive residual stresses also reach higher values in both directions.

When optimizing the parameters of laser cladding, it would be appropriate from the point of view of service life to achieve the parameters that occur in the right side of the clad, where the beads always ended during the cladding process. This fact would be appropriate to investigate in further research using numerical methods.

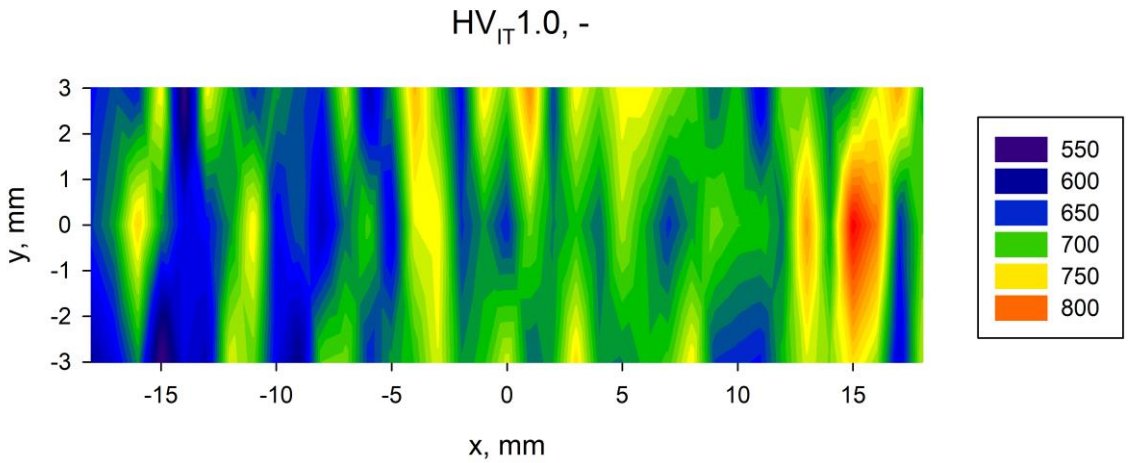

Figure 86: Hardness map of the ground surface of the clad.

6.4 Conclusion

Laser deposition of H13 tool steel showed great application potential. In the first step, the microstructure of the multi-layer clad was described in detail, where it was found that the layers show differences that may lead to undesirable properties. A crack was observed on the surface, its propagation could be supported by tensile surface residual stresses in the T direction. The bulk compressive residual stresses in the T direction were characterized only at the transition between the clad and the base material.

Further, a different ferritic structure was described in the second layer. It was confirmed that this area had a significantly lower hardness by about 200 HV. The decrease in hardness corresponds to annealing at a temperature of approximately 600°C. The higher annealing temperature was also reflected in the phase composition, when in the area with lower hardness there was a decrease in retained austenite. From this it can be concluded that the strategy of cladding process and temperature control can significantly affect the resulting material properties. The phase composition and the real structure on the surface of the clad showed greater inhomogeneities, from which it can be concluded that the cladding process and especially the rate of cooling of the material is not the same in all areas. This information must be taken into account when further optimizing the process. Moreover, it was shown that the average tensile strength of the cladded volume is 1787 ± 195 MPa. According to observation, the higher standard error value of tensile strength is due to differences in hardness of the sample. Deformation and rotation of individual grains during tensile test was observed by EBSD.

It is very important that areas with lower hardness did not reach a large part of the surface during machining, as it has been demonstrated that samples with lower hardness can exhibit significantly worse wear resistance. The ground surface showed compressive residual stresses in both directions, which are convenient from the point of view of component life. Even the real structure did not indicate large differences within the analysed ground surface. However, greater variance was observed for hardness, where the difference between the highest and lowest value is 300 HV. Future research needs to devote attention to describing the formation of areas with lower hardness.

7 Summary and future research plan

The objectives of the work were met in full, the research was able to describe in detail the effect of laser cladding on the real structure of AISI H13 tool steel. The knowledge obtained from the experiments can be summarised in the following bullet points:

- Laser deposition of H13 tool steel showed great application potential, as it was possible to create clads without internal defects;
- For single bead cladding, tensile RS was detected in the transversal direction, therefore, phase transformation and not shrinkage is likely to be the dominant effect;
- By tempering, residual stresses declined, nevertheless, tempering does not seem to be needed after cladding;
- It was found that the multi-layered clad showed differences in microstructure across the thickness that may lead to undesirable properties;
- Martensitic structure predominated, but a mostly ferritic structure was observed in the second cladded layer. It was confirmed that this area had a significantly lower hardness by about 200 HV. The decrease in hardness corresponded to annealing to a temperature of approximately 600 °C;
- The majority of alloying elements in the clad were not in the form of carbides. Carbides were confirmed only in areas with a ferritic structure;
- A crack was observed on the surface of the clad, the propagation of which could be supported by tensile surface residual stresses in the direction transverse to cladding. The bulk compressive residual stresses in the T direction were characterised only at the interface between the clad and the base material;
- Surface residual stresses reached mainly compressive values in the L direction; only at the edges were there areas with tensile stresses. However, unfavourable bulk tensile stresses were determined using neutron diffraction in the clad in the L direction;
- The resulting wear resistance of the cladded volume was significantly affected by the hardness of the functional surface. In turn, it was shown that the hardness was significantly affected by the cladding process and also by the temperature reached during the cladding of the subsequent layers;

- The outer surface layer, which showed tensile surface residual stresses and cracks, was removed by grinding. Furthermore, surface compressive residual stresses were described in both directions on the ground surface, which is convenient from the perspective of component service life.

Interesting data were obtained that were able to answer several questions, but some parts of the research are still awaiting clarification. Therefore, the experience gained should be applied in follow-up research and in cooperation with industry. In particular, the different microstructure, hardness and real structure within the cladded volume need to be further investigated and the reasons for their occurrence clarified.

To this end, a computational finite element method could be used as a suitable tool to answer many questions following calibration with real experimental data. This numerical model would propose an optimal cladding strategy to reduce areas with unsuitable mechanical properties and real structure, especially in complex samples, where heat dissipation and thus cooling rate will be very uneven.

It seems appropriate to pursue the scheme proposed below with other research and industrial partners in a joint application project.

1) Problem analysis, selection of suitable cladding technology and powders for select applications.
2) Finding process parameters for cladding without internal defects.
3) Study of mechanical properties, microstructure, phase composition, and residual stresses of newly cladded volume in laboratory samples. Study of the transition area and inhomogeneity within the volume. Machining of the clad into the final shape, testing of the newly created surface.
4) Optimization of process parameters and print layout based on previous results.
5) Preparation of a numerical model for cladding modelling and calibration using experimental values.
6) Verification of numerical models, mechanical properties, and fatigue life of complex machine parts.
7) Real application of laser cladding by an industrial partner using a cladding strategy according to a numerical model.

References

[1] Steen, W. M. Laser material processing. 3rd ed. London: Springer, 2003. ISBN 1-85233-698-6.

[2] Kužel, R. Real structure of polycrystalline materials - Short course. Materials Structure in Chemistry, Biology, Physics and Technology. 2009, Vol. 16, 2a.

[3] Čapek, J., Trojan, K., Kec, J., Černý, I., Ganev, N., Němeček, S. On the Weldability of Thick P355NL1 Pressure Vessel Steel Plates Using Laser Welding. Materials. 2020, Vol. 14, 1.

[4] Vedani, M., Previtali, B., Vimercati, G. M., Sanvito, A., Somaschini, G. Problems in laser repair-welding a surface-treated tool steel. Surface & Coatings Technology. 2007, Vol. 201, 8, pp. 4518–4525.

[5] Telasang, G., Majumdar, D. J., Wasekar, N., Padmanabham, G., Manna, I. Microstructure and Mechanical Properties of Laser Clad and Post-cladding Tempered AISI H13 Tool Steel. Metallurgical and Materials Transactions A. 2015, Vol. 46, 5, pp. 2309–2321.

[6] Shinde, M. S., Ashtankar, K. M. Additive manufacturing–assisted conformal cooling channels in mold manufacturing processes. Advances in mechanical engineering. 2017, Vol. 9, 5, pp. 1–14.

[7] Čapek, J., Černý, I., Trojan, K., Ganev, N., Kec, J., Němeček, S. Investigation of residual stresses in high cycle loaded laser steel welds. Experimental Stress Analysis - 57th International Scientific Conference, EAN 2019 - Conference Proceedings. 2019, pp. 24–29.

[8] Schwingenschlögl, P., Niederhofer, P., Merklein, M. Investigation on basic friction and wear mechanisms within hot stamping considering the influence of tool steel and hardness. Wear. 2019, Vols. 426–427, A, pp. 378–389.

[9] Liu, J., To, A. C. Topology optimization for hybrid additive-subtractive manufacturing. Structural and Multidisciplinary Optimization. 2017, Vol. 55, pp. 1281–1299.

[10] Kraus, I., Fiala, J. Elementární fyzika pevných látek. Praha: ČVUT, 2011. ISBN 978-80-01-04931-0.

[11] Ion, J. C. Laser Processing of Engineering Materials: Principles, procedure and industrial application. Oxford: Butterworth Heinemann, 2005. ISBN 0-7506-6079-1.

[12] Quimby, R. S. Photonics and lasers: an introduction. Hoboken: Wiley-Interscience, 2006. ISBN 0-471-71974-9.

[13] Thyagarajan, K., Ghatak, A. K. Lasers: theory and applications. New York: Plenum Press, 1981. ISBN 0-306-40598-9.

[14] Csele, M. Fundamentals of light sources and lasers [electronic source]. Hoboken: Wiley, 2004. ISBN 9780471675211.

[15] Silfvast, W. T. Laser fundamentals. Cambridge: Cambridge University Press, 1996. ISBN 0-521-55617-1.

[16] O'Sullivan, M. S., Hui, R. Fiber optic measurement techniques. Burlington: Academic Press, 2009. ISBN 978-0-12-373865-3.

[17] Peterka, P., Honzátko, P., Kašík, I. Vláknové lasery: nový nástroj pro průmysl a medicínu. Československý časopis pro fyziku. 2015, Vol. 65, pp. 389–394.

[18] Ocelík, V., De Hosson, J. T. M. Thick metallic coatings by coaxial and side laser cladding: Processing and properties. [book auth.] P. Schaaf. Advances in Laser Materials Processing Technology. West Palm Beach: CRC Press, 2010, pp. 426–458.

[19] Laserline. Laser Cladding. [Online] Laserline GmbH. [Cited: 1 June 2020.] https://www.laserline.com/en-int/laser-cladding/.

[20] Jeníček, L., Ryš, P., Cenek, M. Nauka o materiálu I. Praha: Academia, 1966. ISBN 21-081-66.

[21] Kraus, I. Struktura a vlastnosti krystalů. 1. Vyd. Praha: Academia, 1993. ISBN 80-200-0372-X.

[22] Kraus, I., Ganev, N. Difrakční analýza mechanických napětí. Praha: ČVUT, 1995. ISBN 80-01-01366-9.

[23] Machek, V., Sodomka, J. Struktury kovových materiálů. 1. část, [Nauka o materiálu]. Praha: ČVUT v Praze, 2006. ISBN 80-01-03379-1.

[24] Bhadeshia, H., Honeycombe, R. Steels: Microstructure and Properties. 3. Cambridge: Butterworth Heinemann, 2006. ISBN 978-0-7506-8084-4.

[25] Vojtěch, D. Kovové materiály. Praha: Vydavatelství VŠCHT Praha, 2006. ISBN 80-7080-600-1.

[26] Kraus, I. Úvod do strukturní rentgenografie. 1. Vyd. Praha: Academia, 1985.

[27] Kraus, I., Ganev, N. Technické aplikace difrakční analýzy. Vyd. 1. Praha: Vydavatelství ČVUT, 2004. ISBN 80-01-03099-7.

[28] Von Dreele, R. B. Powder diffration peak profiles. [book auth.] Gilmore, C. J., Kaduk, J. A. and H. Schenk. International Tables for Crystallography, Volume H, Powder Diffraction. Hoboken: Wiley, 2019, pp. 263–269.

[29] Valvoda, V., Polvarová, M., Lukáč, P. Základy strukturní analýzy. Praha: Univerzita Karlova, 1992. ISBN 80-200-0280-4.

[30] Pecharsky, V. K., Zavalij, P. Y. Fundamentals of powder diffraction and structural characterization of materials. Second Edition. New York: Springer, 2009. ISBN 978-0-387-09578-3.

[31] Čapek, J. Difrakční analýza mřížkových deformací polykrystalických materiálů s přednostní orientací: doctoral thesis. Praha: České vysoké učení technické v Praze, Fakulta jaderná a fyzikálně inženýrská, Katedra inženýrství pevných látek, 2018.

[32] Guinebretière, R. X-ray Diffraction by Polycrystalline Materials. London: ISTE, 2007. ISBN 978-1-905209-21-7.

[33] Klug, H. P., Alexander, L. E. X-Ray Diffraction Procedures For Polycrystalline and Amorphous Materials. New York: Wiley, 1974. ISBN 0-471-49369-4.

[34] Gnaupel-Herold, T., Mikula, P., Paranjpe, S. K., Schneider, R., Teixeira, J., Torok, G., Youtsos, A. G. Measurement of residual stress in materials using neutrons. Proceedings of IAEA Technical Meeting, IAEA-TECDOC. 2003, Vol. 1457.

[35] Withers, P. J., Preuss, M., Steuwer, A., Pang, J. W. L. Methods for obtaining the strain-free lattice parameter when using diffraction to determine residual stress. Journal of applied crystallography. 2007, Vol. 40, 5, pp. 891–904.

[36] Karlík, M. Úvod do transmisní elektronové mikroskopie. Praha: ČVUT v Praze, 2011. ISBN 978-80-01-04729-3.

[37] JEOL Co. Ltd.. Invitation to the SEM World: For People who are Using the SEM for the First Time, user manual. 2004.

[38] Chauhan, A. Deformation and damage mechanisms of ODS steels under high-temperature cyclic loading. 2018.

[39] Wilkinson, A. J., Britton, T. B. Strains, planes, and EBSD in materials science. Materials Today. 2012, Vol. 15, 9, pp. 366–376.

[40] Zaefferer, S. Some Ideas on the Formation Mechanisms and Intensity Distribution of Backscatter Kikuchi Patterns. Microscopy and Microanalysis. 2007, Vol. 13, S02, pp. 928–929.

[41] Max-Planck-Institut für Eisenforschung. Electron backscatter diffraction - EBSD. [Online] [Cited: 1 June 2020.] https://www.mpie.de/3077954/EBSD.

[42] TSL, TexSEM Laboratories. Orientation Imaging Microscopy (OIM) software version 7.3.0, user manual. 2015.

[43] Mikami, Y., Oda, K., Kamaya, M., Mochizuki, M. Effect of reference point selection on microscopic stress measurement using EBSD. Materials Science and Engineering. A, 2015, Vol. 647, pp. 256–264.

[44] Wright, S. I., Nowell, M. M. EBSD image quality mapping. Microscopy and microanalysis. 2006, Vol. 12, 1, pp. 72–84.

[45] Microscopy Australia. X-ray intensity. MyScope. [Online] 12 June 2014. [Cited: 1 June 2020.] https://myscope.training/legacy/analysis/eds/xrayintensity/.

[46] Macek, K., Zuna, P. Nauka o materiálu. Praha: ČVUT v Praze, 1996. ISBN 80-01-01507-6.

[47] Fiala, J., Mentl, V., Šutta, P. Struktura a vlastnosti materiálu. Praha: Academia, 2003. ISBN 80-200-1223-0.

[48] Lucca, D. A, Herrmann, K., Klopfstein, M. J. Nanoindentation: Measuring methods and applications. CIRP Annals. 2010, Vol. 59, 2, pp. 803–819.

[49] Oliver, W., Pharr, G. An improved technique for determining hardness and elastic modulus using load and displacement sensing indentation experiments. Journal of Materials Research. 1992, Vol. 7, 6, pp. 1564–1583.

[50] Anton Paar. Instrumented indentation testing (IIT). Anton Paar Wiki. [Online] Anton Paar. [Cited: 25 May 2020.] https://wiki.anton-paar.com/en/instrumented-indentation-testing-iit/.

[51] Tribonet. Pin on Disk Test. [Online] 24. February 2019. [Citace: 1. June 2020.] https://www.tribonet.org/wiki/pin-on-disk-test/.

[52] Godse, R. S., Gawande, S. H. and Keste, A. A. Tribological Behavior of High Fraction Carbon Steel Alloys. Journal of Bio- and Tribo-Corrosion. 2016, Vol. 2, 3.

[53] Ross, B. R. LSS H13 tool steel. [Online] January 2007. [Cited: 2019 June 1.] http://www.latrobesteel.com.

[54] BOHLER-UDDEHOLM CORPORATION. Bohler-Uddeholm H13 TOOL STEEL. [Online] July 2013. [Cited: 1 June 2019.] https://www.voestalpine.com/highperformancemetals/usa/en/products-brands/tool-steel/.

[55] Standard A 681 - 08. ASTM International, 2015.

[56] EN ISO 4957:1999 Tool steels. Brussels: European committee for standardization, 1999.

[57] UDDEHOLMS AB. UDDEHOLM ORVAR SUPREME. [Online] September 2013. [Cited: 1 June 2019.]

[58] Gupta, K. Advanced manufacturing technologies. Springer, 2017. ISSN 2195-092X.

[59] Wołosz, P., Baran, A., Polański, M. The Influence of Laser Engineered Net Shaping (LENS™) Technological Parameters on the Laser Deposition Efficiency and Properties of H13 (AISI) Steel. Journal of Alloys and Compounds. 2020, Vol. 823, 153840.

[60] He, X., Yu, G., Mazumder, J. Temperature and composition profile during double-track laser cladding of H13 tool steel. Journal of Physics D: Applied Physics. 2009, Vol. 43, 1.

[61] Candel, J. J., Amigó, V., Ramos, J. A., Busquets, D. Problems in laser repair cladding a surface AISI D2 heat-treated tool steel. Welding International. 2013, Vol. 27, 1, pp. 10–17.

[62] Paul, S., Thool, K., Singh, R., Samajdar, I., Yan, W. Experimental characterization of clad microstructure and its correlation with residual stresses. Procedia Manufacturing. 2017, pp. 804–818.

[63] Chen, C., Yan, K., Qin, L., Zhang, M., Wang, X., Zou, T., Hu, Z. Effect of heat treatment on microstructure and mechanical properties of laser additively manufactured AISI H13 tool steel. Journal of Materials Engineering and Performance. 2017, Vol. 26, 11, pp. 5577–5589.

[64] Wang, S., Chen, J. and Xue, L. Characteristics of H13 Tool Steel Coatings by Pulsed Nd: YAG Laser Cladding. 2013. TMS 2013 142nd Annual Meeting and Exhibition, Annual Meeting. pp. 201–208.

[65] Ferreira, D. F., Vieira, J. S., Rodrigues, S. P., Miranda, G., Oliveira, F. J., Oliveira, J. M. Dry sliding wear and mechanical behaviour of selective laser

melting processed 18Ni300 and H13 steels for moulds. Wear. 2022, Vol. 488, 204179.

[66] Telasang, G., Majumdar, J. D., Padmanabham, G., Tak, M., Manna, I. Effect of laser parameters on microstructure and hardness of laser clad and tempered AISI H13 tool steel. Surface and Coatings Technology. 2014, Vol. 258, pp. 1108–1118.

[67] Zhang, Y., Xianghua, Z. and Xiangkai, Y. Eliminating cladding cracks: pre-heating and stress analysis. Laser Institute of America, 2001. Vol. 1, pp. 577–587.

[68] Paul, S., Ashraf, K., Singh, R. Residual stress modeling of powder injection laser surface cladding for die repair applications. ASME 2014 International Manufacturing Science and Engineering Conference collocated with the JSME 2014 International Conference on Materials and Processing and the 42nd North American Manufacturing Research Conference. 2014.

[69] Kattire, P., Paul, S., Singh, R., Yan, W. Experimental characterization of laser cladding of CPM 9V on H13 tool steel for die repair applications. Journal of Manufacturing Processes. 2015, Vol. 20, pp. 492–499.

[70] Cottam, R., Wang, J., Luzin, V. Characterization of microstructure and residual stress in a 3D H13 tool steel component produced by additive manufacturing. Journal of Materials Research. 2014, Vol. 29, 17, pp. 1978–1986.

[71] Bailey, N. S, Katinas, C., Shin, Y. C. Laser direct deposition of AISI H13 tool steel powder with numerical modeling of solid phase transformation, hardness, and residual stresses. Journal of Materials Processing Technology. 2017, Vol. 247, pp. 223–233.

[72] Chen, J., Wang, S., Xue, L. On the development of microstructures and residual stresses during laser cladding and post-heat treatments. Journal of Materials Science. 2012, Vol. 47, 2, pp. 779–792.

[73] Nie, Z., Wang, G., McGuffin-Cawley, J. D., Narayanan, B., Zhang, S., Schwam, D., Kottman, M., Rong, Y. K. Experimental study and modeling of H13 steel deposition using laser hot-wire additive manufacturing. Journal of Materials Processing Technology. 2016, Vol. 235, pp. 171–186.

[74] Santhanakrishnan, S., Kong, F., Kovacevic, R. An experimentally based thermo-kinetic hardening model for high power direct diode laser cladding. Journal of Materials Processing Technology. 2011, Vol. 211, 7, pp. 1247–1259.

[75] Zhao, X., Lv, Y., Dong, S., Yan, S., He, P., Liu, X., Liu, Y., Lin, T., Xu, B. The effect of thermal cycling on direct laser-deposited gradient H13 tool steel: Microstructure evolution, nanoprecipitation behaviour, and mechanical properties. Materials Today Communications. 2020, Vol. 25, 101390.

[76] Zhu, L., Wang, S., Pan, H., Yuan, C., Chen, X. Research on remanufacturing strategy for 45 steel gear using H13 steel powder based on laser cladding technology. Journal of Manufacturing Processes. 49, 2020, pp. 344–354.

[77] Haldar, B., Saha, P. Identifying defects and problems in laser cladding and suggestions of some remedies for the same. Materials Today: Proceedings. 2018, Vol. 5, 5, pp. 13090–13101.

[78] Köhler, H., Partes, K., Kornmeier, J. R., Vollertsen, F. Residual Stresses in Steel Specimens Induced by Laser Cladding and their Effect on Fatigue Strength. Physics Procedia. 2012, Vol. 39, pp. 354–361.

[79] Salonitis, K., D'Alvise, L., Schoinochoritis, B. Additive manufacturing and post-processing simulation: laser cladding followed by high speed machining. The International Journal of Advanced Manufacturing Technology. 2015, Vol. 85, pp. 2401–2411.

[80] Totten, G. E., Howes, M., Inoue, T. Handbook of residual stress and deformation of steel. 1. Materials Park: ASM International, 2002. ISBN 9780871707291.

[81] Lee, S. J., Lee, Y. M., Du, M. F. The polishing mechanism of electrochemical mechanical polishing technology. Journal of Materials Processing Technology. 2003, Vol. 140, 1–3, pp. 280–286.

[82] Andrews, K. W. Empirical Formulae for the Calculation of Some Transformation Temperatures. Journal of the Iron and Steel Institute. 1965, Vol. 203, pp. 721–727.

[83] Krauss, G. Steels: Processing, Structure, and Performance. Materials Park: ASM International, 2005. ISBN 0871708175.

[84] Klobčar, D., Tušek, J., Taljat, B. Thermal fatigue of materials for die-casting tooling. Materials Science & Engineering A. 2008, Vol. 472, 1, pp. 198–207.

[85] Li, Ch., Yu, Z. B., Gao, J. X., Zhao, J. Y., Han, X. Numerical simulation and experimental study on the evolution of multi-field coupling in laser cladding process by disk lasers. Weld World. 2019, Vol. 63, pp. 925–945.

[86] Kitahara, H., Ueji, R., Tsuji, N., Minamino, Y. Crystallographic features of lath martensite in low-carbon steel. Acta Materialia. 2006, Vol. 54, 5, pp. 1279–1288.

[87] Oliver, W. C., Pharr, G. M. Measurement of hardness and elastic modulus by instrumented indentation: Advances in under-standing and refinements to methodology. Journal of Materials Research. 2004, Vol. 19, pp. 3–20.

[88] ISO 14577. Metallic Materials—Instrumented Indentation Test for Hardness and Material Parameters. Geneva, Switzerland: ISO, 2002.

[89] Matěj, Z., Kužel, R. MStruct - software/library for MicroStructure analysis by powder diffraction. [Online] X-ray group, School of Physics, Charles University in Prague; Scientific software, MAX IV Laboratory, Lund University, 15 June 2018. [Cited: 10 October 2020.] http://www.xray.cz/mstruct/.

[90] Murray, C. E., Noyan, I.C. Applied and residual stress determination using X-ray diffraction. [book auth.] Schajer, G. S. Practical Residual Stress Measurement Methods. Chichester: John Wiley & Sons, 2013, pp. 139–161.

[91] Mikula, P., Vrana, M. High-resolution neutron diffraction for phase and residual stress investigations. In Fracture of Nano and Engineering Materials and Structures. [book auth.] Gdoutos., E. E. Fracture of Nano and Engineering Materials and Structures. Dordrecht: Springer, 2006.

[92] Randau, C., Garbe, U., Brokmeier, H. G. StressTextureCalculator: A software tool to extract texture, strain and microstructure information from area-detector measurements. Journal of Applied Crystallography. 2011, Vol. 44, pp. 641–646.

[93] Wern, H., Johannes, R., Walz, H. Dependence of the X-ray elastic constants on the diffraction plane. Physica Status Solidi. 1998, Vol. 206, pp. 545–557.

[94] Smith, D. K. Crystallite statistics and accuracy in powder diffraction. [book auth.] Snyder, R. L., Fiala, J., Bunge, H. J. Defect and Microstructure Analysis by Diffraction. New York: Oxford University Press, 1999, pp. 333–345.

[95] Roberts, G., Krauss, G., Kennedy, R. Tool Steels. Materials Park: ASM International, 1998. ISBN 0871705990.

[96] Dao, M., Lu, L., Asaro, R. J., De Hosson, J. T. M., Ma, E. Toward a quantitative understanding of mechanical behavior of nano-crystalline metals. Acta Materialia. 2007, Vol. 55, pp. 4041–4065.

[97] Fan, Z. The grain size dependence of ductile fracture toughness of polycrystalline metals and alloys. Materials Science and Engineering: A. 1995, Vol. 171, pp. 73–83.

Author's list of publications

Publications in impact journals

[1] Trojan, K., Ocelík, V., Čapek, J., Čech, J., Canelo-Yubero, D., Ganev, N., Kolařík, K., De Hosson, J.T.M. Microstructure and Mechanical Properties of Laser Additive Manufactured H13 Tool Steel. Metals. 2022, Vol. 12, 243. DOI:10.3390/met12020243.

[2] Čapek, J., Trojan, K., Kec, J., Černý, I., Ganev, N., Němeček, S. On the Weldability of Thick P355NL1 Pressure Vessel Steel Plates Using Laser Welding. Materials. 2021, Vol. 14, 131. DOI:10.3390/ma14010131.

[3] Schmidová, E., Neslušan, M., Ondruš, J., Trojan, K., Pitoňák, M., Klejch, F., Ramesha, S. K. Monitoring of Plastic Straining Degree of Components Made of Interstitial Free Steel after Uniaxial Tensile Test by the Use of Barkhausen Noise Technique. Steel Research International. 2021, 2100597. DOI: 10.1002/srin.202100597.

[4] Neslušan, M., Bahleda, F., Trojan, K., Pitoňák, M., Zgútová, K., Barkhausen noise emission in over-stressed steel wires. Journal of Magnetism and Magnetic Materials. 2020, Vol. 513, 167134. ISSN 0304-8853, DOI:10.1016/j.jmmm.2020.167134.

[5] Neslušan, M., Trojan, K., Haušild, P., Minárik, P., Mičietová, A., Čapek, J., Monitoring of components made of duplex steel after turning as a function of flank wear by the use of Barkhausen noise emission. Materials Characterization. 2020, Vol. 169, 110587. ISSN 1044-5803, DOI:10.1016/j.matchar.2020.110587.

[6] Neslušan, M., P. Minárik, J. Grenčík, Trojan, K, Zgútová, K. Non-Destructive Evaluation of the Railway Wheel Surface Damage After Long-Term Operation Via Barkhausen Noise Technique. Wear. 2019, Vol. 420–421, pp. 195–206. DOI:10.1016/j.wear.2018.10.016.

[7] Čapek, J., Kolařík, K., Trojan, K., Němeček, J., Ganev, N., Neslušan, M., Pitrmuc, Z., Kyncl, J., Beránek, L., Mikeš, P. Surface integrity after turning a duplex stainless steel with respect to tool geometry. Transactions of Famena. 2018, Vol. 42, 4, pp. 1–14. DOI:10.21278/TOF.42401.

Reviewed publications in the Web of Science or Scopus

[1] Trojan, K., Čapek, J., Ganev, N., Černy, I., Kec, J., Nemeček, S. Residual stresses of laser-hardened railway axles. Experimental Stress Analysis - 58th International Scientific Conference, EAN 2020 - Conference Proceedings. 2020, pp. 547–554.

[2] Čapek, J., Trojan, K., Kec, J., Černy, I., Ganev, N., Kolarik, K., Nemeček, S. Comparison of residual stresses and mechanical properties of unconventionally welded steel plates. Experimental Stress Analysis - 58th International Scientific Conference, EAN 2020 - Conference Proceedings. 2020, pp. 30–36.

[3] Čapek, J., Černý, I., Trojan, K., Ganev, N., Kec, J., Němeček, S. Investigation of residual stresses in high-cycle loaded laser steel welds. Experimental Stress Analysis - 57th International Scientific Conference, EAN 2019 - Conference Proceedings. 2019, pp. 24–29.

[4] Trojan, K., Vlk, A., Capek, J., Hervoches, C., Ganev, N. Residual stresses of laser-welded pressure vessel steel determined by X-ray and neutron diffraction. Experimental Stress Analysis - 57th International Scientific Conference, EAN 2019 - Conference Proceedings. 2019, pp. 535–539.

[5] Čapek, J., Trojan, K., Němeček, J., Ganev, N., Kolařík, K. Comparison of Different Methods Residual Stress Determination of Cold-Rolled Austenitic-Ferritic, Austenitic and Ferritic Steels. Materials Research Proceedings. Millersville: Materials Research Forum LLC. 2018, Vol. 6, pp. 145–150. ISSN 2474-395X, ISBN 978-1-945291-88-3.

[6] Čapek, J., Černík, M., Ganev, N., Trojan, K., Němeček, J., Kolařík, K. Comparison of rolling texture of austenite and ferrite phases of duplex steel with single-phase austenitic and ferritic steel. IOP Conference Series: Materials Science and Engineering. 2018, Vol. 375, 1, pp. 12025–12033. DOI:10.1088/1757-899X/375/1/012025.

[7] Čapek, J., Trojan, K., Němeček, J., Ganev, N., Kolařík, K. Formation of austenite and ferrite preferred orientation during cold-rolling of dual and single-phase steels. Experimental Stress Analysis 2018, Praha. 2018, pp. 41–45. ISBN 978-80-270-4062-9.

[8] Němeček, J., Kolařík, K., Čapek, J., Ganev, N., Trojan, K., Kuzin, V. V. X-ray diffraction study of macroscopic residual stresses of Al2O3 + TiC oxide cutting ceramics after surface machining. Experimental Stress Analysis 2018, Praha. 2018, pp. 296–302. ISBN 978-80-270-4062-9.

[9] Trojan, K., Ocelík, V., Ganev, N., Němeček, S., Čapek, J. Effects of advanced laser processing on the microstructure and residual stresses of H13 tool steel. Experimental Stress Analysis 2017, Košice. 2017, pp. 464–471. ISBN 978-80-553-3167-6.

[10] Čapek, J., Gancarczyk, K., Pitrmuc, Z., Kolařík, K., Málek, J., Beránek, L., Ganev, N., Trojan, K. Grain orientation influence on residual stress distribution of ground surface of blade roots made of inconel 713LC. Experimental Stress Analysis 2017, Košice. 2017, pp. 115–121. ISBN 978-80-553-3167-6.

[11] Kolařík, K., Ganev, N., Trojan, K., Sís, J., Němeček, S. Effect of shielding gas on residual stresses and mechanical properties of laser welding of S355 steel. Experimental Stress Analysis 2016, Srní. 2016. ISBN 978-80-261-0624-1.

[12] Čapek, J., Kolařík, K., Pitrmuc, Z., Ganev, N., Beránek, L., Trojan, K., Kyncl, J., Šimota, J. Influence of Cutting Conditions on Surface Integrity after Progressive Grinding of Blade Roots from Inconel 713LC. Experimental Stress Analysis 2016, Srní. 2016. ISBN 978-80-261-0624-1.

[13] Kolařík, K., Ganev, N., Trojan, K., Řídký, O., Zuzánek, L., Čapek, J. Characterization of residual stresses distribution and real structure in thick welded sheets by X-ray diffraction and barkhausen noise analysis after metal active gas and laser welding. Experimental Stress Analysis 2015, Český Krumlov. 2015, pp. 177–182. ISBN 978-800105734-6.

[14] Kolařík, K., Trojan, K., Čapek, J., Sís, J., Řídký, O., Zuzánek, L., Ganev, N. Residual stress mapping by X-ray diffraction in thick laser welded sheets of DOMEX S355 steel. Experimental Stress Analysis 2014. Plzeň: Výzkumný a zkušební ústav Plzeň s.r.o.. 2014, pp. 65–66. ISBN 978-80-261-0376-9.

Other publications

[1] Trojan, K., Čapek, J., Ocelík, V., Ganev, N. Description of the microstructure of the laser-cladded H13 tool steel using EBSD. Sborník příspěvků 10. studentské vědecké konference fyziky pevných látek. Praha: České vysoké učení technické v Praze. 2021, pp. 55–59. ISBN 978-80-01-06931-8.

[2] Ganev, N., Čapek, J., Trojan, K., Žďárek, J., Kolařík, K. Zbytková Napjatost Povrchových Vrstev Oceli Opracované Metodou Sponge-Jet. Životnost komponent energetických zařízení. Plzeň: Západočeská univerzita v Plzni. 2021, pp. 147–150. ISBN 978-80-261-1045-3.

[3] Trojan, K., Čapek, J., Čech, J., Ocelík, V., Ganev, N. Study of the real structure and hardness of the laser-cladded H13 tool steel. Sborník příspěvků 9. Studentské vědecké konference fyziky pevných látek a materiálů. Praha: České vysoké učení technické v Praze. 2020, pp. 39–42. ISBN 978-80-01-06799-4.

[4] Trojan, K., Čapek, J., Čech, J., Ocelík, V., Ganev, N. Studium reálné struktury laserem navařené nástrojové ocele. Materials Structure. Praha: Krystalografická společnost. 2020, pp. 104–105, Vol. 2. ISSN 1211-5894.

[5] Čapek, J., Ganev, N., Trojan, K., Němeček, S., Kolařík, K. Investigation of the real structure using X-ray diffraction as a tool for laser welding optimization. Advances in X-ray Analysis: Proceedings of the Denver X-ray Conference. Boulevard: The International Centre for Diffraction Data. 2019, Vol. 63. ISSN 1097-0002.

[6] Trojan, K., Ocelík, V., Čapek, J., Ganev, N. Study of the real structure of the laser-cladded steel. Materials Structure. Praha: Krystalografická společnost. 2019, pp. 166–167, Vol. 3. ISSN 1211-5894.

[7] Čapek, J., Trojan, K., Ganev, N. Comparison of the rolling texture of particular phases of dual-phase steel with single-phase steels. Materials Structure. Praha: Krystalografická společnost. 2019, pp. 169–170, Vol. 3. ISSN 1211-5894.

[8] Trojan, K., Ocelík, V., Ganev, N., Němeček, S., Čech, J., Čapek, J., Němeček, J. Effect Of Annealing On The Real Structure And Microstructure Of Advanced Laser Processed AISI H13 Tool Steel. Acta Polytechnica CTU Proceedings.

Praha: Czech Technical University in Prague. 2018, Vol. 17, pp. 15–19. ISSN 2336-5382, ISBN 978-80-01-06459-7.

[9] Neslušan, M., Čilliková, M., Ganev, N., Trojan, K. Influence of tool wear during turning on plasma nitridation and Barkhausen noise emission. Development in Machining Technology/Scientific-Research Reports. Krakow: Cracow University of Technology. 2018, Vol. 8, pp. 76–85. ISBN 978-80-553-2718-1.

[10] Trojan, K., Čapek, J., Čech, J., Ocelík, V., Ganev, N. Evaluation of microstructure in laser-welded ferritic steel plates using electron backscatter diffraction and nanoindentation. Applied Researches in Technics, Technologies and Education. 2018, Vol. 6, 3, pp. 207–212. ISSN 1314-8788.

[11] Trojan, K., Čapek, J., Hervoches, Ch., Ganev, N., Mikula, P., Kolařík, K. Real Structure and Residual Stresses in Advanced Welds Determined by X-ray and Neutron Diffraction Analysis. Materials Structure in Chemistry, Biology, Physics and Technology. 2018, Vol. 25, 2, pp. 79–83. ISSN 1211-5894.

[12] Trojan, K., Ganev, N., Němeček, S., Čapek, J., Němeček, J. Diffraction analysis of surface residual stress distribution on laser welded steel plates. Journal of the Technical University of Gabrovo. Gabrovo: University publishing house. 2018, Vol. 56, pp. 11–14. ISSN 1310-6686.

[13] Čapek, J., Ganev, N., Trojan, K., Kolařík, K. Residual Stresses Determination in Materials with Preferred Orientation. Journal of the Technical University of Gabrovo. Gabrovo: University publishing house. 2018, Vol. 57, pp. 28–30. ISSN 1310-6686.

[14] Neslušan, M., Čilliková, M., Ganev, N., Trojan, K. Influence of tool wear during turning on plasma nitridation and Barkhausen noise emission. Development in Machining Technology/Scientific-Research Reports. Krakow: Cracow University of Technology. 2018, Vol. 8, pp. 76–85. ISBN 978-80-553-2718-1.

[15] Čapek, J., Trojan, K., Němeček, J., Ganev, N. Real structure of ferritic steel and ferrite phase of duplex steel after cold-rolling. Materials Structure in Chemistry, Biology, Physics and Technology. 2018, Vol. 25, 2, pp. 88–91. ISSN 1211-5894.

[16] Trojan, K., Hervoches, Ch., Kolařík, K., Ganev, N., Mikula, P., Čapek, J. Real Structure and Residual Stresses in Advanced Welds Determined by X-ray and Neutron Diffraction. Acta Polytechnica CTU Proceedings. Praha: Czech

Technical University in Prague. 2017, Vol. 9, pp. 32–38. ISSN 2336-5382. ISBN 978-80-01-06298-2.

[17] Kolařík, K., Ganev, N., Trojan, K., Řidký, O., Zuzánek, L., Čapek, J. X-ray Diffraction and Barkhausen Noise Diagnostics of Thick Welds Prepared by Metal Active Gas and Laser Welding. Applied Mechanics and Materials. 2016, Vol. 827, pp. 113–116. ISSN 1660-9336, ISBN 978-3-03835-531-1.

Further, the author contributed to the preparation of 15 scientific publications and 124 research reports. In addition, the author was also the supervisor of a diploma thesis and co-editor of a conference proceeding.